Structure of the small ribosomal subunit from *T. Thermophilus*

Dissertation

zur Erlangung des akademischen Grades
Doctor rerum naturalium (Dr. rer. nat.)

vorgelegt dem
Rat der Biologisch-Pharmazeutischen Fakultät
der Friedrich-Schiller- Universität Jena

von Ante Tocilj, BSc. MSc
geboren am 04. 12. 1971. In Split (Croatia)

Gutachter:

1. ***Prof. Dr. Rolf Hilgenfeld***
2. ***Prof. Dr. Ada Yonath***
3. ***Prof. Dr. Wolfram Saenger***

The work presented in this thesis was performed at the Max-Planck-Arbeitsgruppen für strukturelle Molekularbiologie Hamburg, Germany, under the supervision of Prof. Ada Yonath (MPGARS Hamburg) and Prof. Rolf Hilgenfeld (University of Jena).

My first thanks are due to Prof. Ada Yonath, a supervisor and a group leader one could really wish for and Prof. Rolf Hilgenfeld for his encouragement and for allowing me to fulfill my quest for knowledge.

I am equally indebted to Dr. Frank Schluenzen who guided me through the woes of science and showed me how to sail the waters of crystallography. Also thanks to Dr. Francois Franceschi, Dr. Jorg Harms, Marco Gluehmann and Raz Zarivach for believing in the project from its early stage until the end. My special thanks to Dr. Bill Bennett and Dr. Harly Hansen for critical and constructive discussions.

Thanks also go to all group members in present and past of the Max-Planck-Arbeitsgruppen für strukturelle Molekularbiologie (Hamburg), Max-Planck-Institute for Molecular Genetics (Berlin) and Weizmann Institute of Science (Israel). They made me feel welcome and in many ways helped me to improve myself.

Thanks to my dear friends Marco, Marta, Kristian and Gordana for - being friends!

Abbreviations

50S	The large ribosomal subunit
70S	Prokaryotic ribosome
BS	Back-soaked crystals
CCD	Charged Coupled Device (Detector)
EM	Electron Microscpy
H50S	The large ribosomal subunit from *Haloarcula Marismortui*
IP	Image Plate
MIR	Multiple isomorphous replacement
mRNA	Messenger RNA
SIR	Single isomorphous replacement
SR	Synchrotron radiation
T30S	Small ribosomal subunit from *T. Thermophilus*
TAMM	Tetrakis-acetoxi-mercury-methane
TIR	Tetra Iridium Cluster
tRNA	Transfer RNA
W18	Heteropolytungstate cluster $K_6(P_2W_{18})O_{62}14H_2O$
Wative	W18-treated crystals

Zusammenfassung

Die kleine ribosomale Untereinheit vollzieht die Dekodierung der genetischen Information in der Protein-Biosynthese. Die Struktur dieser Untereinheit von *Thermus thermophilus* zeigt, daß das Dekodierungszentrum, in dem die mRNA und die drei tRNA-Moleküle positioniert werden, ausschließlich aus RNA aufgebaut ist. Der Eingang zum mRNA-Kanal wird durch eine flexible, molekulare Klammer, die wesentlich an dem präzisen Transport der mRNA durch das Ribosom beteiligt ist, umschlossen. RNA-Helizes, die die ribosomale Untereinheit in ihrer ganzen Länge durchziehen, können periphere strukturelle Änderungen innerhalb des Moleküls weiterleiten, und so mit dem Zyklus der mRNA-Translokation synchronisieren.

96% der Nukleotide und die Faltung aller Proteine konnten modelliert werden. Die ribosomalen Proteine sind zum Teil an der Peripherie des Moleküls und tragen als *Linker* zur Organisation der RNA bei. In gewissen Maße könne manche der Proteine zur Translokation beitragen.

Summary

The small ribosomal subunit performs the decoding of genetic information during translation. The structure of that from *Thermus thermophilus* shows that the decoding center, which positions mRNA and three tRNAs, is constructed entirely of RNA. The entrance to the mRNA channel will encircle the message when a latch-like contact closes and contributes to processivity and fidelity. Extended RNA helical elements that run longitudinally through the body transmit structural changes, correlating events at the particle's far end with the cycle of mRNA translocation at the decoding region. 96% of the nucleotides were traced and the main fold of all proteins was determined. The latter are either peripheral or appear to serve as linkers. Some may assist the directionality of translocation.

The structure of the small subunit, presented here at 3.3Å resolution, is essentially a complete molecular description. It includes 1457 nucleotides and the entire fold of all 20 proteins of this particle. It shows known as well as newly detected folding and packing motifs. It provides insight into the decoding mechanism and its universality, and highlights the role of selected components in maintaining the sophisticated architecture of the ribosome.

Introduction

1. Biomacromolecular crystallography

The knowledge of accurate molecular structures is a prerequisite for rational drug design and for structure-based functional studies. Crystallography can reliably provide the answer to many structure-related questions, from global folds to atomic details of bonding. In contrast to NMR, in principle no size limitation exists for the molecules or complexes that are studied.

This introductory chapter gives a brief overview of the methods that have been developed to date to carry out structure solution.

1.1. Crystal structure determination

The determination of macromolecular structures by X-ray crystallographic analysis involves the following steps.

i. Purification and crystallization of biological macromolecules
ii. Diffraction data measurements
iii. Phase determination
iv. Electron density map computation and interpretation
v. Model refinement

1.1.1. Crystallization

Crystallization is one of several means (including nonspecific aggregation/ precipitation) by which a metastable supersaturated solution can reach a stable lower energy state by reduction of solute concentration.[1] The general processes of crystallization are similar for both small molecules (salts and small organics) and biological macromolecules (proteins, DNA, RNA).

There are many methods to crystallize biological macromolecules, all of which aim at bringing their solution to a supersaturated state. Among them, the vapor diffusion technique is probably the most widely used, and it will be shortly described here.

The vapor diffusion method is very well suited for small volumes (down to 2 µl or less). A droplet containing the biological macromolecule to crystallize with buffer, crystallizing agent and additives is equilibrated against a reservoir containing a solution of crystallizing agent at a higher concentration than the droplet. Equilibration proceeds by diffusion of the volatile species (water or organic solvent) until vapor pressure in the droplet equals the one in the reservoir. If equilibration occurs by water exchange (from the drop to the reservoir), it leads to a droplet volume change. For solvents with a vapor pressure higher than water, the exchange occurs from reservoir to drop. This method can be applied to three different systems: hanging drop, sitting drop and sandwiched drop. There are of course variants of vapor diffusion were the statements above do not apply (e.g. salting-in: higher ionic strength in protein droplet than in reservoir).

1.1.2. Phasing

The diffracted X-rays measured from crystals are the Fourier transform of the atomic structure of the material from which the crystal is built. Actually, the diffraction results from the density of electrons in the crystal space. Because the

Fourier transform can be reversed, one can build up a picture of the electron density "map" from the diffracted waves. But this is where the phase problem rears its head; what can be measured is only the intensity of a diffracted wave, and this tells us its amplitude but not the phase angle. It is the phase angle that dominates where the peaks and troughs are placed in electron density reconstruction, and is therefore essential for constructing the correct electron density map. Because phases can not be measured directly, they must be deduced.

There are three commonly used approaches that may be taken for deducing phase information in a diffraction experiment.

The direct methods approach can make estimates about the reflection phases using statistical relations between phases and structure factor amplitudes.[2] Direct methods are routinely used for the solution of small structures and have only recently been applied to the solution of small proteins containing about 50 amino acid residues. However direct methods can only be used if very high-resolution data (<1.2Å) are available which is rarely the case for biological macromolecules.

In case an approximate or a related three-dimensional structure of a similar molecule is known, such information can be used in the course of structure determination. The method called "Molecular Replacement" was pioneered in the sixties by Rossmann and Blow, who explored the possibility of finding the orientation of similar structures in the crystal cell without any knowledge about the rotational and translational components, making use of the Patterson function.[3,4] After the correct orientation is found, a search for the translation vector can be carried out.

The third, commonly used method to solve the phase problem in macromolecular crystallography is isomorphous replacement and related methods. In these methods phase information is obtained by making isomorphous structural modifications to the native protein, usually by including a heavy atom or changing the scattering

strength of a heavy atom already present. If the position of the additional heavy atom or the change in its scattering strength is known then the phase of each diffracted X-ray can be determined by solving a set of simultaneous phase equations. Methods that use such a strategy are Single Isomorphous Replacement (SIR), Multiple Isomorphous Replacement (MIR), Single Isomorphous Replacement with Anomalous Scattering (SIRAS), Multiple Isomorphous Replacement with Anomalous Scattering (MIRAS) and, within the last 15 years, the Multiple wavelength Anomalous Diffraction method (MAD) where a strong anomalous effect is required together with the possibility to tune the wavelength.[5,6]

1.1.3. Density modification

With an experimental set of phases, one can calculate a three-dimensional electron density map of the crystal structure. The phase information obtained from experimental measurements on macromolecules using either multiple isomorphous replacement or multi-wavelength anomalous diffraction is often insufficient for constructing a electron-density map useful for model building. Many density-modification methods have been developed in recent years for improving the quality of electron-density maps by incorporation prior knowledge about the features expected in these maps when they are obtained at high or moderate resolution (2-4Å). Among the most powerful of these methods are solvent flattening, non-crystallographic symmetry averaging, histogram matching, phase extension, entropy maximization and iterative model building, however still the main density modification technique involves the alternate application of two processes.[7,8]

Map modification: Electron density is modified in accordance with the chemical knowledge about the nature of protein structure. This gives rise to a modified map.
Phase combination: Modified phases are weighted on the basis of how well the modified magnitudes match their observed values, and then a weighted combination with the experimental phases is performed.

1.1.4. Model building and refinement

An initial model built into an experimental map, or in a poorly phased molecular replacement map, will usually contain many errors. In order to produce an accurate model, it is necessary to carry out crystallographic refinement as well as interactive rebuilding. Depending on the size of the structure, the automatic (refinement) or the manual (rebuilding) parts may be rate-limiting. Refinement programs change the model in order to improve the fit between the observed and the calculated structure-factor amplitudes. Due to the limited resolution typically obtained in biomacromolecular crystallography, the relatively scarce experimental data is augmented by chemical information, for instance concerning bond lengths and angles. Interactive model rebuilding is necessary for the removal of errors that cannot be remedied by refinement programs. In rebuilding, the experimental map (if available) should always be kept, and at each stage one should try to re-interpret it according to the current model, assisted by the current $2F_o$-F_c, F_o-F_c and other maps. While rebuilding a model, the accumulated knowledge concerning macromolecular structures should be used in order to locate deviations from our expectations and from previous experience (as pertaining to quality of the fit between the model and the map, stereochemistry, preferred conformations and environments of residues); such deviations could indicate local errors.

After the phase of model building, refinement of the model is carried out against the experimentally measured intensities. This stage may include the addition of ordered solvent molecules and in cases where very high resolution X-ray data are available even the addition of hydrogen atoms, although the latter is rare for macromolecular structures. The refinement program will use any degree of freedom it is given to reduce the discrepancy between observed and calculated structure factors. However, since the data are afflicted by error, and since the model is not an exhaustive description of all scattering matter in the crystal (space- and time-

averaged), this may easily lead to a situation in which the errors are compensated by erroneous changes to the model. Recently, Brünger introduced a cross-validation scheme based on the so-called free R-factor, or R_{free}.[9] The idea is to set aside a small fraction of the data (the "test set") which is not used in the refinement, but for which an R-factor is nevertheless calculated. The comparison of the values of the conventional and the free R-factor indicates the extent to which one has over-fitted the map as well as the quality of the model and the data.

1.2. Phasing strategy for ribosomal particles

The assignment of phases to the observed structure factor amplitudes is the most crucial and most complicated step in structure determination. Since the phases cannot be directly measured, their elucidation remains the least predictable task, even for average-size proteins. Multiple and single isomorphous replacement (MIR and SIR) and multiple anomalous dispersion (MAD), are the commonly used methods for phasing diffraction data from crystals of biological macromolecules. All require the preparation of heavy atom derivatives in which electron-dense atoms are inserted into the crystalline lattice at distinct locations. As the changes in the structure factor amplitudes resulting from the addition of the heavy atoms are being exploited, the derivatization reagents are chosen according to their potential ability to induce measurable signals.

Originally it was not clear that phase information could be obtained at high resolution for large asymmetric particles like ribosomes, but the development of bright, tunable synchrotron radiation sources, large and accurate area detectors, vastly improved crystallographic computing, and the advent of cryocrystallography have all contributed to making structural studies of the ribosome more tractable. The use of anomalous scattering from the L_{III} edges of lanthanides, osmium, iridium and tungsten derivatives has also played a critical role in obtaining phases.[10-14]

The strategy proved, so far, to be most suitable for phasing ribosomal data is based on the determination of an initial phase set at low resolution. This may be extended later, by experimental or computational methods. Molecular replacement exploiting cryoelectron-microscopy reconstructions proved useful for H50S, T50S and for the whole ribosome from *T. thermophilus,* T70S.[10,15,16] For T30S, however, despite extensive attempts, no solution was obtained, perhaps because of its multi-conformational nature and inherent flexibility.[16,17] Therefore phasing was performed by MIR-type methods. Advantage was taken of dense compounds containing a large number of heavy-atoms, arranged in close proximity.[18] These were used either for pre-crystallization covalent binding at preferred locations, or for traditional soaking experiments.[19] Despite the large size of the clusters that may have hampered their penetration into the crystals, many of the soaking experiments were successful, presumably because the ribosomal crystals contain wide internal solvent channels. Furthermore, it seems that for crystals with large solvent regions, the large size of these compounds is advantageous, as it limits the free movement of the crystallized particles and minimizes multiple site binding.

Heteropolytungstates yielded useful derivatives in crystallographic studies of several biological macromolecules, all by soaking experiments. These large anions are of exceptional stability over a wide range of pH and redox states. They posses a high degree of internal symmetry, and a correlation between it and their binding sites has been detected. In such cases they were found suitable for high resolution phasing. An example is the structure of riboflavin synthase that possess an internal five fold symmetry, which coincided with that of ($NaP_5W_{30}O_{110}$).[20] However, in the absence of preferred orientation, the effective phasing resolution is limited to 4-5 Å, even when sophisticated spherical averaging techniques are being used.[21] Nevertheless under favorable conditions, it was found that W18 clusters did bind in a specific way, so that its individual W atoms could be resolved at resolution higher than 4.0 Å, and used for phasing.

In ribosomal crystallography the heteropolytungstates were found to be very suitable for phasing at low resolution, as well as for the validation of the results obtained by molecular replacement searches.[10] So far, reports of materials that generated phases include: W12 ($Na_{16}[(O_3PCH_2PO_3)_4W_{12}O_{36}]40H_2O$) and W17 ($Cs_7(P_2W_{17}O_{61}Co(NC_5H_5))14H_2O$), as well as W9 $[(phSn)_4(AsW_9O_{33})_2]$ and W11Rh $Cs_5(PW_{11}O_{39}[Rh_2CH_3COO_2]$ were used in phasing the data of the halophilic large subunit.[10,22] $H_4SiO_4[12WO]$ and $Li_{10}(P_2W_{17}O_{61})$ as well as W18 ($(NH_4)_6(P_2W_{18}O_{62})14H_2O$), and W4 ($Na_2[Nb_2W_4O_{19}]18H_2O$) were used for the determination of the high and medium resolution structure of the thermophilic small ribosomal subunit.[11-13]

Additional examples are smaller compounds, Ta_6Br_{14}, a tetra mercury compound, TAMM, and a tetra iridium cluster, TIR.[23] Among them, Ta_6Br_{14} yielded phase information for all ribosomal particles currently being studied, namely, T30S, T50S, T70S and H50S.[10-14,18,24] The other two compounds, TIR and TAMM were designed to bind covalently to exposed sulfhydryls and led to the localization of two ribosomal proteins of the small subunit, S11 and S13.[19]

2. RNA binding proteins

How proteins selectively bind specific sites on nucleic acids has been a challenging and interesting problem since the earliest days of molecular biology. This impressive feat of molecular recognition has been intensively studied ever since, and there are now a large number of atomic resolution structures of protein-DNA complexes which, with parallel thermodynamic studies, provide a picture of how sequence-specifc DNA recognition is performed by a variety of repressors, transcription factors, and restriction enzymes. For a variety of reasons, biochemical and physical characterization of protein-RNA complexes has lagged behind corresponding studies of protein DNA complexes by more than a decade.

2.1. RNA recognition themes

RNA-binding proteins play a key role in a wide range of cellular processes, so there is considerable interest in understanding how these proteins recognize RNA.

Three basic strategies for recognizing specific RNA sites can be discerned. First, when an α-helix provides a surface suitable for hydrogen bonding to RNA bases, presumably in the distorted (minior or major) groove of helix. Second, aromatic residues on the twisted surface of a β-sheet are a means to bind unstacked bases; additional polar groups can then hydrogen bond to the bases to provide sequence specificity. Third, extended loops, frequently poorly structured in the absence of nucleic acid, provide additional free energy of binding by interactions with sugar-phosphate backbone moieties. These backbone interactions may contribute specificity, to the degree that they depend on a particular conformation of the backbone.

2.2. RNA binding motifs

Many RNA-binding proteins are modular and contain distinct globular domains that mediate RNA binding.[25,26] These are found in a variety of proteins across a wide range of organisms. Four RNA-binding domains (RBD) that have already been structurally characterized are referred to as RNP, KH, dsRBD (double-stranded RNA-binding domain) and S1.

The RNP domain is present in many proteins that participate in mRNA splicing, as well as in numerous other RNA-binding proteins.[27] It binds to a range of different RNA molecules with a varying degree of specificity. The KH module is found in many hnRNP proteins and in a number of other RNA-associated proteins.[28,29] Many proteins that interact with double-stranded RNA contain the dsRBD domain, which does not bind to ssRNA and can discriminate between dsRNA and dsDNA.[30-32] A fourth RNA-binding motif was first identified in the *E. coli* ribosomal protein S1.[33]

Since RNA adopts a much greater variety of non-canonical and tertiary structures than does DNA, one might have expected that the bestiary of RNA-binding proteins would be more exotic than the corresponding collection of DNA-binding proteins. But so far it appears that most of the protein frameworks for RNA recognition are not much different from duplex and single-strand-specific DNA binding proteins. Similarities between DNA and RNA binding strategies imply that the two sets of proteins may not have evolved independently. Thus the ribosome, which must include some of the first nucleic acid binding proteins to evolve, may have served as a reservoir of nucleic acid binding motifs during evolution.

3. Small ribosomal subunit

Ribosomes are complex and dynamic ribonucleoprotein assemblies that provide the framework for protein biosynthesis in all organisms. Ribosomes are composed of two unequal subunits. In prokaryotes these are called the 30S subunit, composed of 16S rRNA (1542 nucleotides) and 21 different proteins (S1–S21), and the 50S subunit, composed of two rRNA molecules, 5S (120 nucleotides) and 23S (2904 nucleotides), and 34 different proteins (L1–L34). Understanding the detailed structure of the ribosome and its individual subunits is the key to understanding the mechanism of translation.

The small ribosomal subunit (30S in prokaryotes) is responsible for decoding the genetic information. It discriminates among aminoacyl tRNA molecules, ensures translational fidelity and forms the initiation complex. This requires the interaction of the ribosomal subunit with a several protein factors such as initiation, elongation and termination factors, but also makes it a natural target of ligands that inhibit protein biosynthesis, like toxins and antibiotics.[34]

Many techniques have been used to determine the spatial arrangement of the ribosomal components. Early work using immune electron microscopy, protein–protein crosslinking and neutron scattering focused on the proteins.[35-38] However, with the development of suitable technology and the appreciation of the importance of the RNA component of the ribosome, a lot of work was directed towards understanding the RNA structure. For this the techniques that were used are RNA–RNA crosslinking, mutagenesis and analyses of RNA sequences for long-distance base-pair interactions.[39] Such an extensive pool of biochemical data provided both constraints and modules which were used to build a tentative models of ribosomal particles.[40-42] Clearly, the spatial arrangements of the protein and RNA components in such models had to be consistent with data obtained by protein–RNA crosslinking and footprinting experiments.[43,44]

Crystallographic reports describe low and medium-resolution partial structures for the intact ribosome (70S) from *T. thermophilus*, at 7.8 Å, the large subunit from *Haloarcula marismortui*, at 5Å, the small (30S) subunit from *T. thermophilus*, at 5.5Å, and the activated form of this subunit, at 4.5Å.[10-12,15] Advances in electron cryomicroscopy (cryo-EM) have also revealed new features of ribosomal particles and their complexes.[17,45,46] In parallel, the structures of several ribosomal protein–RNA complexes have been determined at high resolution.[47-50]

The Year 2000 is "The Year of Ribosome" since the essentially complete high-resolution structures of the large and small ribosomal subunit were determined.[12,13,24,51] The structure of the latter was later confirmed by independent group.[14,52]

Methods

4. Crystallization

The crystallization of the T30S subunit was performed using the hanging-drop vapor-diffusion method with 10µl drops equilibrated against 1 ml of reservoir solution at 20 °C as described.[22,53] The 30S concentration was around 21 nmol/ml. The 30S subunits were incubated with spermidine hydrocloride to a final concentration of 10 mM, then "heat-activated" for 5 min at 65°C.[12] Methyl-pentane-diol (MPD) was used as precipitating agent. The final concentration of MPD in the drop was between 0 and 1.5%, while the MPD concentration in the reservoir varied between 14 and 18%.

The crystals of the small ribosomal subunit (Figure 1) belong to space group $P4_12_12$ with unit cell axis **a**,**b**=407Å, **c**=176Å and were treated by the addition of mM amounts of W18. Back-soaked (BS) crystals were generated by soaking the W18-treated crystals (Wative) in their stabilization solution for 10-40 hours. Derivatization was performed by soaking the Wative crystals in heavy atom solutions, in the presence or in the absence of W18, as dictated by the stability of the crystals.

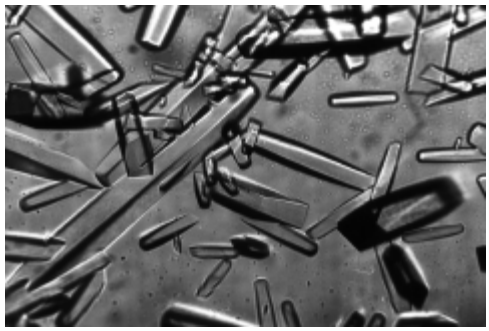

Figure 1 Crystals of the small subunit from Thermus thermophilus

5. X-ray data collection

Single crystal X-ray and neutron crystallography are the only methods that offer direct structural information and have proven to be the most powerful techniques for obtaining a reliable molecular model. Synchrotron radiation, which produces an intense, coherent and focused beam, generated in accelerators often designed for high-energy particle experiments, is being widely used in crystallographic studies of biological macromolecules. It turned out to be the only suitable X-ray source for crystallographic studies of ribosomal crystals, because its high brightness and focusing are indispensable in order to record their diffraction pattern.

Crystallographic data were collected at cryo-temperature (about -180^{o}C) using the screenless rotation method. In this method, the crystal is rotated around an axis perpendicular to the incoming X-ray beam, and for each small rotation angle, the diffraction pattern is recorded. In this way the diffractions of a section of the 3D reciprocal lattice are recorded simultaneously on the detector (film, ImagePlates, CCD). However, due to limitations of synchrotron beam time and the decay of the diffraction at higher beam intensities, we have to economize in the rotation limits. Thus during data collection from T30S crystals, we were trying to align the crystals so that their highest symmetry axis coincides with the spindle axis, to take advantage of the crystal symmetry, which enables smaller total ranges of rotation

Data were collected with a bright synchrotron beam at cryo temperature (86-90 K) from flash frozen crystals as described.[12] For anomalous data collection the wavelength was adjusted to the L_3 edge of W. In order to make an accurate measurements of anomalous pairs, care was taken to align the crystal along the **c** unit cell axis. Prior to data collection, a fluorescence scan (Figure 2), revealed a broad W L_3 with a maximum f'' at 1.2Å.

The data were recorded either on the 345 mm MAR or CCD detectors (QUANTUM4 or APS2) and processed by HKL2000.[54] Collecting the 3-4Å shell, decay was detected

within a period sufficient for 1-1.5° oscillations. To facilitate the collection of complete data set from single crystal, a beam with a smaller cross-section was used. Translating the rod-like crystals (about 500x60x60 microns) once decay was observed allowed measurements from 2-6 separate regions.

A typical rotation photograph of the X-ray diffraction pattern from a crystal of T30S (W18 soak) is shown in Figure 3. Data were collected at the ESRF on beamline ID2. The lune shaped areas can be clearly seen. Each lune is the projection of the area between two small circles produced by the intersection of the Ewald sphere with a particular reciprocal lattice level, throughout the oscillation. The rotation of the crystal during data collection enables the recording of a volume element of the reciprocal space, on each frame (photographs or IP's or CCD).

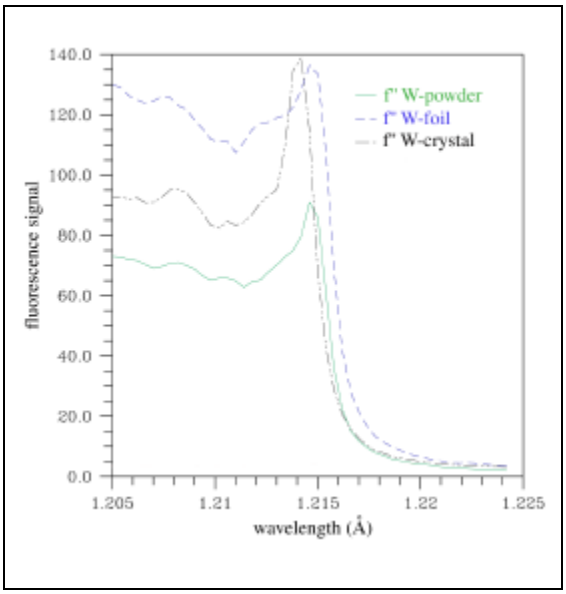

Figure 2 f'' as a function of wavelength, as derived from fluorescence spectra measured from a W foil, W powder and a crystal soaked in a W18 solution, all measured around the W L3 edge

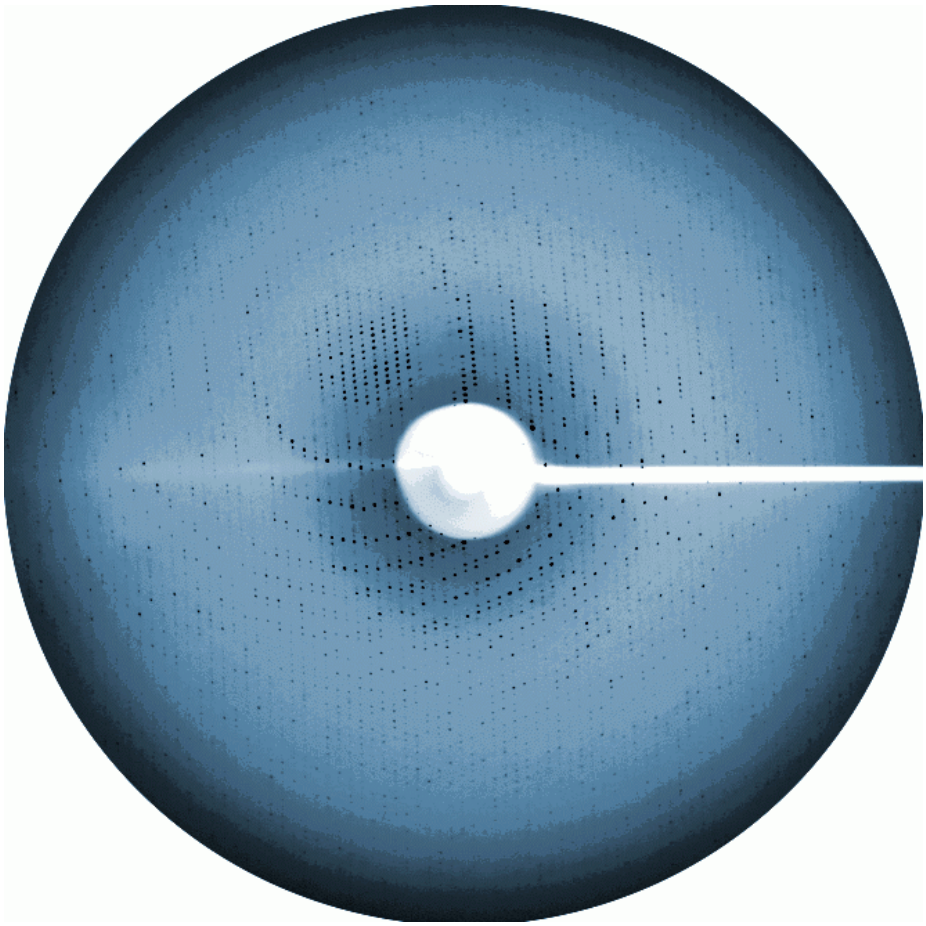

Figure 3 One degree rotation photograph of the X-ray diffraction pattern from a T30S crystal soaked in solution of 0.05mM W18 obtained at ID2/ESRF.

6. Phasing

6.1. MIRAS Phasing

A Harker section of the difference Patterson map Patterson (Figure 4) of data from a W18 cluster showed a clear strong peak of about 7 standard deviations above background, as well as a second minor peak. The positions of these sites and phases to low resolution were calculated using the program SHARP.[55] Difference Fourier synthesis using these low-resolution phases revealed a substantial number of sites in the other heavy-atom derivatives. The program SHARP was used to determine independently and to confirm these sites, as well as to calculate phases by Bayesian phase refinement.[55] The single native data set was not used in the phasing because of lack of isomorphism; therefore the Wative high-resolution data set was used as the 'native' or reference data set in the MIRAS phasing. Phase refinement was performed by sequential addition of the derivatives after pre-refinement as summarized in Table 1. Individual W atoms of the well-ordered W18 cluster were used for phasing beyond 4.0Å; otherwise, the tungsten clusters were represented by their spherically averaged form-factor.

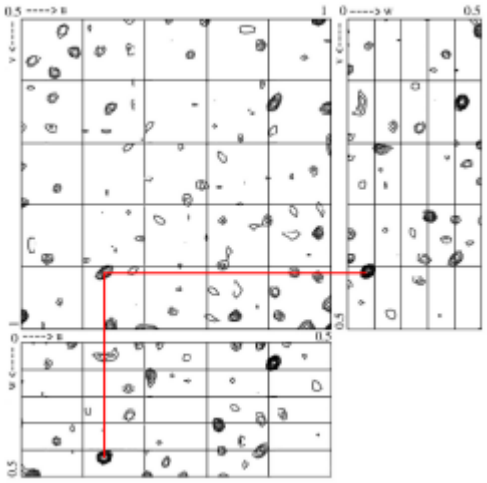

Figure 4 Three Harker sections of the difference Patterson map contoured at 4s, using data collected from Wative and back soaked (BS) crystals, constructed at 8Å resolution showing the main W18 site (red line).

Table 1 MIRAS phasing statistics

	Wative 1	Wative 2	Backsoak	Ir	IrG	Os	Ta_6Br_{12}
Data Collection							
Reflections	2186910	327448	725465	154875	218049	82258	99137
Unique reflections	206724	133199	122788	45748	71096	25593	48132
Completeness	94.7 (77.1)	80.5 (73.1)	86.4 (82.8)	91.3(95.2)	69.3 (68.2)	70.4 (42.8)	56.1 (38.5)
Mean [I/sigma(I)]	21.9 (3.6)	12.3 (2.8)	14.5 (3.3)	11.5 (6.7)	10.7 (3.9)	12.8 (4.9)	10.5 (3.1)
R_{sym}	13.6 (44.1)	10.6 (29.4)	12.7 (34.7)	11.3 (34.2)	12.4 (24.8)	10.3 (46.3)	14.3 (33.2)
d_{min} (Å)	3.3	3.5	3.8	5.4	4.5	5.8	5.0
Phasing							
Sites	13*	10*	8*	14	4	15	5
R_{cullis} (centric)	-	0.67	0.60	0.64		0.87	0.82
R_{cullis} (acentric)°	- / 0.80	0.76 / 0.66	0.72 / 0.56	0.80 /0.83	0.75 / 0.66	0.87 / 0.63	0.88 / -
PP (centric)	-	0.64	1.14	0.98	0.79	1.06	0.98
PP (acentric)°	- / 0.65	0.70 / 0.94	1.22 / 0.75	1.21 /0.85	0.96 / 1.13	1.32 / 0.73	1.13 / -

PP: Phasing Power = <|Fh(calc)|>/<phase-integrated lack of closure. R_{cullis} = <phase-integrated lack of closure>/<|Fph-Fp|>.

Rcullis and Phasing power were obtained from SHARP. The compounds used for derivatization have been described[12] except for Ir = sodium-Ir chloride. Additional minor heavy atoms used for phasing have been omitted from this table. The overall figure of merit (FOM) was 0.48 after MIRAS phasing with SHARP, and 0.78 after density modification with SOLOMON.

° isomorphous/anomalous. Highest resolution bins are given in brackets. *Number of W_{18} sites. Among them four were represented by individual atoms, the remaining sites by their spherically averaged form factor.

6.2. Density Modification

Density modification using the program SOLOMON was used to improve initial phases obtained from SHARP.[7,55] In order to remove any potential bias of W18, density modification procedure were altered to include gradually the low-resolution terms.

7. Model building and refinement

The model was built using the sequence of the 16S RNA and the proteins from *T. thermophilus* (except for protein S16, for which we exploited the sequence of *Bacillus subtilis* since that of *T. thermophilus* was not available). The program O was used for map interpretation.[56] Initially the map was interpreted at 3.8Å. At that stage the map was sufficiently clear so that the backbone phosphates could be positioned unambiguously for most of the RNA chain. Density for the bases was present, but individual bases were hardly separated. The RNA chain was traced by following features in the map, while maintaining acceptable bond lengths and angles. Subsequently the primary structure and the secondary-structure diagrams of the 16S RNA were consulted to confirm interpretation.[57] In most cases, no significant discrepancies were detected. The few disagreements are associated mainly with multiple junctions. One example is the three-way junction of H28/H29/H43, which does not show the triplet formation but instead contains an E loop motif, as suggested.[58] Where coordinates for individual proteins were available, they were introduced as rigid bodies, and rebuilt as needed. The structures of the RNA-protein complexes that became available were consulted after the 3.8Å map was traced. The spatial arrangement of the rRNA chains was found to be in reasonable agreement with most of the independently derived biochemical and biophysical data.

The current 3.3Å map shows a large number of well-resolved individual bases and protein side chains (Figure 5). The folds of the proteins that had not been determined by NMR or X-ray crystallography could be assigned directly from the map.

Initial refinement of the monoclinic form was carried out by CNS and REFMAC.[59,60] After manual adjustment of the model as indicated by σ_A-weighted $2F_o–F_c$ and $F_o–F_c$ difference maps, refinement was continued using the high-resolution data set to 3.3Å. For this, iterative cycles of refinement and model building with O were extended step-wise to 3.3Å resolution. The correctness of the fit was assessed by using OMIT procedures, inspecting a $2F_o$-F_c σ_A weighted map.[61]

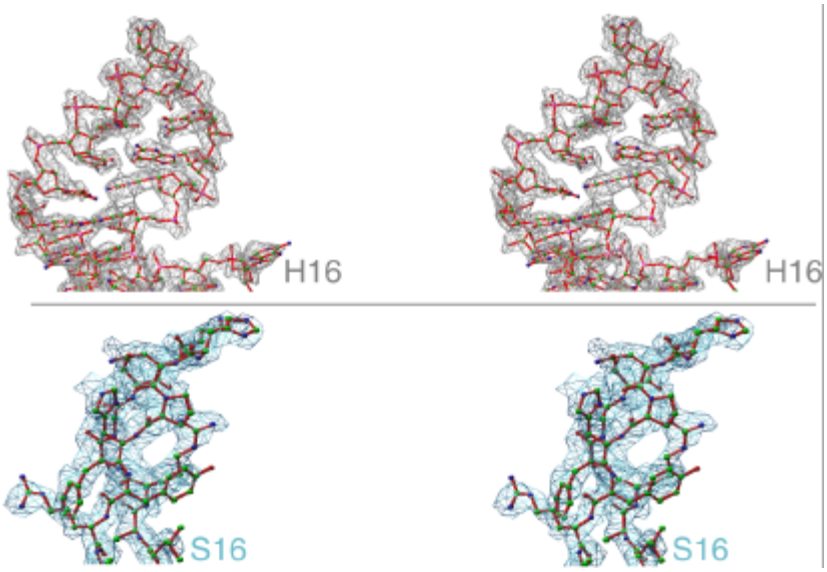

Figure 5 A stereo view of a $2F_o$-F_c s_A weigthed OMIT map at 3.3 Å resolution, with the model superimposed.

8. Bibliography

1. Weber, P. C. Physical principles of protein crystallization. *Adv. Prot. Chem.* **41**, 1-36 (1991).
2. Karle, J. & Hauptmann, H. A. The phases and magnitudes of the structure factors. *Acta Cryst.* **3**, 181-187 (1950).
3. Rossman, M. G. *The molecular replacement method.* (ed. Rossman, M. G.) (Gordon and Brreach science publishers, New-York, 1971).
4. Patterson, A. L. *Phys. Rev.* **46**, 372 (1934).
5. Hendrickson, W. A. Determination of macromolecular structures from anomalous diffraction of synchrotron radiation. *Science* **254**, 51-8 (1991).
6. Guss, J. M. et al. Phase determination by multiple-wavelength x-ray diffraction: crystal structure of a basic "blue" copper protein from cucumbers. *Science* **241**, 806-11 (1988).
7. Abrahams, J. P. & Leslie, A. G. W. Methods used in the structure determination of bovine mitochondrial F-1 ATPase. *Acta Crystallographica Section D-Biological Crystallography* **52**, 30-42 (1996).
8. Terwilliger, T. C. Maximum-likelihood density modification. *Acta Crystallogr D Biol Crystallogr* **56**, 965-72 (2000).
9. Brunger, A. T., Kuriyan, J. & Karplus, M. Crystallographic R factor refinement by molecular dynamics. *Science* **235**, 458-460 (1987).
10. Ban, N. et al. Placement of protein and RNA structures into a 5 Å -resolution map of the 50S ribosomal subunit. *Nature* **400**, 841-847 (1999).
11. Clemons, W. M., Jr. et al. Structure of a bacterial 30S ribosomal subunit at 5.5 A resolution. *Nature* **400**, 833-840 (1999).
12. Tocilj, A. et al. The small ribosomal subunit from Thermus thermophilus at 4.5 A resolution: pattern fittings and the identification of a functional site. *Proc Natl Acad Sci U S A* **96**, 14252-14257 (1999).

13. Schluenzen, F. et al. Structure of functionally activated small ribosomal subunit at 3.3 angstroms resolution. *Cell* **102**, 615-23 (2000).
14. Wimberly, B. T. et al. Structure of the 30S ribosomal subunit. *Nature* **407**, 327-39 (2000).
15. Cate, J. H., Yusupov, M. M., Yusupova, G. Z., Earnest, T. N. & Noller, H. F. X-ray crystal structures of 70S ribosome functional complexes. *Science* **285**, 2095-2104 (1999).
16. Harms, J. et al. Elucidating the medium-resolution structure of ribosomal particles: an interplay between electron cryo-microscopy and X-ray crystallograhy. *Structure Fold Des* **7**, 931-941 (1999).
17. Gabashvili, I. S., Agrawal, R. K., Grassucci, R. & Frank, J. Structure and structural variations of the Escherichia coli 30 S ribosomal subunit as revealed by three-dimensional cryo-electron microscopy. *Journal of Molecular Biology* **286**, 1285-1291 (1999).
18. Thygesen, J., Weinstein, S., Franceschi, F. & Yonath, A. The suitability of multi-metal clusters for phasing in crystallography of large macromolecular assemblies. *Structure* **4**, 513-8 (1996).
19. Weinstein, S. et al. Metal compounds as tools for the construction and the interpretation of medium-resolution maps of ribosomal particles. *Journal of Structural Biology* **127**, 141-151 (1999).
20. Ladenstein, R., Bacher, A. & Huber, R. Some observations of a correlation between the symmetry of large heavy- atom complexes and their binding sites on proteins. *J Mol Biol* **195**, 751-3 (1987).
21. Fu, J. et al. Yeast RNA polymerase II at 5 A resolution. *Cell* **98**, 799-810 (1999).
22. Yonath, A. et al. Characterization of crystals of small ribosomal subunits. *J Mol Biol* **203**, 831-4 (1988).
23. Jahn, W. Synthesis of water soluble tetrairidium cluster for specific labelling of proteins. *Z. Naturforsch* **44b**, 79-82 (1989).
24. Ban, N., Nissen, P., Hansen, J., Moore, P. B. & Steitz, T. A. The complete atomic structure of the large ribosomal subunit at 2.4 A resolution [see comments]. *Science* **289**, 905-20 (2000).

25. Mattaj, I. W. RNA recognition: a family matter? *Cell* **73**, 837-40 (1993).
26. Burd, C. G. & Dreyfuss, G. Conserved structures and diversity of functions of RNA-binding proteins. *Science* **265**, 615-21 (1994).
27. Nagai, K., Oubridge, C., Ito, N., Avis, J. & Evans, P. The RNP domain: a sequence-specific RNA-binding domain involved in processing and transport of RNA. *Trends Biochem Sci* **20**, 235-40 (1995).
28. Siomi, H., Matunis, M. J., Michael, W. M. & Dreyfuss, G. The pre-mRNA binding K protein contains a novel evolutionarily conserved motif. *Nucleic Acids Res* **21**, 1193-8 (1993).
29. Musco, G. et al. Three-dimensional structure and stability of the KH domain: molecular insights into the fragile X syndrome. *Cell* **85**, 237-45 (1996).
30. St Johnston, D., Brown, N. H., Gall, J. G. & Jantsch, M. A conserved double-stranded RNA-binding domain. *Proc Natl Acad Sci U S A* **89**, 10979-83 (1992).
31. Bycroft, M., Grunert, S., Murzin, A. G., Proctor, M. & St Johnston, D. NMR solution structure of a dsRNA binding domain from Drosophila staufen protein reveals homology to the N-terminal domain of ribosomal protein S5 [published erratum appears in EMBO J 1995 Sep 1;14(17):4385]. *Embo J* **14**, 3563-71 (1995).
32. Kharrat, A., Macias, M. J., Gibson, T. J., Nilges, M. & Pastore, A. Structure of the dsRNA binding domain of E. coli RNase III. *Embo J* **14**, 3572-84 (1995).
33. Subramanian, A. R. Structure and functions of ribosomal protein S1. *Prog Nucleic Acid Res Mol Biol* **28**, 101-42 (1983).
34. Janosi, L. et al. Evidence for in vivo ribosome recycling, the fourth step in protein biosynthesis. *Embo J* **17**, 1141-51 (1998).
35. Stoffler, G. & Stoffler-Meilicke, M. Immunoelectron microscopy of ribosomes. *Annu Rev Biophys Bioeng* **13**, 303-30 (1984).
36. Lambert, J. M., Boileau, G., Cover, J. A. & Traut, R. R. Cross-links between ribosomal proteins of 30S subunits in 70S tight couples and in 30S subunits. *Biochemistry* **22**, 3913-20 (1983).
37. Walleczek, J., Redl, B., Stoffler-Meilicke, M. & Stoffler, G. Protein-protein cross-linking of the 50 S ribosomal subunit of Escherichia coli using 2-iminothiolane.

Identification of cross-links by immunoblotting techniques. *J Biol Chem* **264**, 4231-7 (1989).

38. Capel, M. S. et al. A complete mapping of the proteins in the small ribosomal subunit of Escherichia coli. *Science* **238**, 1403-6 (1987).
39. Brimacombe, R. The structure of ribosomal RNA: a three-dimensional jigsaw puzzle. *Eur J Biochem* **230**, 365-83 (1995).
40. Mueller, F. & Brimacombe, R. A new model for the three-dimensional folding of *Escherichia coli* 16S ribosomal RNA. I. Fitting the RNA to a 3D electron microscopic map at 20 Å. *J. Mol. Biol.* **271**, 524-544 (1997).
41. Mueller, F. & Brimacombe, R. A new model for the three-dimensional folding of Escherichia coli 16 S ribosomal RNA. II. The RNA-protein interaction data. *J Mol Biol* **271**, 545-65 (1997).
42. Mueller, F., Stark, H., vanHeel, M., RinkeAppel, J. & Brimacombe, R. A new model for the three-dimensional folding of Escherichia coli 16 S ribosomal RNA. III. The topography of the functional centre. *J. Mol. Biol.* **271**, 566-587 (1997).
43. Osswald, M. et al. RNA-protein cross-linking in Escherichia coli 30S ribosomal subunits; determination of sites on 16S RNA that are cross-linked to proteins S3, S4, S5, S7, S8, S9, S11, S13, S19 and S21 by treatment with methyl p-azidophenyl acetimidate. *Nucleic Acids Res* **15**, 3221-40 (1987).
44. Powers, T. & Noller, H. F. Hydroxyl radical footprinting of ribosomal proteins on 16S rRNA. *Rna* **1**, 194-209 (1995).
45. Gabashvili, I. S. et al. Solution structure of the E. coli 70S ribosome at 11.5 A resolution. *Cell* **100**, 537-549 (2000).
46. Stark, H., Rodnina, M. V., Wieden, H. J., van Heel, M. & Wintermeyer, W. Large-scale movement of elongation factor G and extensive conformational change of the ribosome during translocation. *Cell* **100**, 301-309 (2000).
47. Conn, G. L., Draper, D. E., Lattman, E. E. & Gittis, A. G. Crystal structure of a conserved ribosomal protein-RNA complex. *Science* **284**, 1171-1174 (1999).
48. Wimberly, B. T., Guymon, R., McCutcheon, J. P., White, S. W. & Ramakrishnan, V. A detailed view of a ribosomal active site: the structure of the L11- RNA complex. *Cell* **97**, 491-502 (1999).

49. Agalarov, S. C., Sridhar Prasad, G., Funke, P. M., Stout, C. D. & Williamson, J. R. Structure of the S15,S6,S18-rRNA complex: assembly of the 30S ribosome central domain. *Science* **288**, 107-113 (2000).
50. Nikulin, A. et al. Crystal structure of the S15-rRNA complex. *Nature Structural Biology* **7**, 273-277 (2000).
51. Nissen, P., Hansen, J., Ban, N., Moore, P. B. & Steitz, T. A. The structural basis of ribosome activity in peptide bond synthesis [see comments]. *Science* **289**, 920-30 (2000).
52. Carter, A. P. et al. Functional insights from the structure of the 30S ribosomal subunit and its interactions with antibiotics [see comments]. *Nature* **407**, 340-8 (2000).
53. Trakhanov, S. D. et al. Crystallization of 70-S Ribosomes and 30-S Ribosomal-Subunits from *Thermus Thermophilus*. *Febs Letters* **220**, 319-322 (1987).
54. Otwinowski, Z. & Minor, W. Processing of X-ray diffraction data collected in oscillation mode. *Macromolecular Crystallography, Pt A* **276**, 307-326 (1997).
55. de la Fortelle, E. & Bricogne, G. Maximum-likelihood heavy-atom parameter refinement for multiple isomorphous replacement and multiwavelength anomalous diffraction methods. *Macromolecular Crystallography, Pt A* **276**, 472-494 (1997).
56. Jones, T. A. & Kjeldgaard, M. Electron-density map interpretation. *Meth. Enzimol.* **277**, 173-208 (1997).
57. Gutell, R. R. Collection of small subunit (16S- and 16S-like) ribosomal RNA structures: 1994. *Nucleic Acids Res* **22**, 3502-3507 (1994).
58. Leontis, N. B. & Westhof, E. A common motif organizes the structure of multi-helix loops in 16 S and 23 S ribosomal RNAs. *J Mol Biol* **283**, 571-583 (1998).
59. Brunger, A. T. et al. Crystallography and nmr system (CNS): A new software system for macromolecular structure determination. *Acta Crystallogr D Biol Crystallogr* **54**, 905-921 (1998).
60. Murshudov, G. N., Vagin, A. A., Lebedev, A., Wilson, K. S. & Dodson, E. J. Efficient anisotropic refinement of macromolecular structures using FFT. *Acta Crystallogr D Biol Crystallogr* **55**, 247-55. (1999).

61. Bailey, S. The Ccp4 Suite - Programs for Protein Crystallography. *Acta Crystallogr D Biol Crystallogr* **50**, 760-763 (1994).

The small ribosomal subunit from *Thermus thermophilus* at 4.5 Å resolution: Pattern fittings and the identification of a functional site

Ante Tocilj*, Frank Schlünzen*, Daniela Janell*, Marco Glühmann*, Harly A. S. Hansen*, Jörg Harms*, Anat Bashan†, Heike Bartels*†, Ilana Agmon†, Francois Franceschi‡, and Ada Yonath*†§

*Max Planck Research Unit for Ribosomal Structure, 22603 Hamburg, Germany; †Department of Structural Biology, Weizmann Institute, 76100 Rehovot, Israel; and ‡Max Planck Institute for Molecular Genetics, 14195 Berlin, Germany

Communicated by Alexander Rich, Massachusetts Institute of Technology, Cambridge, MA, September 24, 1999 (received for review August 23, 1999)

The electron density map of the small ribosomal subunit from *Thermus thermophilus*, constructed at 4.5 Å resolution, shows the recognizable morphology of this particle, as well as structural features that were interpreted as ribosomal RNA and proteins. Unbiased assignments, carried out by quantitative covalent binding of heavy atom compounds at predetermined sites, led to the localization of the surface of the ribosomal protein S13 at a position compatible with previous assignments, whereas the surface of S11 was localized at a distance of about twice its diameter from the site suggested for its center by neutron scattering. Proteins S5 and S7, whose structures have been determined crystallographically, were visually placed in the map with no alterations in their conformations. Regions suitable to host the fold of protein S15 were detected in several positions, all at a significant distance from the location of this protein in the neutron scattering map. Targeting the 16S RNA region, where mRNA docks to allow the formation of the initiation complex by a mercurated mRNA analog, led to the characterization of its vicinity.

crystallography of ribosomes | mRNA binding | 30S

Ribosomes are the universal cellular organelles on which protein biosynthesis takes place. They are nucleoprotein assemblies, built of two independent subunits of unequal size that associate on the initiation of protein biosynthesis. The small subunit (0.85 mDa) provides the site for the initiation step and facilitates the decoding of the genetic information. It contains 21 proteins and an RNA chain (16S) of ≈1,500 nucleotides. Significant conformational variability of 30S particles has been observed by cryoelectron microscopy studies (1, 2), by surface probing (3), and by monitoring the ribosomal activity (4).

The inherent flexibility of small ribosomal subunit may be the reason for the low (≈10 Å) resolution of the early crystals of the small ribosomal subunits from *Thermus thermophilus*, T30S (5, 6). It also may account for the unsuitability of all of the available cryoelectron microscopy models of the small ribosomal subunit for extracting initial phase sets, as performed successfully for the large ribosomal subunits (7). Indeed, increasing the homogeneity of the crystallized particles, accompanied by postcrystallization rearrangements, induced by minute amounts of a heteropolytungstate containing 18 W atoms (8), called here W18, resulted in diffraction to 3 Å.

This dramatic increase in crystal quality was not accompanied by changes in the unit cell dimensions or in the crystal symmetry. However, the W18-treated crystals (called Wative) could not be scaled to the original native crystals, suggesting that a major conformational rearrangement occurred upon the W18 treatment. It is conceivable that other metals could have led to a similar effect. Nevertheless, among the many tungsten compounds tested by us (9), only W18 was found suitable for the increase in resolution.

Conformational changes are not routinely induced within crystals because of the limitation of the motion imposed by the crystal network. However, the realization that the T30S crystals can tolerate such changes, prompted us to perform reactivation of the crystallized T30S particles by controlled heating (10). This procedure led to higher proportions of well diffracting crystals and enabled almost quantitative binding of compounds participating in protein biosynthesis or their analogs (1, 11).

Ribosomal crystallography has been found to be rather challenging, especially upon progressing to higher resolution. Consequently, the structure determination proceeds by step-wise approach, progressing from low to higher resolution. Furthermore, most of the interpretations of the currently available electron density maps hinge on models accommodating noncrystallographic structural information (3, 4, 12–19) and exploiting known structures of RNA and of isolated ribosomal proteins. Considerable uncertainties are associated with placements of structures determined at high resolution in medium resolution maps. In the case of the ribosome, special concern is require for minimizing potential ambiguities because its individual components contain common motifs (20, 21). In addition, molecular mimicries (22) may mislead the differentiation between proteins and RNA regions. The non-negligible conformational variability of the ribosomal components (20, 21), accompanied by possible influences of the *in situ* ribosomal environment, may also lead to misinterpretations.

To facilitate unbiased crystallographic identifications, to target sites involved in ribosomal functions, and at the same time to extend the resolution of heavy atom derivatives, we are focusing on the attachment of heavy atom markers to natural or genetically engineered probes at predetermined sites. We also exploit carriers that posses high specific affinities to ribosomal moieties, such as antibiotics or DNA oligomers complementary to exposed RNA regions. In this way, two surface cysteine residues as well as the 3′ end of the 16S RNA have been localized (11, 23, 24). Furthermore, in a few cases, the labeled crystals diffracted to resolution almost matching that of the Wative crystals and yielded data of adequate quality, presumably by reducing the flexibility of the targeted regions.

In this manuscript we present the 4.5 Å map of T30S and show the parts that have been interpreted so far. We focus on strategies and methodologies including the design, choice, and combination of derivatives. We show placements of RNA regions of known motifs as well as of ribosomal proteins of known structures. We also highlight the sites targeted by heavy atom markers, among them an mRNA analog.

Abbreviations: BS crystal, back-soaked crystal; TAMM, tetrakis(acetoxymercuri)-methane.

Data deposition: The atomic coordinates have been deposited in the Protein Data Bank, www.rcsb.org (PDB ID code 1C59).

§To whom reprint requests should be addressed. E-mail: yonath@mpgars.desy.de.

The publication costs of this article were defrayed in part by page charge payment. This article must therefore be hereby marked "*advertisement*" in accordance with 18 U.S.C. §1734 solely to indicate this fact.

Table 1. Phasing statistics

Data set	Unique reflections	Resolution, Å	Completeness (outer shell), %	R_{sym}, %	R_{merge}, %	Phasing power	R_{cullis}	Sites
	Soaking							
BS (Native)	85991	4.5*	93.2 (91.1)	10.8	—	—	—	—
Wative 1	56350	5.0	95.7 (99.6)	13.2	17.9	1.2	0.74	4
Wative 2	68335	4.4	81.5 (80.5)	12.3	16.6	1.5	0.77	3
Wative (anomalous)	42995	7.0	99.1 (99.6)	7.6	17.2	1.6/1.1†	0.4/0.8†	3
Ta_6Br_{14}	46690	6.0	68.0 (44.0)	14.2	26.6	1.4	0.84	3
$Hg_3C_6O_4H_8$‡	17092	6.5	60.1 (58.7)	14.4	22.9	1.3	0.73	7
$C_2Hg_6N_2O_8$	55800	5.9	79.6 (75.0)	6.9	21.7	1.7	0.50	4
PIP	62015	4.5	80.9 (80.3)	14.1	17.5	0.5	0.91	6
K_2O_4Os	49751	5.0	77.9 (84.4)	14.7	22.9	1.0	0.68	7
Pb_3-citrate‡§	26982	6.4	92.4 (75.2)	11.1	14.6	1.1	0.79	8
$NaAuCl_4$	30078	5.5	81.0 (78.0)	13.6	15.5	1.0	0.78	1
W_4	26748	6.4	91.8 (91.3)	11.8	15.0	0.9	0.72	4
K_2PtCl_4‡	23551	6.5	81.5 (78.5)	11.1	20.9	0.8	0.90	7
	Specific covalent binding or hybridization							
oliT‡§	36083	4.8¶	58.1 (60.6)	14.2	14.9	3.1	0.71	1
TAMM	25797	7.0	60.3 (61.5)	10.7	16.4	0.6	0.94	2
TIR‡§	43424	4.5	57.3 (16.3)	8.5	21.4	0.6	0.88	2
Methyl-Hg-acetate‡§	29719	6.0	80.6 (71.9)	13.7	16.2	1.2	0.66	6
Uranyl-acetate‡§	30911	6.0	84.4 (75.1)	12.3	15.3	0.5	0.85	5
	Derivatives with dual chemical properties							
AquaPt	28439	5.0	49.3 (59.3)	15.9	26.1	0.6	0.85	5
CisPt	19366	6.9	80.7 (70.3)	9.9	18.1	0.6	0.84	3

$R_{sym} = \Sigma|I - \langle I\rangle|/\Sigma\langle I\rangle$, $R_{merge} = \Sigma|F_{PH} - F_P|/\Sigma F_P$, $R_{cullis} = \langle$phase-integrated lack of closure$\rangle/\langle|F_{PH} - F_P|\rangle$, Phasing power $= \langle[|F_H(calc)|/$phase-integrated lack of closure$]\rangle$. PIP, diiodopiplatinum (II) diethyleneamine; W_4, (tetramethylammonium)$_2Na_2[Nb_2W_4O_{14}18H_2)]$; TIR, a tetrairidium cluster; aquaPt, *cis*-diaquacisplatin; cisPt; *cis*-$[Pt(NH_3)_4]$.

*Data were collected to 3 Å, but not used in this study.

†iso/ano.

‡SIR, not incorporated yet.

§Wative was considered as native.

¶Data were collected to 3.5 Å, but not used in this study.

Materials and Methods

Crystal Preparation. Ribosomal subunits from *T. thermophilus* were prepared and crystallized as described (5, 23). The crystals ($a = b = 407$ Å, $c = 176$Å, $P4_12_12$, hand determined from anomalous data) were treated by the addition of millimolar amounts of W18. Back-soaked (BS) crystals were generated by soaking the W18-treated crystals (Wative) in their stabilization solution for 10–40 hours. The content of W18 in the BS crystals was determined as described (9). Derivatization was performed by soaking the Wative crystals in heavy atom solutions, in the presence or in the absence of W18, as dictated by the stability of the crystals.

Site Targeting. Tetrakis(acetoxymercuri)-methane (TAMM) was covalently bound to exposed SH^- groups as described for the tetrairidium cluster in (24). TAMM mercuration of cDNA oligomers was performed on 5′ extensions of the oligomers containing thiolated bases. The non-oligomer-bound mercury atoms of the TAMM molecule were masked to avoid the attachment of the oligomers to undesired locations as described (11). The oligomer presented in these studies was (AGAAAG-GAGGTGATC), to which a tail of A(thio-dG)$_3$ was added.

Data Collection and Evaluation. Data were collected with a bright synchrotron beam at cryotemperature (86–90 K) from flash frozen crystals, as described (23). The data were recorded either on the 345 mm MAR Research (Hamburg) or charge-coupled device detectors [QUANTUM4 or APS2, Cornell High Energy Syncrotron Source (CHESS), Ithaca, NY] and were processed by HKL2000 (25). For anomalous data collection, the wavelength was adjusted to the L_3 edge of W. Collecting the 3–4 Å shell, decay was detected within a period sufficient for 1–1.5° oscillations. To facilitate the production of complete data sets, crystals were irradiated by a beam with a smaller cross-section. Translating the rod-like crystals (≈500 × 60 × 60 microns) once decay was observed allowed measurements from 2–6 separate regions. Larger cross sections were chosen when a less intense or divergent beam was provided. Under these conditions, however, only lower resolution data (<5–6 Å) could be collected.

Phasing. Because the original native crystals (5) became obsolete by the W18 treatment, Wative or BS crystals were considered "native," depending on the given soaking procedure. Data reduction, scaling, and initial phasing were performed with the CCP4 program package (26). The sites of W18 that were removed by the back-soaking procedure were identified in difference Patterson maps, and those that exist in the BS crystals were detected by using anomalous signals. The sites of the additional heavy atoms were determined and verified by difference Patterson and difference Fourier procedures. Refinement and phasing were carried out with the program SHARP (27). Heavy atom clusters, such as W18, Ta_6Br_{14}, tetrairidium, and TAMM were represented by their spherical averaged form factors, as implemented in SHARP (27). The initial 7 Å multiple isomorphous replacement map, obtained by W18 and Ta_6Br_{14}, was subjected to density modification by using the program SOLOMON (28), assuming a solvent content of 65%. The incorporation of phase information from derivatives diffracting to ≈6 Å resulted in a map with Figure of merit = 0.59 and $R_{cullis} = 0.75$. The resolution of the map was extended to 4.5 Å in steps by the incorporation of phase information from additional heavy atom derivatives (Table 1). After tracing of ≈500 nucleotides, the model, ac-

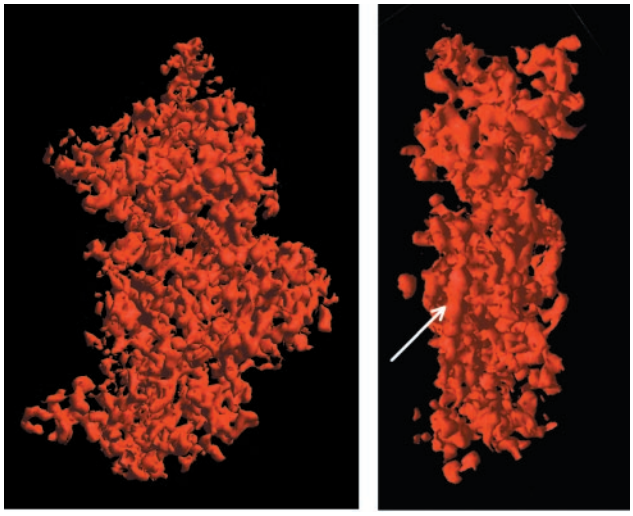

Fig. 1. Two orthogonal views of the overall structure of the small subunit, as extracted from the 4.5 Å map (contour level 1.2 SD). The arrow points at an exceptionally long dense region, suitable to host double-helical RNA chain that may be interpreted as helix 44 in the model of the 16S RNA (18).

counting for ≈28% of the total mass, was subjected to rigid-body refinement. The phases generated from the refined positions were combined with those originating by multiple isomorphous replacement. This step was carefully monitored by the introduction of several weighing procedures, as well as by the temporary removal of parts of the model used for phase combination.

Map Interpretation. Fitting was carried out by following the features of the map. Building blocks were constructed from known RNA motifs (canonical RNA A-form, hammer head, anticodon loop, sarcin/ricin loop, archaeal bulge-helix-bulge, pseudoknot, specific kinks and turns, etc.) or from the ribosomal proteins whose structures have been determined crystallographically or by NMR (20, 21). Tracing was performed interactively, using the program O (29). The results were displayed either by O or by RIBBONS (30).

Results and Discussion

The initial 7 Å as well as the current 4.5 Å maps contain shapes with a morphology remarkably similar to most of the cryoelectron microscopy reconstructions (1, 2, 12, 13) of small ribosomal subunits. They show the consensus division into a "head" connected by a short "neck" to a bulky lower "body" (Fig. 1) and contain elongated dense features alongside lower-density globular regions.

The 7 Å resolution map was found suitable for initial fittings of both RNA chains and protein structures. At around 6 Å, the number of the RNA duplexes that appeared as separated chains became larger. At 4.5 Å, a larger number of regions suggesting

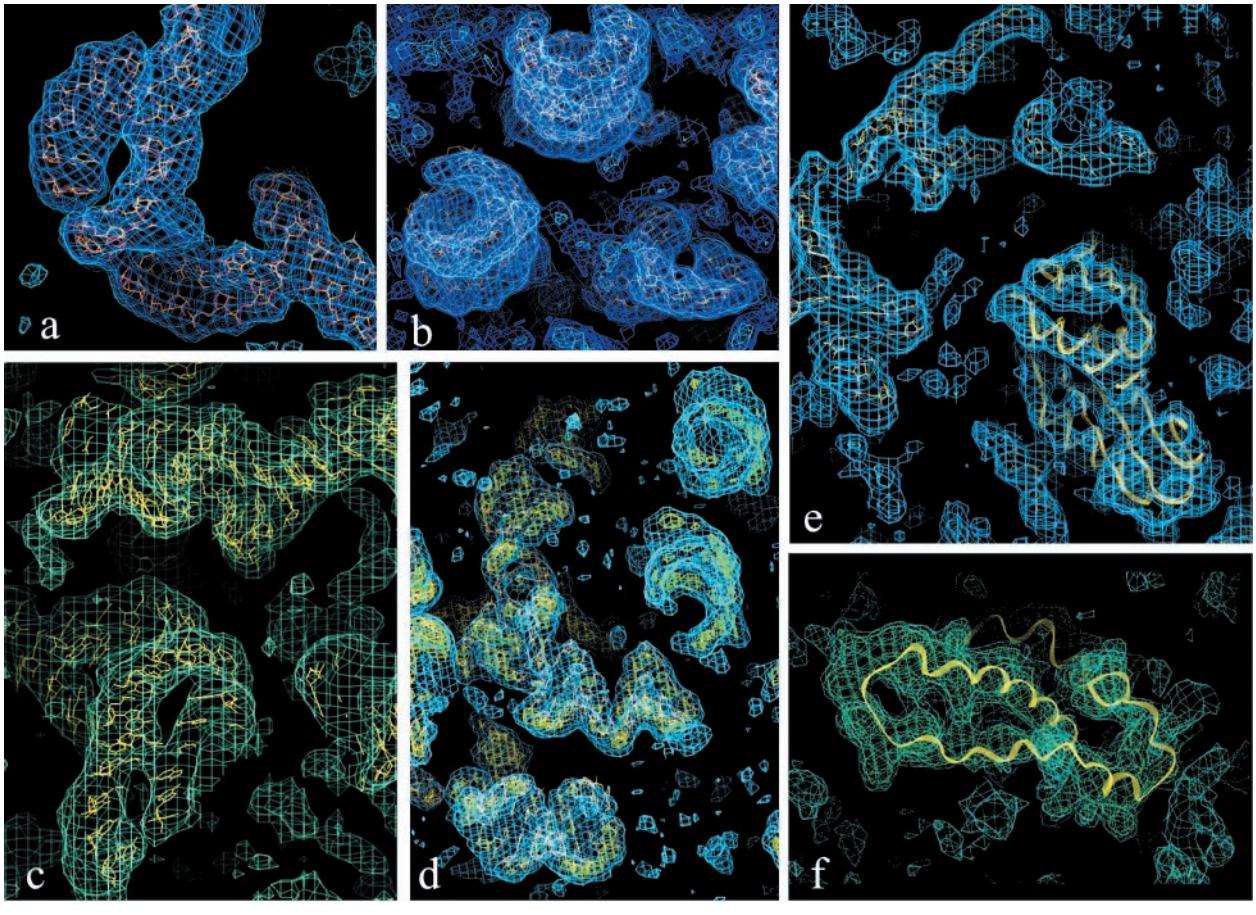

Fig. 2. Parts of the T30S electron density maps at different stages of structure determination from 6 to 4.5 Å (contour level 1 SD, unless otherwise mentioned). (*a*) A helix-bulge-helix region, traced at 6 Å resolution. (*b* and *c*) Views of A-form RNA regions within the 4.5 Å map. (*d*) Part of the 4.5 Å map, contoured at 1.5 (cyan) and 2.5 (green-yellow) SD. These levels were chosen to avoid background noise and to highlight the phosphates in the RNA backbone, respectively. (*e* and *f*) The regions of the 4.5 Å map assigned to protein TS5 and TS15, respectively. In *f*, the less well defined helix was found to be flexible in isolation by NMR and x-ray (21).

prominent protein folds were detected, and the phosphates belonging to the RNA backbone appeared as bulges. Density accounting for the bases could be seen (Fig. 2), but individual bases were still not well resolved, similar to the observations made at comparable resolution in several other systems (31–34). Although the current resolution is too low to suggest novel structural motifs, indications for them were nevertheless detected in the course of map interpretation.

We have previously reported experiments in which tetrairidium attached to exposed cysteines revealed the locations of proteins TS11 and TS13 at 6–7 Å resolution (11, 24). The position of TS13 is compatible with that suggested by immunoelectron microscopy (14), neutron scattering (16), and modeling experiments (19). However, the position of the surface of TS11 deviates from the neutron scattering map by a distance larger than the expected diameter of this protein. These results have been confirmed by using TAMM instead of tetrairidium. Furthermore, the availability of a map of a higher detail allowed the examination of the vicinity of the bound heavy atom compounds. It was found that the cysteine of TS13 is located in a region rich in features interpretable as α helices and β sheets whereas the quality of the map in the vicinity of TS11 is somewhat lower.

The structures of ribosomal proteins that have been determined crystallographically or by NMR (20, 21) were exploited for visual placements, keeping in mind that these assignments are only partially justified. Guidelines were taken from the large volume of noncrystallographic studies. In these experiments, proteins TS5 and TS7 (Fig. 2) were found to be in the vicinity of the positions suggested for them by earlier noncrystallographic studies (14, 16, 19). The case of protein TS15 is more complicated because several regions suitable to accommodate its core could be identified in the map. As the core of protein S15 contains well packed α helices (reviewed in refs. 20 and 21), a structural element that is likely to be common among ribosomal proteins, this finding was not surprising. In neither of the potential positions of protein S15, the remaining part of this protein, a flexible arm, could be well placed (Fig. 2). All of these positions are rather far from the location of S15 in the neutron scattering map (16). Hence, the region closest to the location of S15 in the neutron density map was tentatively chosen (Fig. 3). It is noteworthy that several additional regions suitable to accommodate ribosomal proteins were identified but still not assigned. Of interest is a region that seems to be rich in loosely packed α helices, located at the protein-free part of the neutron scattering map (16), at the bottom of the particle.

Hybridization of exposed RNA regions with mercurated cDNA oligomers was found to be useful for independent site identifications as well as for monitoring ribosomal functional activities. The following example is illuminating. The oligomer complementary to the 3′ end of the 16S RNA (called here oliT) was found to hybridizes well even as its TAMM mercurated form. Furthermore, despite its large-size, which may reach 70 Å in length, it readily diffused into the crystals that were found to diffract to resolutions comparable to that of the Wative or BS crystals. Indications for the location of its mercurated tail were obtained first at 7.5 Å resolution (11). Extending these studies to the current resolution allowed an analysis of the vicinity of this site, which, as expected, contains a rather long single stranded RNA chain (Fig. 3). It also led to more accurate positioning of the 5′ end of the cDNA oligomer.

This oligomer is of high functional relevance, as it contains the Shine-dalgarno sequence, thus imitating the mRNA segment involved in the initiation of protein biosynthesis. It was designed to dock at the 3′ end of the 16S RNA that contains the anti-Shine-Dalgarno sequence, and to mimic the formation of the initiation complex. This region of the 16S chain is known to be rather flexible and may adopt several conformations (19). Hence, it is suggested that the high quality diffraction obtained from the crystals derivatized by this oligomer results from stabilization of the flexible 3′ arm of the 16S RNA in a fashion that mimics its binding to mRNA.

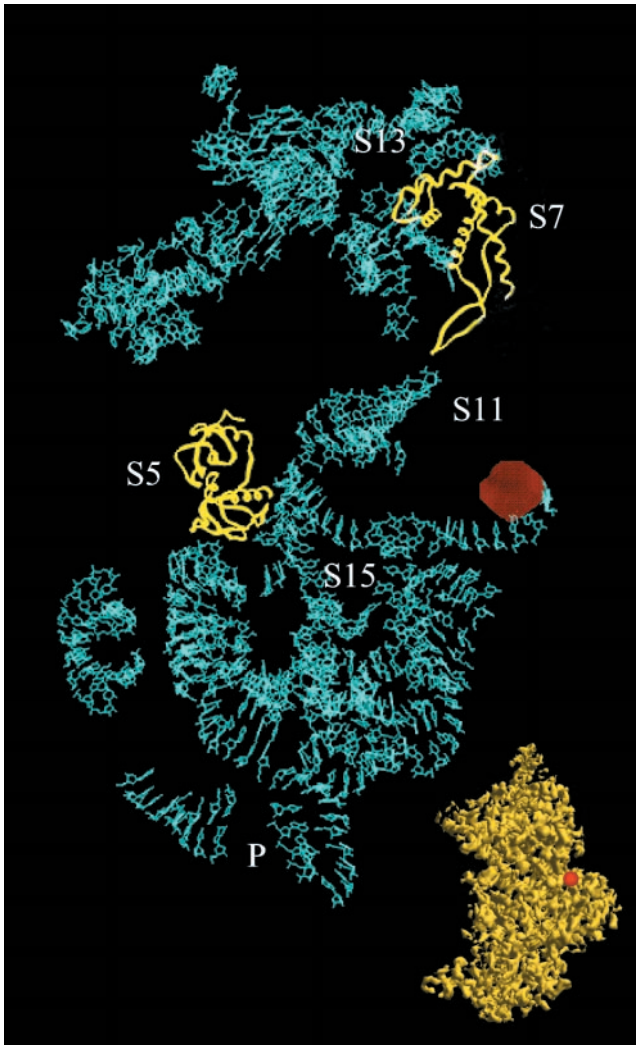

Fig. 3. Most of the so far traced RNA chain (in cyan). The position of the center of mass of the TAMM molecules that were bound to the mRNA analog is shown as a red sphere (of artificially enlarged size). The locations of proteins TS5, TS7 are represented by their backbone structure, as determined crystallographically. The tentative locations of the center of protein TS15 and of the exposed cysteines of proteins TS11 and TS13 are marked by their numbers. P shows a possible location for a still-not-assigned protein. For orientation, the oliT position has been placed on the body of T30S subunit (shown in the lower-right insert).

It is still premature to determine whether the site revealed in the current map reflects the position of the 3′ end of 16S RNA at its free, 50S bound, or intermediate conformations. Interestingly, the position assigned for the 5′ end of this oligomer was found to be at close proximity to one of the major sites of W18. Because both the polyanion cluster and the RNA chains are negatively charged, it is conceivable that their interactions are mediated by Mg^{2+} ions. Regardless of the mode of the interactions, it is likely that the gain of resolution by the W18 treatment is a result of minimizing the flexibility of the RNA chains. Indeed, so far, all W18 sites were detected in positions that may significantly reduce the mobility of the T30S particles within the crystal network. Thus, two of the main W18 sites were detected at the interface between the two paired particles, indicating a possible involvement of W18 in the pairing contacts.

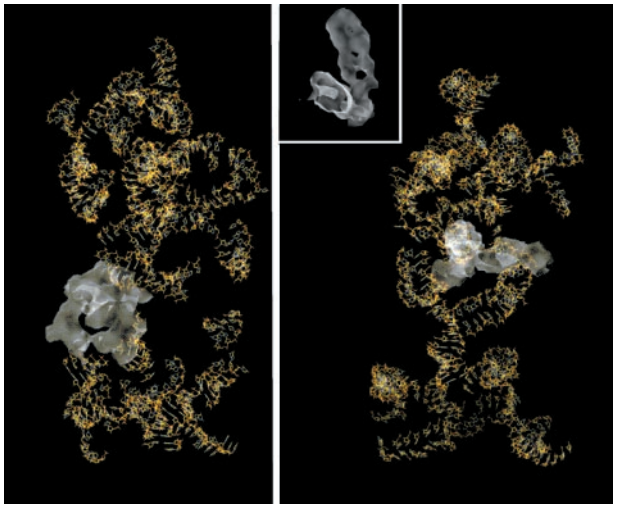

Fig. 4. The regions that became interpretable by the incorporation of the anomalous data, shown as white objects. The insert focuses on one of them, traced later as helix-bulge-helix motif.

To gain confidence in the 4.5 Å map, it was screened for structural features that were not detected in the lower resolution maps. Among those, a prominent spherical object of a size comparable to that of the W18 cluster was clearly seen. Also, the contribution of the W anomalous signals provided additional verification for the quality of both the multiple isomorphous replacement and the multiple isomorphous replacement with anomalous signals maps, as it led to marked improvement in several regions, two of which are shown in Fig. 4. Finally, several portions of the modeled RNA chain were removed before its use for phase combination, and the map resulting from the combined phases was examined. Some variability in map quality was evident. Nevertheless, in many positions, considerable improvement in the map was detected (Fig. 5), and RNA regions that were not used in the phase combination procedure could be clearly visualized.

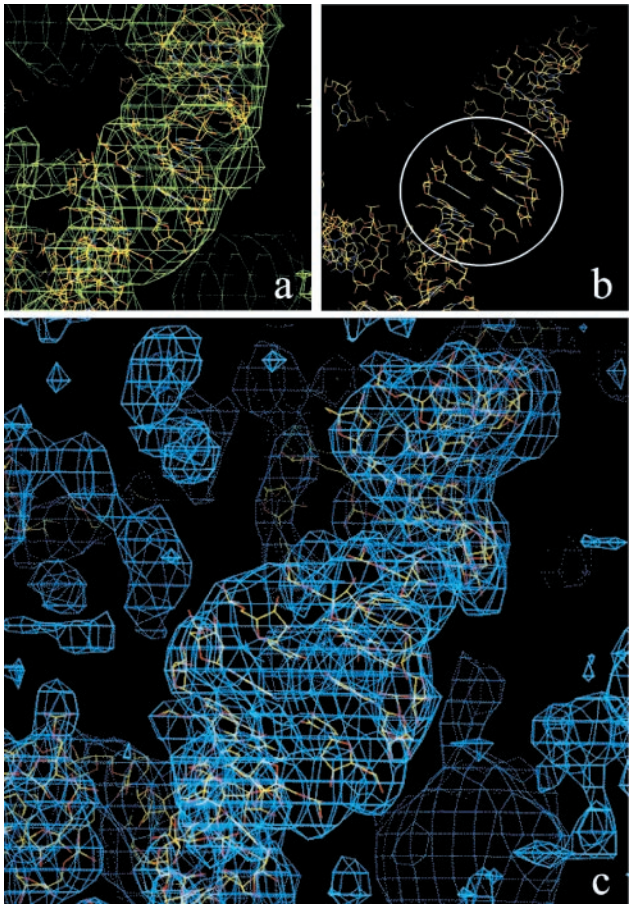

Fig. 5. (*a*) A region of the 7 Å map and its interpretation before phase combination. The portion of the modeled RNA that was removed before phase combination (highlighted by a circle). (*c*) The comparable part of the phase-combined 5 Å map, showing the features detected at the surroundings of the removed part.

Conclusions

The unbiased structural information revealed in this study is consistent with most of the available noncrystallographic data, but at the same time it presents some deviations. Careful inspection of the current map resulted in the identification of a wealth of commonly occurring as well as rarely found structural elements. However, it is clear that, at this stage, detailed functional assignments are bound to depend heavily on models created according to biochemical and biophysical considerations. Because we have shown that selected ribosomal sites can be targeted within the crystals, and because data are being collected to higher resolution, there are solid reasons to expect that a reliable and unbiased interpretation, capable of shedding light on intricate functional issues, will soon emerge.

Note. Two related crystallographic studies, albeit performed at lower resolution, were published during the reviewing period of this manuscript. These report assignments of ribosomal components within maps of the small (35) and the large (36) subunit, in a fashion based exclusively on the existing noncrystallographic ribosomal models. Interestingly, the upper part of the 5.5 Å small subunit structure (35) appears to be less well resolved, compared with that reported here. This may be attributable to the postcrystallization activation step used by us.

We thank M. Wilchek for indispensable advice, M. Pope, W. Jahn, and W. Preetz for heavy atom compounds, M. Safro and I. Levin for active participation, R. Brimacombe and F. Müller for the 16S model, W. Traub for fruitful discussions, and R. Albrecht, T. Auerbach, H. Avila, W. S. Bennett, H. Burmeister, C. Glotz, Y. Halfon, M. Kessler, K. Knaack, M. Laschever, S. Meier, J. Müssig, M. Pioletti, M. Peretz, C. Radzwill, M. Simitsopoulou, S. Weinstein, and R. Zarivach for contributing to different stages of these studies, and to the synchrotron radiation facilities staff: European Molecular Biology Laboratory and Max Planck Group beam lines at Deutsches Elektronen Synchrotron; F1/Cornell High Energy Syncrotron Source; ID2 and ID13 at the European Syncrotron Radiation Facility; and ID19/APS at Argonne National Laboratory. Support was provided by the Max-Planck Society, the National Institutes of Health (Grant GM 34360), the German Ministry for Science and Technology (Bundesministerium für Bildung, Wissenschaft, Forschung und Technologie Grant 05-641EA), and the Kimmelman Center for Macromolecular Assembly at the Weizmann Institute. A.Y. holds the Martin S. Kimmel Professorial Chair.

1. Harms, J., Tocilj, A., Levin, I., Agmon, I., Stark, H., Kolln, I., van Heel, M., Cuff, M., Schlunzen, F., Bashan, A., *et al.* (1999) *Structure Fold. Des.* **7,** 931–941.
2. Gabashivili, I. S., Agrawal, R. K., Grassucci, R. & Frank, J. (1999) *J. Mol. Biol.* **286,** 1285–1291.
3. Wang, R., Alexander, R. W., VanLoock, M., Vladimirov, S., Bukhtiyarov, Y., Harvey, S. C. & Cooperman, B. S. (1999) *J. Mol. Biol.* **286,** 521–540.
4. Tapprich, W. E. & Hill, W. E. (1986) *Proc. Natl. Acad. Sci. USA* **83,** 556–560.
5. Yonath, A., Glotz, C., Gewitz, H. S., Bartels, K., von Boehlen, K., Makowski, I. & Wittmann, H. G. (1988) *J. Mol. Biol.* **203,** 831–833.
6. Trakhanov, S. D., Yusupov, M. M., Agalarov, S. C., Garber, M. B., Ryazantsev, S. N., Tischenko, S. V. & Shirokov, U. A. (1987) *FEBS Lett.* **220,** 319–322.

7. Ban, N., Freeborn, B., Nissen, P., Penczek, P., Grassucci, R. A., Sweet, R., Frank, F., Moore P. & Steitz, T. (1998) *Cell* **93,** 1105–1115.
8. Dawson, B. (1953) *Acta Crystallogr.* **6,** 113–126.
9. Yonath, A., Harms, J., Hansen, H. A., Bashan, A., Schlunzen, F., Levin, I., Koelln, I., Tocilj, A., Agmon, I., Peretz, M., *et al.* (1998) *Acta Crystallogr. A* **54,** 945–955.
10. Zamir, A., Miskin, R. & Elson, D. (1971) *J. Mol. Biol.* **60,** 347–364.
11. Auerbach, T., Pioletti, M., Avila, H., Anagnostopoulos, K., Weinstein S., Franceschi, F. & Yonath, A. (1999) *Biomol. Struct. Dyn.*, in press.
12. Stark, H., Mueller, F., Orlova, E. V., Schatz, M., Dube, P., Erdemir, T., Zemlin, F., Brimacombe, R. & van Heel, M. (1995) *Structure (London)* **3,** 815–821.
13. Frank, J., Zhu, J., Penczek, P., Li, Y., Srivastava, S., Verschoor, A., Radermacher, M., Grassucci, R., Lata, A. R & Agrawal, R. K. (1995) *Nature (London)* **376,** 441–444.
14. Stöffler, G. & Stöffler-Meilicke, M. (1986) in *Structure, Function and Genetics of Ribosomes*, eds. Hardesty, B. & Kramer, G. (Springer, Heidelberg), pp. 28–46.
15. Oakes, M. I., Clark, M. W., Henderson, E. & Lake, J. A., (1986) *Proc. Natl. Acad. Sci. USA* **83,** 275–279.
16. Moore, P. B., Capel, M. S., Kjeldgaard, M. & Engelman, D. M. (1985) in *Structure, Function and Genetics of Ribosomes*, eds. Hardesty, B. & Kramer, G. (Springer, Heidelberg), pp. 87–100.
17. Merryman, C., Moazed, D., McWhirter, J. & Noller, H. F. (1999) *J. Mol. Biol.* **285,** 97–105.
18. Malhotra, A. & Harvey, S. C. (1994) *J. Mol. Biol.* **240,** 308–340.
19. Müller, F. & Brimacombe, R. (1997) *J. Mol. Biol.* **271,** 524–544.
20. Liljas, A. & Al-Karadaghi, S. (1997) *Nat. Struct. Biol.* **4,** 767–771.
21. Ramakrishnan, V. & White, S. W (1998) *Trends Biochem. Sci.* **3,** 208–212.
22. Nyborg, J., Nissen, P., Kjeldgaard, M., Thirup, S., Polekhina, G., Clark, B. F. C. & Reshetnikova, L. (1996) *Trends Biochem. Sci.* **21,** 81–82.
23. Schlünzen, F., Koelln, I., Janell, D., Gluehmann, M., Levin, I., Bashan, A., Harms, J., Bartels, H., Auerbach, T., Pioletti, *et al.* (1999) *J. Synth. Radiation* **6,** 928–941.
24. Weinstein, S., Jahn, W., Glotz, C., Schluenzen, F., Levin I., Janell, D., Harms, J., Kolln, I., Mansen, H. A. S., Gluehmann, M., *et al.* (1999) *J. Struct. Biol.* **127,** 141–151.
25. Otwinowski Z. & Minor, W. (1997) *Methods Enzymol.* **276,** 307–326.
26. CCP4 Collaborative Computational Project (1994) *Acta Crystallogr. D* **50,** 760–763.
27. La Fortelle E. & de Bricogne, G. (1997) *Methods Enzymol.* **276,** 472–494.
28. Abrahams, J. P. & Leslie, A. G. W. (1996) *Acta Crystallogr. D* **52,** 30–42.
29. Jones, T. A., Zou, J.-Y., Cowan, S. W. & Kjeldgaard, M. (1991) *Acta Crystallogr. A* **47,** 110–119.
30. Carson, M. (1991) *J. Appl. Crystallogr.* **24,** 958–961.
31. Wolberger, C., Ding, Y., Ptashne, M. & Harrison, S. H. (1988) *Nature (London)* **335,** 789–795.
32. Jaeger, J., Restle, T. & Steitz, T. A. (1998) *EMBO J.* **17,** 4535–4542.
33. Price, S., Cusack, S., Borel, F., Berthetcolominas, C. & Leberman, R. (1993) *FEBS Lett.* **324,**167–170.
34. Golden, B., Gooding, A. R., Podell, E. R. & Cech, T. A. (1998) *Science* **282,** 259–264.
35. Clemons, W. M., Jr., May, J. L., Wimberly, B. T., McCutcheon, J. P., Capel, M. S. & Ramakrishnan, V. (1999) *Nature (London)* **400,** 833–840.
36. Ban, N., Nissen, P., Hansen, J., Capel, M., Moore, P. B. & Steitz, T. A. *Nature (London)* **400,** 841–847.

Cell, Vol. 102, 615–623, September 1, 2000, Copyright ©2000 by Cell Press

Structure of Functionally Activated Small Ribosomal Subunit at 3.3 Å Resolution

Frank Schluenzen,*‖ Ante Tocilj,*‖ Raz Zarivach,† Joerg Harms,* Marco Gluehmann,* Daniela Janell,* Anat Bashan,† Heike Bartels,† Ilana Agmon,† François Franceschi,‡§ and Ada Yonath*†

*Max-Planck-Research Unit for Ribosomal Structure
22603 Hamburg
Germany
†Weizmann Institute
76100 Rehovot
Israel
‡Max-Planck-Institute for Molecular Genetics
14195 Berlin
Germany

Summary

The small ribosomal subunit performs the decoding of genetic information during translation. The structure of that from *Thermus thermophilus* shows that the decoding center, which positions mRNA and three tRNAs, is constructed entirely of RNA. The entrance to the mRNA channel will encircle the message when a latch-like contact closes and contributes to processivity and fidelity. Extended RNA helical elements that run longitudinally through the body transmit structural changes, correlating events at the particle's far end with the cycle of mRNA translocation at the decoding region. 96% of the nucleotides were traced and the main fold of all proteins was determined. The latter are either peripheral or appear to serve as linkers. Some may assist the directionality of translocation.

Introduction

Ribosomes are the universal ribonucleoprotein particles that translate the genetic code into proteins. They are built of two subunits, which associate upon initiation of protein synthesis. The large subunit (1.45 MDa in bacterial ribosomes) catalyzes the peptide bond formation and provides a path for the nascent polypeptide chain. The small subunit (0.85 MDa) initiates mRNA engagement, decodes the message, governs mRNA and tRNA translocation, and controls fidelity of codon–anticodon interactions.

Recent reports describe crystallographically determined low- and medium-resolution partial structures for the intact ribosome (70S) from *T. thermophilus,* at 7.8 Å (Cate et al., 1999), the large subunit from *Haloarcula marismortui,* at 5 Å (Ban et al., 1999), the small (30S) subunit from *T. thermophilus,* at 5.5 Å (Clemons et al., 1999), and the activated form of this subunit, at 4.5 Å (Tocilj et al., 1999). Advances in electron cryomicroscopy (cryo-EM) have also revealed new features of ribosomal particles and their complexes (Gabashvili et al., 1999b, 2000; Stark et al., 2000). In parallel, the structures of several ribosomal protein–RNA complexes have been determined at high resolution (Conn et al., 1999; Wimberly et al., 1999; Agalarov et al., 2000; Nikulin et al., 2000).

The small ribosomal subunit from *T. thermophilus* contains 19 proteins (Tsiboli et al., 1994), a small polypeptide of 26 amino acids, called Thx (Choli et al., 1993) and an RNA chain, called 16S, of 1518 nucleotides (Murzina et al., 1988). Base pairing and stacking interactions induce local folding of most of this long RNA chain, resulting in multiple junctions of helical regions, frequently interrupted by mismatches and internal bulges. The structure of the small subunit, presented here at 3.3 Å resolution (Figure 1), is an essentially complete molecular description. It includes 1457 nucleotides and most of the fold of all 19 proteins belonging to this particle. It shows known as well as newly detected folding and packing motifs. It provides insight into the decoding mechanism and its universality, and highlights the role of selected components in maintaining the sophisticated architecture of the ribosome.

Results and Discussion

Structure Determination

The 3.3 Å resolution map (Figure 1 and Table 1), obtained by multiple isomorphous replacement and anomalous scattering (MIRAS) is sufficiently clear that most of the structure could be traced. In many regions bases were well separated and purines and pyrimidines could be assigned. Likewise, many of the proteins loop and side chains could be identified. The ribosome is a molecular machine with multiple states, and particular segments are likely to be disordered in any one of these states. Although improvement is expected at higher resolution, we believe that most of the less well resolved map regions, accounting for less than 4% of all nucleotides, show that these RNA segments are indeed flexible.

Our structure contains most of the 16S nucleotides and all the proteins of the 30S subunit. Localization of the proteins was based on the large body of noncrystallographic information, as described in (Tocilj et al., 1999). We placed the structures of S4, S5, S6, S7, S8, S15, S17, S18, and S19, as determined by X-ray crystallography or NMR (Ramakrishnan and White, 1998; Helgstrand et al., 1999; Agalarov et al., 2000) and identified density that should account for most of the parts of these proteins that were not determined in isolation. We also identified parts of the known structures that seem to assume different conformations within the ribosome. In addition, we traced, fully or partially, proteins S2, S3, S9, S10, S11, S12, S13, S14, S16, and S20. As for the above, the positioning of these proteins was based on the available biochemical, biophysical, and functional data. We confirmed the positions of S11 and S13 by the independent localization of heavy-atom clusters that were bound to their exposed cysteines prior to crystallization (Weinstein et al., 1999).

§To whom correspondence should be addressed (e-mail: franceschi@molgen.mpg.de).
‖These authors contributed equally to the work.

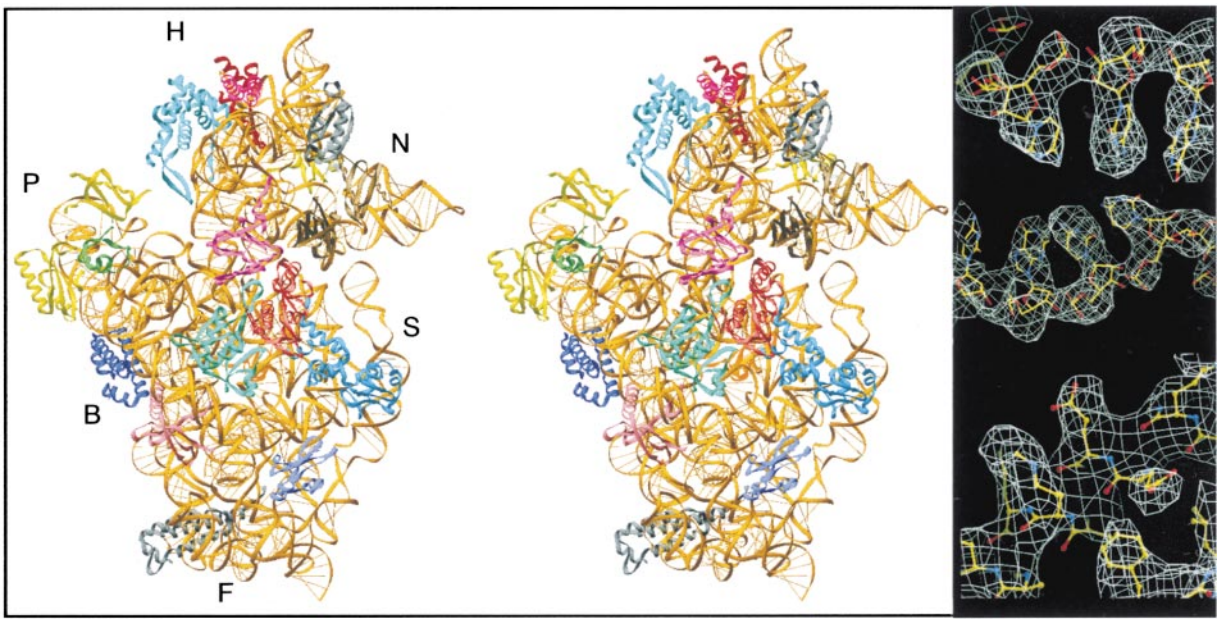

Figure 1. The Small Subunit and Its Electron Density Map

(Left and center) A stereo representation of the full model described in this paper. RNA is shown in gold, using a ribbon backbone and simple lines for base pairs. The differently colored helical segments and loops are the proteins. The major subdivisions are labeled: H, head; B, body; S, shoulder; P, platform; N, nose; F, foot.

In all figures, the head is at the top of the drawing and the foot at the bottom.

These portions of Figures 1–3 were made with Ribbons (Carson, 1997).

(Right) Segments showing RNA (top and middle pannels) and proteins (bottom) of the MIRAS map at 3.3 Å resolution, with the model superimposed. Made with O (Jones and Kjeldgaard, 1997).

Global Organization of the Small Subunit

The particle that emerges from our map (Figure 1) contains the morphological features familiar from cryo-EM reconstructions. The traditional subdivisions are the "head," "neck," and "body"; the body has a "shoulder," a "platform," and a "foot" with a "toe" (called also "spur"). The head has a "nose" with a further protuberance, the "beak."

Three long helices, called here "longitudinal" to designate their direction, H44, H7, and H16/H17 (Figure 2) run parallel to the long axis of the subunit (vertically in the view in Figure 1). Among them H44 and H16/H17 are located on the rather flat surface that faces the 50S subunit. The three longitudinal helices are linked by transverse features, placed like ladder rungs between them. Principal among these transverse helices are H21-H23 (Figure 2), which lie in an inclined lune extending from the shoulder to the platform. The head contains mainly short helices, in marked contrast to the long duplexes of the body. It has a bilobal architecture, with H34 serving as the bridge between hemispheres (Figure 2). The head joins the body through a single RNA helix, H28 which appears to act as a hinge. In addition, the upper part of the shoulder (H16/H18) and the lower part of the nose (H33/H34) form a noncovalent body–head connection (Figures 1 and 3). We refer to this interaction as the "latch." It surrounds the entrance to an elongated, curved channel, proposed by us to be the conduit for the mRNA chain, based on previous structural studies (Arad et al., 1987; Mueller et al., 1997; Cate et al., 1999).

All the major functional features of the subunit consist of RNA elements; the proteins appear to serve largely as struts, linkers, and supports. Of interest are long extensions of proteins which penetrate into rRNA regions, similar to those detected in the nucleosome (Luger et al., 1997). Some of them reach distal proteins. For example, protein S12 contains a long tail which spans the particle, extending toward S17 (Figure 2). Parts missing in the available crystallographic or NMR structures that were readily traced in our map are an α-helical region at the N terminus of S5, a β strand protruding from S7, and a short arm originating at S18 and pointing toward S6.

Only one protein, S12, is located at the RNA-rich surface that interacts with the large subunit. Two additional proteins, S7 and S15, that are located at the rims of the subunit interface region, are partially involved in tRNA binding or in intersubunit contacts, respectively. A few proteins, such as S4, S5, S8, and S12 may contribute to the fidelity and the directionality of the translocation (see below). About half a dozen are peripheral, located on the particle's surface, at its solvent side. These may have evolved at later stages to fine tune the complex tasks and intricate recognitions required for the decoding process. They also may prevent nonproductive interactions with the large subunit or the initiation factors.

The Decoding Center and Its Vicinity

The decoding center organizes mRNA and tRNA translocation and controls fidelity in codon–anticodon interactions (Green and Noller, 1997). It is located at the upper part of the body and the lower part of the head. Mapping the conserved nucleotides in the 16S RNA on our structure showed remarkable conservation around this region, in accord with the universality of the decoding

Table 1. MIRAS Phasing Statistics

Data Collection	Wative 1	Wative 2	Backsoak	Ir	IrG	Os	Ta_6Br_{12}
Reflections	2,186,910	327,448	725,465	154,875	218,049	82,258	99137
Unique reflections	206,724	133,199	122,788	45,748	71,096	25,593	48132
Completeness	94.7 (77.1)	80.5 (73.1)	86.4 (82.8)	91.3 (95.2)	69.3 (68.2)	70.4 (42.8)	56.1 (38.5)
Mean [I/sigma(I)]	21.9 (3.6)	12.3 (2.8)	14.5 (3.3)	11.5 (6.7)	10.7 (3.9)	12.8 (4.9)	10.5 (3.1)
R_{sym}	13.6 (44.1)	10.6 (29.4)	12.7 (34.7)	11.3 (34.2)	12.4 (24.8)	10.3 (46.3)	14.3 (33.2)
D_{min} (Å)	3.3	3.5	3.8	5.4	4.5	5.8	5.0
Phasing							
Sites	13[b]	10[b]	8[b]	14	4	15	5
R_{cullis} (centric)	—	0.67	0.60	0.64		0.87	0.82
R_{cullis} (acentric)[a]	—/0.80	0.76/0.66	0.72/0.56	0.80/0.83	0.75/0.66	0.87/0.63	0.88/—
PP (centric)	—	0.64	1.14	0.98	0.79	1.06	0.98
PP (acentric)[a]	—/0.65	0.70/0.94	1.22/0.75	1.21/0.85	0.96/1.13	1.32/0.73	1.13/—

PP: phasing power = <|Fh(calc)|>/<phase-integrated lack of closure. R_{cullis} = <phase-integrated lack of closure>/<|Fph − Fp|>. R_{cullis} and phasing power were obtained from SHARP. The compounds used for derivatization have been described in (Tocilj et al., 1999) except for Ir = sodium-Ir chloride. Additional minor heavy atoms used for phasing have been omitted from this table. The overall figure of merit (FOM) was 0.48 after MIRAS phasing with SHARP, and 0.78 after density modification with SOLOMON.

[a] Isomorphous/anomalous. Highest resolution bins are given in brackets.

[b] Number of W_{18} sites. Among them four were represented by individual atoms, the remaining sites by their spherically averaged form factor.

process. This region contains the upper part of H44, H45, the 3′ and 5′ ends of the 16S RNA, the switch helix (Lodmell and Dahlberg, 1997), H27, the central pseudoknot, H1/H2, and the stem loop of H18, and the main transverse head element, H34 (Figure 2).

The most prominent feature in the decoding center is the upper portion of H44 (also called the "penultimate stem"), which bends toward the neck. H44 forms much of the intersubunit contact in the assembled ribosome (Cate et al., 1999); its upper bulge—nucleotides 1492–1498 and their base pairs 1402–1408 (*E. coli* numbering)—form the A and P tRNA sites. The terminal helix, H45, packs between H44 and H24 and leads to the 3′ end of the 16S RNA. The 3′ segment is known to be highly flexible and contains the region that pairs with the trigger (Shine-Dalgarno) sequence in the mRNA, an interaction critical for initiation of protein synthesis. The switch helix can undergo changes in its base-pairing scheme; these may induce cooperative rearrangements that lead to movements of the platform, shoulder, and head (Gabashvili et al., 1999b). Thus, the global conformational state of the particle may be correlated with the base-pairing scheme of H27 (Lodmell and Dahlberg, 1997). We see in our map the conformation called 912–885 (*E. coli* numbering). As expected, the opening of the central pseudoknot is not observed, consistent with the importance of the integrity of the pseudoknot for the functionality of the ribosome (Poot et al., 1998).

H27 packs groove-to-groove with the upper end of H44, which is the target of amino-glycoside antibiotics. The structure of an RNA-paromomycin complex (Fourmy et al., 1998) indicates that the antibiotic causes the upper stem of H44 to bend toward H27; this bending may, in turn, induce a displacement of H27 toward S5. Such coordinated movement is permitted by the structure we see; it could explain the differences in streptomycin protection patterns observed in naked 16S rRNA and in complete 30S particles (Spickler et al., 1997), as well as the relations between mutations in H27 (Lodmell and Dahlberg, 1997) and the ribosomal ambiguity (*ram)* as well as the restrictive mutations.

The structural elements of the decoding center create between the head and the body an elongated, curved channel, which we assigned as the path of the mRNA. The loop of H18 is located near the entrance to this channel. In our structure it bends toward the decoding center, in agreement with crosslinking data (Powers and Noller, 1991; Bullard et al., 1998). Connecting between regions known to be mobile, and interacting with the incoming mRNA (Dontsova et al., 1992), this region may assume more than one conformation unless it is stabilized. Indeed, this region is somewhat less well defined in our map.

The positions of mRNA and tRNA in the decoding center were determined by reference to the structure (at 7.8 Å resolution) of a tRNA-70S complex (Cate et al., 1999). The entire penultimate stem is clearly defined in that structure, so we superposed this region onto our electron density map (Cate et al., 1999 and PDB entry 486D). Only a small shift was then needed to achieve a remarkable fit of the tRNA and mRNA codons with the geometry of the decoding center (Figure 3). The required shift, smaller than 6 Å, may be linked to the conformational rearrangements that the small subunit undergoes upon incorporation into the 70S particle or consequent to the binding of the mRNA/tRNA molecules. Alternatively, it may be due to the uncertainties of the limited resolution of the 70S map. We also found similarities between the shape of the decoding center seen in our structure and the contour of the corresponding part of the NMR structure of a 26-mer oligonucleotide of *E. coli* sequence (Fourmy et al., 1998) and with that adopted from it in modeling attempts (VanLoock et al., 1999).

An important conclusion, illustrated in Figure 3, is that the anticodon loops of the A and P site tRNAs and the codon segments of the mRNA do not contact any ribosomal proteins. The configuration of the 16S RNA therefore determines the precise arrangement of the interacting elements and enforces precision in codon–anticodon interactions. As seen at lower resolution in the structure of the 70S complex (Cate et al., 1999), the shape of the mRNA channel at the vicinity of the

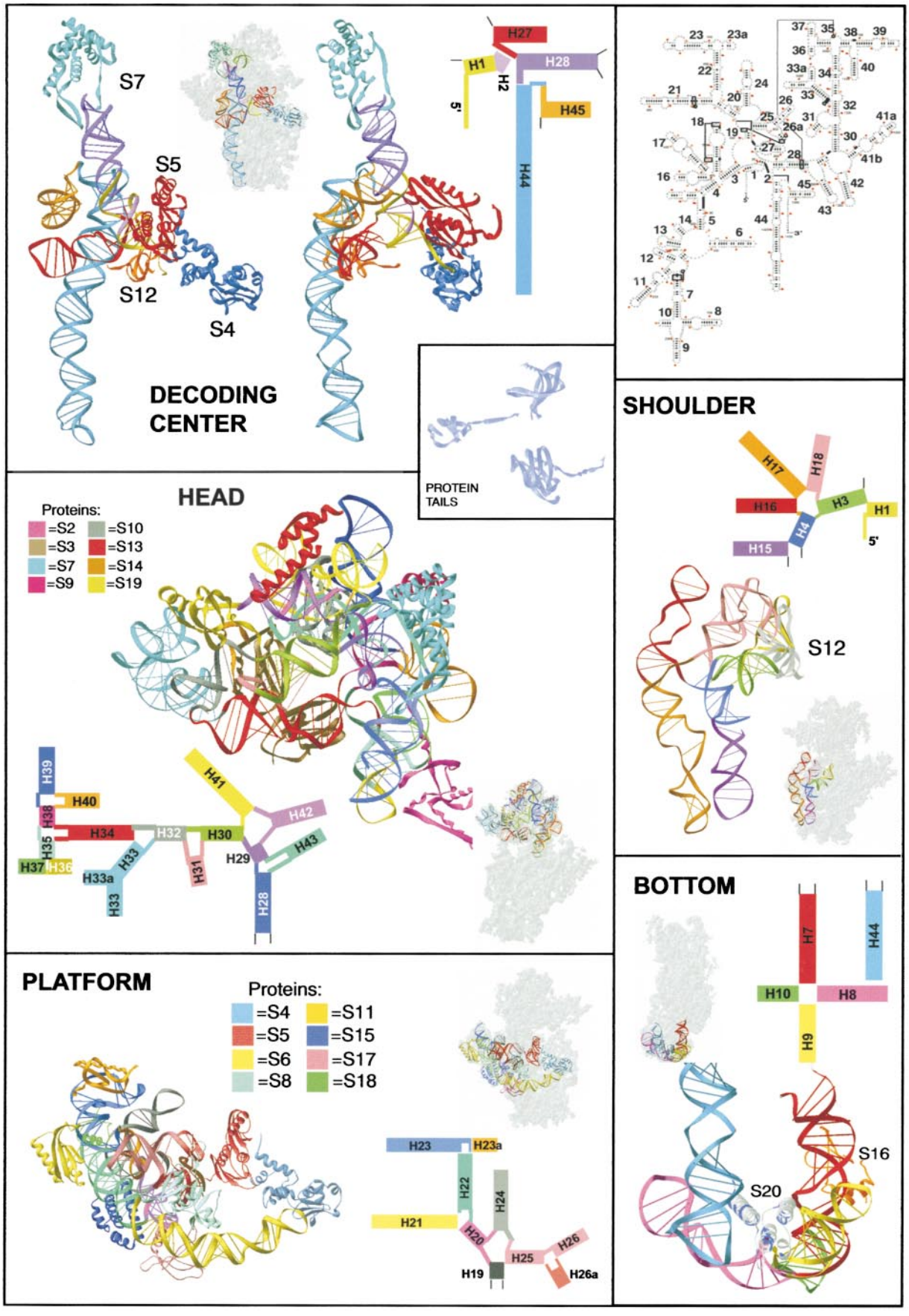
S7
S5
S12
S4
DECODING CENTER
H27
H28
H1
H2
5'
H45
H44
PROTEIN TAILS
SHOULDER
H17
H18
H16
H3
H1
H4
H15
5'
S12
HEAD
Proteins:
=S2
=S3
=S7
=S9
=S10
=S13
=S14
=S19
H39
H40
H38
H34
H32
H30
H41
H42
H35
H33
H31
H29
H43
H37
H36
H33a
H33
H28
BOTTOM
H7
H44
H10
H8
H9
S16
S20
PLATFORM
Proteins:
=S4
=S5
=S6
=S8
=S11
=S15
=S17
=S18
H23
H23a
H22
H24
H21
H20
H25
H26
H19
H26a

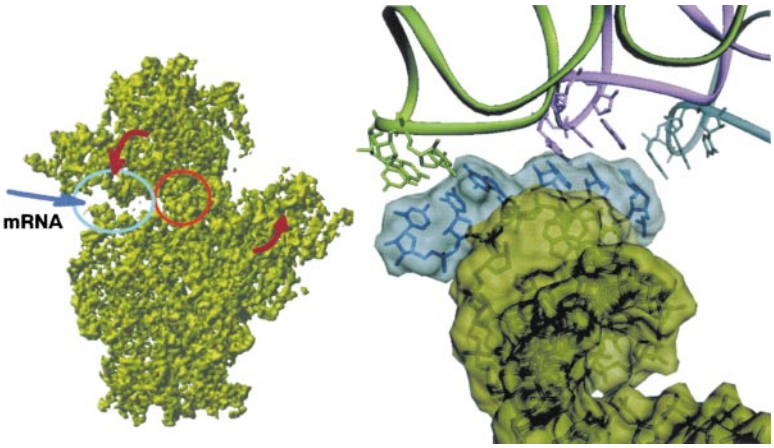

Figure 3. The Presumed mRNA Path

(Left) A surface representation of the subunit, viewed from the side of the 50S subunit. The latch is circled in cyan and the decoding center in red. The mRNA would enter the path in the approximate direction shown by the dark-blue arrow, pass through the aperture defined by the latch, and along the channel in the near face of the subunit. The brown curved arrows show the suggested global cooperative movements of the platform and the head, which facilitate the mRNA entrance, progression, and exit.

(Right) Enlarged image of the decoding center region, showing the positions of tRNA anticodon stem loops and mRNA codons, using the superposition of tRNA and mRNA from the model of Cate et al., 1999, as described in the text. The uppermost bulge of H44 is shown in olive, two codons of mRNA in blue, and the anticodon bases of the tRNA molecules in green (A site), magenta (P site) and gray (E site). The right side of the figure was made with DINO (Philippsen, 2000). The contour level is 1.1 standard deviations.

decoding center dictates formation of two successive kinks along the mRNA, allowing two tRNA molecules to be bound simultaneously and to be translocated with the mRNA chain, thus guaranteeing processivity.

Inspection of the P and E sites revealed a noteworthy example of protein-RNA mimicry. The P site tRNA interacts with helix H30, and a similar contour is contributed by protein S7 for its interaction with the E site tRNA. If the primitive ribosome contained only RNA, and the biosynthetic process required only two tRNA molecules, protein S7 may have evolved as a refinement to define the third tRNA position more precisely and to assist in the post translocational ejection of the E site tRNA.

A Latch at the Entrance of the mRNA Channel

The positions of tRNA and messenger-RNA, as determined by the superposition described above, show that mRNA must enter the channel through a pore created by a noncovalent connection between the head and body (Figure 3). To form this contact, H33/H34 project from the rim of the nose, and H16/H18 project from the shoulder, in accord with results from hydroxyl-radical cleavage experiments (Newcomb and Noller, 1999). This interaction is not seen in structures of nonactivated small subunits determined by cryo-EM (Gabashvili et al., 1999a; Harms et al., 1999) or X-ray crystallography (Clemons et al., 1999), but it is present in functional complexes of 70S ribosomes analyzed by either method (Stark et al., 1997, 2000; Cate et al., 1999; Frank and Agrawal, 2000). Closure of this "latch" is clearly due to the stabilization of the active conformation of the small subunit in our crystals. Comparisons between the present and previously determined 30S structures suggest that latch closure results from an intricate network of conformational rearrangements, involving H27, H28, and H34. These observations are in excellent agreement with the findings that opening and closing of the mRNA channel relate to the base-pairing states of the accuracy switch (Lodmell and Dahlberg, 1997; Gabashvili et al., 1999b), which depends in turn on the activation state of the ribosome (Frank and Agrawal, 2000). They are also in remarkable accord with recent targeting experiments in which the region participating in the formation of the latch was protected in activated particles and exposed in nonactivated subunits (Muth et al., 2000), suggesting that changes in the latch elements are linked to rearrangements of H34 (Stark et al., 2000) and may explain frame-shifting caused by pseudoknots in the mRNA (Kim et al., 1999). We propose that closing of the latch provides a geometry that guarantees processivity

Figure 2. Selected Structural Elements within the Small Ribosomal Subunit

Each element is shown as ribbon representations of the RNA segments and the proteins that contribute to it, together with the superposition of the element on the outline of the small subunit (gray). For each region the RNA secondary-structural elements are included, color coded to match.

The decoding center: The view on the left corresponds to rotating the object in Figure 1 by about 45° around the vertical axis (counterclockwise when seen from above), so that the platform moves toward the viewer and the nose moves away. In this view, mRNA would enter from the right rear and exit from the left front. The view on the right is roughly perpendicular to the right one.

The head: The view is about 180° from Figure 1, that is, from the side of the 50S subunit in an assembled ribosome. Note, for example, that the nose now points to the left.

The shoulder is viewed from the 50S subunit side, as shown in (B).

The bottom of the particle is seen at about 90° to the viewpoint of Fig. 1, as if from the left. That is, in an assembled ribosome, the 50S subunit would be on the left in this figure and the solvent on the right.

The platform is viewed from the solvent side, as in Figure 1. Helices H21–23 form the framework of the platform, on the solvent-facing side of the body.

Insets: (Top right) The secondary-structure diagram of the 16S RNA from *T. thermophilus* (Gutell et al., 1999), with helix numbering according to Mueller and Brimacombe, 1997.

(Middle) Within the "decoding center": the folds of proteins S5, S12, and S17 (counterclockwise, starting on top), as examples for long protruding arms.

and ensures maximum fidelity. If conformational changes in the platform and head drive translocation of mRNA-tRNA complexes, then the latch may provide directionality and prevent dissociation.

The Body

The body of the 30S subunit has a relatively compact lower part ("foot") and a wider and more flexible upper region, comprising the platform, the shoulder, and the decoding-center cleft. The foot appears to serve as an anchor to control the inclination and orientation of the main features in the intersubunit interface and in the decoding center. It contains H6-H11 and protein S20 (Figure 2). H7 runs longitudinally, parallel to H44, and branches into H8, which defines the lower boundary of the particle. H9 has extensive groove–groove contacts with H7, with its tetraloop facing outward. H7 connects with H11, which is sandwiched between H7 and H44. Helices H6–H11 and the distal end of H44 are clamped together by a highly α-helical protein, identified as S20, based on immunoelectron microscopy (Schwedler et al., 1993) and directed hydroxyl radical probing (Culver and Noller, 1998). Its sequence (to be published) shows periodically distributed lysines and arginines that form a positively charged surface to contact the sugar-phosphate backbone of the RNA. These characteristics suggest that S20 recognizes RNA structure rather than sequence, and indeed, neither the distal end of H44 nor the segment H8-H9 has a highly conserved nucleotide sequence. Despite its remote location, S20 contributes significantly to the decoding process: mutants lacking S20 exhibit misreading, temperature sensitivity, reduced capacity for intersubunit association, and impaired P site codon–anticodon interaction (Gotz et al., 1990; Ryden-Aulin et al., 1993). S20 must therefore function in part by maintaining the correct orientation of H44.

The effects of mutations in S20 demonstrate an important consequence of the striking architecture of the body. In this construction three major longitudinal elements, H44, H16/H17, and H7, act as structural pillars that extend for over 110 Å. They can therefore not only stabilize the body but also transmit conformational changes and displacements over a very long distance.

The platform (Figure 2) contributes to P site tRNA binding and is known to shift when subunits associate (Gabashvili et al., 1999b). It contains H20–H24 and proteins S6, S8, S11, S15, and S18 (Figure 2). Its central substructure, containing all proteins mentioned above apart from S11, has been studied at high resolution (Agalarov et al., 2000; Nikulin et al., 2000) and part of it has been assigned in crystallographic studies of the entire subunit at low resolution (Clemons et al., 1999). In essence, all four independently determined structures are closely related. However, we observed differences in the relative locations of some of the platform's components, when comparing the structures of our activated particle and of the nonactivated one (Clemons et al., 1999). The coaxial stack, H23 and H22, define one arm of the broad, L-shaped domain, and H21, which projects toward the shoulder, defines the other. Groove-to-groove contacts between H23 and H24 anchor the base of the platform; H25 and H26, mutually perpendicular, form a binding surface for S8. Contacts between H22 and H25 further tighten the core of the structure. The platform and the shoulder are connected by a protein-rich belt, which contains S4, S5, and S8 (Figure 2).

The shoulder contains two major, longitudinal rods, made of H15/H18 and H16/H17 (Figure 2). Their side-by-side interactions appear to form the backbone of the entire body. The packing of the mutually perpendicular H3 and H4 creates a highly compact fold in the five-way junction, H3/H4/H16/H17/H18, which is connected to the central pseudoknot through H3. The loops of H16 and H18 form one side of the latch, as described above.

The putative path taken by the messenger is located in this region. The components likely to interact with mRNA as it threads its way from the latch into the channel include the loop of H18 and proteins S3, S4, S5, and S12. S4, S5, and S12 (Baranov et al., 1999) probably assist the directionality of the decoding process and the accuracy in translation, as it has been observed that *ram* (ribosomal ambiguity) mutations in S4 and S5 cause misreading and the restrictive mutations in S12 enhance the fidelity (van Acken, 1975; Wittmann-Liebold and Greuer, 1978; Alksne et al., 1993). The anti-Shine-Dalgarno sequence, which is located at the 3′ end of the 16S RNA hybridizes with the incoming 5′ end of the mRNA. By use of an mRNA analog (a cDNA oligomer of 22 nucleotides) to which heavy atom markers had been bound prior to hybridization, the 3′ end of the 16S RNA could be located near H45 on the upper side of the platform, in the vicinity of S11 and the binding site of initiation factor IF3 (Tocilj et al., 1999; Auerbach et al., 2000; Bashan et al., 2000; further details to be published).

The Head and Neck

The head (Figure 2) contains most of the 3′ region of the 16S RNA (but not, of course, the last two helices, H44 and H45). It interacts with mRNA, elongation factor G, tRNA, and several antibiotics (Dontsova et al., 1992; Wilson and Noller, 1998; Stark et al., 2000). The proteins of the head appear to help stabilize its fold, which contains short helices and several multihelix junctions with complicated architecture. The head proteins fall mainly, but not exclusively, into two groups, on opposite sides of the domain, as suggested by early immunoelectron microscopy (Oakes et al., 1986; Stöffler and Stöffler-Meilicke, 1986). The crest of the head contains H41 and H42; the nose includes H33 and H33a; the side opposite the nose contains the stacked helices H35/H36/H38/H39. Helices H29, H30, and H32 wrap around the head and form a link to it. This unusual RNA arrangement creates an oval-shaped protein pocket. The three-way junction loop connecting H28, H29, and H43 is organized as a highly conserved, modular RNA motif (Leontis and Westhof, 1998), with similarity to loop E (Szewczak et al., 1993). This junction loop contributes to the P site for tRNA (Leontis and Westhof, 1998). Protein S7, which has been specifically crosslinked to tRNA and mRNA analogs (Dontsova et al., 1991), binds to this loop. In our model, S7 lies closer to the E site tRNA than to the P site tRNA, but its effects on stability of the fold of the 16S RNA could propagate to the entire decoding center.

H28 is the only covalent connection from the body to the head. The base-pair mismatches within it cause some structural deviations from strict A-form geometry; it is possible that these deviations are related to the postulated role of the neck as a hinge for global head motions. Variability in the shape of the head, as seen by cryo-EM (Frank et al., 1995; Stark et al., 1995; Gabashvili et al., 1999a; Harms et al., 1999) and by

X-ray crystallography (Clemons et al., 1999), shows that adjustments and conformational changes may occur within the domain, in addition to the suggested hinge motions about the neck. Conformational changes of either type may take place even within crystals, and the head may be stabilized by association with the large subunit or by nonribosomal elements, such as the W clusters in our crystals (Tocilj et al., 1999). Indeed, the apparent variability in the orientation of the head is likely to be coupled to the movement of the platform, which is known to shift upward upon subunit interaction, IF3 binding or heat activation (Gabashvili et al., 1999b, 2000). Global shifts of around 5–6 Å of the platform were also observed by superposition of the coordinates of the penultimate helix as determined for the nonactivated small subunit at 5.5 Å (Clemons et al., 1999 and PDB IQD7) on the structure of the functionally activated particle presented here.

Conclusions

The picture of the ribosomal small subunit that emerges from our analysis is one of a precisely engineered machine, with shifts coupled over long as well as short distances to create a defined sequence of events at the decoding center. Thus, mutational changes at the foot of the subunit can affect the accuracy of translation, because long helices link the foot with the center of the subunit, and motions of the head may open and close the mRNA latch. The head and platform motions may be coupled to the state of the switch helix, H27. The decoding center itself is formed exclusively of RNA, and even the closest proteins, S12 and S7, seem to serve ancillary functions such as stabilizing required conformation and assisting the translocation. The kinks in mRNA are enforced by the shape of the decoding site, and the positions of the anticodons of A and P site tRNAs are determined by cavities bounded by polynucleotide. A more extensive description of the dynamics of mRNA association and translocation will clearly require many additional structures, among them of antibiotics-bound particles, such as edeine. The present results provide a structural framework for better understanding the mechanisms associated with the decoding of the genetic information. They make the first complete bridge from the language of gross anatomy to the language of chemistry at close to atomic resolution.

Experimental Procedures

Crystals

Crystals in space group P41212 (a = b = 406.3 Å; c = 173.1 Å), were grown from heat-activated (Zamir et al., 1971) 30S subunit from T. *thermophilus,* as described in (Tocilj et al., 1999). Postcrystallization heat activation, followed by stabilization by $(K_6(P_2W_{18})O_{62})14H_2O$ (called here W18), was performed to increase the homogeneity of the activated form within the crystals, yielding a dramatic increase in the resolution. The functionally active conformation of the 30S subunits within these crystals (called here Wative) was confirmed since they were found to be isomorphous with crystals containing substrate analogs, the 5′ end of mRNA (Tocilj et al., 1999; Auerbach et al., 2000) or IF3, one of the factors that together with 30S and mRNA participates in the ribosomal initiation complex. Cocrystals of 30S with either the initiation factor IF3 or the antibiotic edeine were obtained under the same conditions. When treated by W18, they yielded diffraction of comparable resolution (3.3–3.6 Å).

Heavy-atom derivatives were prepared as described previously (Tocilj et al., 1999). The crystals contain a single 30S particle and seven W18 clusters in an asymmetric unit. The clusters stabilize and rigidify the particle (Tocilj et al., 1999). X-ray diffraction data were collected at 95K, using bright synchrotron radiation. The data were recorded on image-plate (MAR 345) or CCD (Mar, Quantum 4, or APS2) and processed with DENZO (Otwinowski and Minor, 1997). They were reduced either with SCALEPACK (Otwinowski and Minor, 1997) or with the CCP4 package (Bailey, 1994).

MIRAS Phasing

MIRAS phasing was carried out as summarized in Table 1. The W18 sites were obtained from difference Patterson and residual maps. Minor sites and sites of the smaller heavy-atom compounds were obtained form difference Fourier and residual maps. Phase refinement was performed using SHARP (de la Fortelle and Bricogne, 1997), by sequential addition of the derivatives after prerefinement. Individual W atoms of the well-ordered W18 clusters were used for phasing beyond 4.5 Å; otherwise, the tungsten clusters were represented by their spherically averaged form-factor.

Density Modification

Density modification was carried out using SOLOMON (Abrahams and Leslie, 1996). To remove potential bias of W18, the density modification procedure was altered to include gradually the low-resolution terms.

Model

The model was built using the sequence of the 16S RNA and the proteins from *T. thermophilus* (except for protein S16, for which we exploited the sequence of *Bacillus subtilis* since that of *T. thermophilus* was not available). The program O (Jones and Kjeldgaard, 1997) was used for map interpretation. Initially the map was interpreted at 3.8 Å. At that stage the map was sufficiently clear that the backbone phosphates could be positioned unambiguously for most of the RNA chain. Density for the bases was present, but individual bases were hardly separated. The RNA chain was traced by following features in the map, while maintaining acceptable bond lengths and angles. Subsequently we consulted the primary sequence and the secondary-structure diagrams of the 16S RNA (Gutell et al., 1999) to confirm our interpretation. In most cases, no significant discrepancies were detected. The few disagreements are associated mainly with multiple junctions. One example is the three-way junction of H28/H29/H43, which does not show the triplet formation but instead contains an E loop motif, as suggested by (Leontis and Westhof, 1998). Where coordinates for individual proteins were available, they were introduced as rigid bodies, and rebuilt as needed. We also consulted the structures of the RNA-protein complexes that became available after our 3.8 Å map was traced. The spatial arrangement of the rRNA chains was found to be in reasonable agreement with most of the independently derived biochemical and biophysical data.

The current 3.3 Å map shows a large number of well-resolved individual bases and protein side chains (Figure 1). The folds of the proteins that had not been determined by NMR or X-ray crystallography could be assigned directly from the map. We also could trace most of the previously undetermined parts of those proteins that have been analyzed as isolated entities by crystallography or NMR.

An example for our assignment strategy at its initial stage is given below. Apart from S7 and S19, the structures of the head proteins have not been determined independently, but density for the majority was readily detected even in our 3.8 Å map. The α-helical region above S7 was assigned to S9, exploiting crosslinking data (Baranov et al., 1999). S13, containing three parallel α helices, was located at the crest of the head in the vicinity of S19. This assignment relied on the pairing of S13 and S19 (Pohl and Wittmann-Liebold, 1988), on immuno-EM results (Montesano-Roditis et al., 1993), and on the position of a heavy-atom marker bound to an exposed cysteine of S13, prior to the crystallization (Weinstein et al., 1999). The map shows features of an S6 motif near H39; as S10 cross links to RNA components of this region and as its sequence predicts an S6-like structure, we assigned S10 to this density. S2 was identified close to H35-H37, in accord with biochemical data (Powers et al., 1988). Once the resolution improved, several regions became clearer and adjustments could be made.

Refinement with CNS (Brünger et al., 1998) and REFMAC (Murshudov et al., 1999) are in progress. An initial rigid-body refinement with bulk solvent correction yielded R_{free} of 30.5%. The correctness of the fit was assessed by using OMIT procedures, inspecting $2F_o$-F_c sigma$_a$ weighted map (Bailey, 1994).

Acknowledgments

Raz Zarivach contributed significantly to the tracing, and Joerg Harms to the assignments. We thank S. Harrison and W. Traub for critical review of the manuscript, M. Wilchek for indispensable advice, M. Pope for heavy-atom compounds, R. Brimacombe and H. Stark for fruitful discussions. We thank R. Albrecht, T. Auerbach, H. Avila, W.S. Bennett, H. Burmeister, D. Choli, C. Glotz, H.A.S. Hansen, R. Kafri, K. Knaack, M. Laschever, S. Meier, J. Muessig, M. Pioletti, M. Peretz, C. Radzwill, I. Sagi, B. Schmidt, A. Vieweger, and S. Weinstein for contributing to different stages of these studies. These studies could not be performed without the cooperation of the staff of the synchrotron radiation facilities at EMBL & MPG beam lines at DESY; ID2 and ID14/2 and 4 at EMBL and ESRF; ID19/APS/ANL and F1/CHESS. Support was provided by the Max-Planck Society, the US National Institutes of Health (GM34360), the German Ministry for Science and Technology (Bundesministerium für Bildung, Wissenschaft, Forschung und Technologie Grant 05-641EA), and the Kimmelman Center for Macromolecular Assembly at the Weizmann Institute. A. Y. holds the Martin S. Kimmel Professorial Chair.

Received June 23, 2000; revised July 31, 2000.

References

Abrahams, J.P., and Leslie, A.G.W. (1996). Methods used in the structure determination of bovine mitochondrial F-1 ATPase. Acta Crystallogr. Sect. D Biol. Crystallogr. *52*, 30–42.

Agalarov, S.C., Sridhar Prasad, G., Funke, P.M., Stout, C.D., and Williamson, J.R. (2000). Structure of the S15, S6, S18-rRNA complex: assembly of the 30S ribosome central domain. Science *288*, 107–113.

Alksne, L.E., Anthony, R.A., Liebman, S.W., and Warner, J.R. (1993). An accuracy center in the ribosome conserved over 2 billion years. Proc. Natl. Acad. Sci. USA *90*, 9538–9541.

Arad, T., Piefke, J., Weinstein, S., Gewitz, H.S., Yonath, A., and Wittmann, H.G. (1987). Three-dimensional image reconstruction from ordered arrays of 70S ribosomes. Biochimie *69*, 1001–1006.

Auerbach, T., Pioletti, M., Avila, H., Anagnostopoulos, K., Weinstein, S., Franceschi, F., and Yonath, A. (2000). Genetic and biochemical manipulations of the small ribosomal subunit from *Thermus thermophilus* HB8. J. Biomol. Struct. Dyn. *17*, 617–628.

Bailey, S. (1994). The Ccp4 suite—programs for protein crystallography. Acta Crystallogr. Sect. D Biol. Crystallogr. *50*, 760–763.

Ban, N., Nissen, P., Hansen, J., Capel, M., Moore, P.B., and Steitz, T.A. (1999). Placement of protein and RNA structures into a 5 Å-resolution map of the 50S ribosomal subunit. Nature *400*, 841–847.

Baranov, P.V., Kubarenko, A.V., Gurvich, O.L., Shamolina, T.A., and Brimacombe, R. (1999). The database of ribosomal cross-links: an update. Nucleic Acids Res. *27*, 184–185.

Bashan, A., Pioletti, M., Bartels, H., Janell, D., Schlünzen, F., Glühmann, M., Levin, I., Harms, J., Hansen, H.A.S., Tocilj, A., et al. (2000). Identification of selected ribosomal components in crystallographic maps of prokaryotic ribosomal subunits at medium resolution. In The Ribosome: Structure, Function, Antibiotics and Cellular Interactions, R. Garrett, S. Douthwaite, A. Liljas, A. Matheson, P. Moore, and H. Noller, eds. (Washington D.C.: ASM Press), pp. 21–33.

Brünger, A.T., Adams, P.D., Clore, G.M., DeLano, W.L., Gros, P., Grosse-Kunstleve, R.W., Jiang, J.S., Kuszewski, J., Nilges, M., Pannu, N.S., Read, R.J., Rice, L.M., Simonson, T., and Warren, G.L. (1998). Crystallography & NMR system: a new software suite for macromolecular structure determination. Acta Crystallogr. Sect. D Biol. Crystallogr. *54*, 905–921.

Bullard, J.M., van Waes, M.A., Bucklin, D.J., Rice, M.J., and Hill, W.E. (1998). Regions of 16S ribosomal RNA proximal to transfer RNA bound at the P-site of *Escherichia coli* ribosomes. Biochemistry *37*, 1350–1356.

Carson, M. (1997). Ribbons. Methods Enzymol. *277*, 493–505.

Cate, J.H., Yusupov, M.M., Yusupova, G.Z., Earnest, T.N., and Noller, H.F. (1999). X-ray crystal structures of 70S ribosome functional complexes. Science *285*, 2095–2104.

Choli, T., Franceschi, F., Yonath, A., and Wittmann-Liebold, B. (1993). Isolation and characterization of a new ribosomal protein from the thermophilic eubacteria, *Thermus thermophilus*, *Thermus aquaticus* and *Thermus flavus*. Biol. Chem. Hoppe-Seyler *346*, 377–383.

Clemons, W.M., Jr., May, J.L., Wimberly, B.T., McCutcheon, J.P., Capel, M.S., and Ramakrishnan, V. (1999). Structure of a bacterial 30S ribosomal subunit at 5.5 A resolution. Nature *400*, 833–840.

Conn, G.L., Draper, D.E., Lattman, E.E., and Gittis, A.G. (1999). Crystal structure of a conserved ribosomal protein-RNA complex. Science *284*, 1171–1174.

Culver, G.M., and Noller, H.F. (1998). Directed hydroxyl radical probing of 16S ribosomal RNA in ribosomes containing Fe(II) tethered to ribosomal protein S20. RNA *4*, 1471–1480.

de la Fortelle, E., and Bricogne, G. (1997). Maximum-likelihood heavy-atom parameter refinement for multiple isomorphous replacement and multiwavelength anomalous diffraction methods. Macromol. Crystallogr. A *276*, 472–494.

Dontsova, O., Kopylov, A., and Brimacombe, R. (1991). The location of messenger-RNA in the ribosomal 30S initiation complex—site-directed cross-linking of messenger-RNA analogs carrying several photo-reactive labels simultaneously on either side of the AUG start codon. EMBO J. *10*, 2613–2620.

Dontsova, O., Dokudovskaya, S., Kopylov, A., Bogdanov, A., Rinke-Appel, J., Junke, N., and Brimacombe, R. (1992). Three widely separated positions in the 16S-RNA lie in or close to the ribosomal decoding region—a site-directed cross-linking study with messenger-RNA analogs. EMBO J. *11*, 3105–3116.

Fourmy, D., Yoshizawa, S., and Puglisi, J.D. (1998). Paromomycin binding induces a local conformational change in the A-site of 16 S rRNA. J. Mol. Biol. *277*, 333–345.

Frank, J., and Agrawal, R.K. (2000). A ratchet-like inter-subunit reorganization of the ribosome during translocation. Nature *406*, 318–322.

Frank, J., Zhu, J., Penczek, P., Li, Y.H., Srivastava, S., Verschoor, A., Radermacher, M., Grassucci, R., Lata, R.K., and Agrawal, R.K. (1995). A model of protein synthesis based on cryo-electron microscopy of the *E. coli* ribosome. Nature *376*, 441–444.

Gabashvili, I.S., Agrawal, R.K., Grassucci, R., and Frank, J. (1999a). Structure and structural variations of the *Escherichia coli* 30S ribosomal subunit as revealed by three-dimensional cryo-electron microscopy. J. Mol. Biol. *286*, 1285–1291.

Gabashvili, I.S., Agrawal, R.K., Grassucci, R., Squires, C.L., Dahlberg, A.E., and Frank, J. (1999b). Major rearrangements in the 70S ribosomal 3D structure caused by a conformational switch in 16S ribosomal RNA. EMBO J. *18*, 6501–6507.

Gabashvili, I.S., Agrawal, R.K., Spahn, C.M., Grassucci, R.A., Svergun, D.I., Frank, J., and Penczek, P. (2000). Solution structure of the *E. coli* 70S ribosome at 11.5 A resolution. Cell *100*, 537–549.

Gotz, F., Dabbs, E.R., and Gualerzi, C.O. (1990). *Escherichia coli* 30S mutants lacking protein S20 are defective in translation initiation. Biochim. Biophys. Acta *1050*, 93–97.

Green, R., and Noller, H.F. (1997). Ribosomes and translation. Annu. Rev. Biochem. *66*, 679–716.

Gutell, R.R., Subashchandran, S., Schnare, M., Du, Y., Lin, N., Madabusi, L., Muller, K., Pande, N., Yu, N., Shang, Z., Date, S., Konings, D., Schweiker, V., Weiser, B., and Cannone, J.J. (1999). Comparative sequence analysis and the prediction of RNA structure, and the Web. http://www.rna.icmb.utexas.edu/.

Harms, J., Tocilj, A., Levin, I., Agmon, I., Stark, H., Kölln, I., van Heel, M., Cuff, M., Schlünzen, F., Bashan, A., Franceschi, F., and Yonath, A. (1999). Elucidating the medium-resolution structure of ribosomal particles: an interplay between electron cryo-microscopy and X-ray crystallography. Structure Fold. Des. *7*, 931–941.

Helgstrand, M., Rak, A.V., Allard, P., Davydova, N., Garber, M.B., and Hard, T. (1999). Solution structure of the ribosomal protein S19 from *Thermus thermophilus*. J. Mol. Biol. *292*, 1071–1081.

Jones, T.A., and Kjeldgaard, M. (1997). Electron-density map interpretation. Methods Enzymol. *277*, 173–208.

Kim, Y.G., Su, L., Maas, S., O'Neill, A., and Rich, A. (1999). Specific mutations in a viral RNA pseudoknot drastically change ribosomal frameshifting efficiency. Proc. Natl. Acad. Sci. USA *96*, 14234–14239.

Leontis, N.B., and Westhof, E. (1998). A common motif organizes the structure of multi-helix loops in 16 S and 23 S ribosomal RNAs. J. Mol. Biol. *283*, 571–583.

Lodmell, J.S., and Dahlberg, A.E. (1997). A conformational switch in *Escherichia coli* 16S ribosomal RNA during decoding of messenger RNA. Science *277*, 1262–1267.

Luger, K., Mader, A.W., Richmond, R.K., Sargent, D.F., and Richmond, T.J. (1997). Crystal structure of the nucleosome core particle at 2.8 Å resolution. Nature *389*, 251–260.

Montesano-Roditis, L., McWilliams, R., Glitz, D.G., Olah, T.V., Perrault, A.R., and Cooperman, B.S. (1993). Placement of dinitrophenyl-modified ribosomal proteins in totally reconstituted *Escherichia coli* 30S subunits: Localization of proteins S6, S13, S16, and S18 by immune electron microscopy. J. Biol. Chem. *268*, 19701–19709.

Mueller, F., and Brimacombe, R. (1997). A new model for the three-dimensional folding of *Escherichia coli* 16S ribosomal RNA. I. Fitting the RNA to a 3D electron microscopic map at 20 Å. J. Mol. Biol. *271*, 524–544.

Mueller, F., Stark, H., vanHeel, M., Rinke-Appel, J., and Brimacombe, R. (1997). A new model for the three-dimensional folding of *Escherichia coli* 16 S ribosomal RNA. III. The topography of the functional centre. J. Mol. Biol. *271*, 566–587.

Murshudov, G.N., Levedev, A., Vagin, A.A., Wilson, K.S., and Dodson, E.J. (1999). Efficient anisotropic refinement of macromolecular structures using FFT. Acta Crystallogr. Sect. D Biol. Crystallogr. *55*, 247–255.

Murzina, N.V., Vorozheykina, D.P., and Matvienko, N.I. (1988). Nucleotide sequence of *Thermus thermophilus* HB8 gene coding 16S ribosomal-RNA. Nucleic Acids Res. *16*, 8172–8172.

Muth, G.W., Hennelly, S.P., and Hill, W.E. (2000). Using a targeted chemical nuclease to elucidate conformational changes in the *E. coli* 30S ribosomal subunit. Biochemistry *34*, 4068–4074.

Newcomb, L.F., and Noller, H.F. (1999). Directed hydroxyl radical probing of 16S rRNA in the ribosome: spatial proximity of RNA elements of the 3′ and 5′ domains. RNA *5*, 849–855.

Nikulin, A., Serganov, A., Ennifar, E., Tishchenko, S., Nevskaya, N., Shepard, W., Portier, C., Garber, M., Ehresmann, B., Ehresmann, C., Nikonov, S., and Dumas, P. (2000). Crystal structure of the S15-rRNA complex. Nat. Struct. Biol. *7*, 273–277.

Oakes, M., Henderson, E., Scheinman, A., Clark, M., and Lake, J.A. (1986). Ribosome structure, function and evolution: mapping ribosomal RNA, proteins, and functional sites in three dimensions. In Structure, Function and Genetics of Ribosomes, B. Hardesty and G. Kramer, eds. (Berlin: Springer Verlag), pp. 47–67.

Otwinowski, Z., and Minor, W. (1997). Processing of X-ray diffraction data collected in oscillation mode. Macromol. Crystallogr. A *276*, 307–326.

Philippsen, A. (2000). DINO: Visualizing Structural Biology. http://www.bioz.unibas.ch/∼xray/dino.

Pohl, T., and Wittmann-Liebold, B. (1988). Identification of a cross-link in the *Escherichia coli* ribosomal protein pair S13–S19 at the amino acid level. J. Biol. Chem. *263*, 4293–4301.

Poot, R.A., van den Worm, S.H., Pleij, C.W.A., and van Duin, J. (1998). Base complementarity in helix 2 of the central pseudoknot in 16S rRNA is essential for ribosome functioning. Nucleic Acids Res. *26*, 549–553.

Powers, T., and Noller, H.F. (1991). A functional pseudoknot in 16S ribosomal-RNA. EMBO J. *10*, 2203–2214.

Powers, T., Stern, S., Changchien, L.M., and Noller, H.F. (1988). Probing the assembly of the 3′ major domain of 16 S rRNA interactions involving ribosomal proteins S2, S3, S10, S13 and S14. J. Mol. Biol. *201*, 697–716.

Ramakrishnan, V., and White, S.W. (1998). Ribosomal protein structures: insights into the architecture, maschinery and evolution of the ribosome. Trends Biochem. Sci. *23*, 208–212.

Ryden-Aulin, M., Shaoping, Z., Kylsten, P., and Isaksson, L.A. (1993). Ribosome activity and modification of 16S RNA are influenced by deletion of ribosomal protein S20. Mol. Microbiol. *7*, 983–992.

Schwedler, G., Albrecht-Ehrlich, R., and Rak, K.H. (1993). Immunoelectron microscopic localization of ribosomal proteins BS8, BS9, BS20, BL3 and BL21 on the surface of 30S and 50S subunits from *Bacillus stearothermophilus*. Eur. J. Biochem. *217*, 361–369.

Spickler, C., Brunelle, M.N., and Brakier-Gingras, L. (1997). Streptomycin binds to the decoding center of 16 S ribosomal RNA. J. Mol. Biol. *273*, 586–599.

Stark, H., Mueller, F., Orlova, E.V., Schatz, M., Dube, P., Erdemir, T., Zemlin, F., Brimacombe, R., and Heel, M. (1995). The 70S *Escherichia coli* ribosome at 23 Å resolution: fitting the ribosomal RNA. Structure *3*, 815–821.

Stark, H., Rodnina, M.V., Rinke-Appel, J., Brimacombe, R., Wintermeyer, W., and van Heel, M. (1997). Visualization of elongation factor Tu on the *Escherichia coli* ribosome. Nature *389*, 403–406.

Stark, H., Rodnina, M.V., Wieden, H.J., van Heel, M., and Wintermeyer, W. (2000). Large-scale movement of elongation factor G and extensive conformational change of the ribosome during translocation. Cell *100*, 301–309.

Stöffler, G., and Stöffler-Meilicke, M. (1986). Immuno electron microscopy on *Escherichia coli* ribosomes. In Structure, Function and Genetics of Ribosomes, B. Hardesty and G. Kramer, eds. (Berlin: Springer Verlag), pp. 28–46.

Szewczak, A.A., Moore, P.B., Chang, Y.L., and Wool, I.G. (1993). The conformation of the sarcin/ricin loop from 28S ribosomal RNA. Proc. Natl. Acad. Sci. USA *90*, 9581–9585.

Tocilj, A., Schlünzen, F., Janell, D., Glühmann, M., Hansen, H.A., Harms, J., Bashan, A., Bartels, H., Agmon, I., Franceschi, F., and Yonath, A. (1999). The small ribosomal subunit from *Thermus thermophilus* at 4.5 A resolution: pattern fittings and the identification of a functional site. Proc. Natl. Acad. Sci. USA *96*, 14252–14257.

Tsiboli, P., Herfurth, E., and Choli, T. (1994). Purification and characterization of the 30S ribosomal proteins from the bacterium *Thermus thermophilus*. Eur. J. Biochem. *226*, 169–177.

van Acken, U. (1975). Protein chemical studies on ribosomal proteins S4 and S12 from ram (ribosomal ambiguity) mutants of *Escherichia coli*. Mol. Gen. Genet. *140*, 61–68.

VanLoock, M.S., Easterwood, T.R., and Harvey, S.C. (1999). Major groove binding of the tRNA/mRNA complex to the 16 S ribosomal RNA decoding site. J. Mol. Biol. *285*, 2069–2078.

Weinstein, S., Jahn, W., Glotz, C., Schlünzen, F., Levin, I., Janell, D., Harms, J., Kölln, I., Hansen, H.A.S., Glühmann, M., et al. (1999). Metal compounds as tools for the construction and the interpretation of medium-resolution maps of ribosomal particles. J. Struct. Biol. *127*, 141–151.

Wilson, K.S., and Noller, H.F. (1998). Mapping the position of translational elongation factor EF-G in the ribosome by directed hydroxyl radical probing. Cell *92*, 131–139.

Wimberly, B.T., Guymon, R., McCutcheon, J.P., White, S.W., and Ramakrishnan, V. (1999). A detailed view of a ribosomal active site: the structure of the L11-RNA complex. Cell *97*, 491–502.

Wittmann-Liebold, B., and Greuer, B. (1978). The primary structure of protein S5 from the small subunit of the *Escherichia coli* ribosome. FEBS Lett. *95*, 91–98.

Zamir, A., Miskin, R., and Elson, D. (1971). Inactivation and reactivation of ribosomal subunits: amino acyl transfer RNA binding activity of the 30S subunit from *Escherichia coli*. J. Mol. Biol. *60*, 347–364.

Protein Data Bank ID Code

The coordinates reported in this paper have been deposited in the Protein Data Bank under ID code 1FKA.

Elucidating the medium-resolution structure of ribosomal particles: an interplay between electron cryo-microscopy and X-ray crystallography

Jörg Harms[1‡], Ante Tocilj[2‡], Inna Levin[2‡], Ilana Agmon[2‡], Holger Stark[3†‡], Ingo Kölln[1], Marin van Heel[3], Marianne Cuff[3], Frank Schlünzen[1], Anat Bashan[2], Francois Franceschi[4] and Ada Yonath[1,2*]

Background: Ribosomes are the universal cellular organelles that accomplish the translation of the genetic code into proteins. Electron cryo-microscopy (cryo-EM) has yielded fairly detailed three-dimensional reconstructions of ribosomes. These were used to assist in the determination of higher resolution structures by X-ray crystallography.

Results: Molecular replacement studies using cryo-EM reconstructions provided feasible packing schemes for crystals of ribosomes and their two subunits from *Thermus thermophilus*, and of the large subunits from *Haloarcula marismortui*. For the large subunits, these studies also confirmed the major heavy-atom sites obtained by single isomorphous replacement combined with anomalous diffraction (SIRAS) and by multiple isomorphous replacement combined with anomalous diffraction (MIRAS) at ~10 Å. Although adequate starting phases could not be obtained for the small subunits, the crystals of which diffract to 3.0 Å, cryo-EM reconstructions were indispensable for analyzing their 7.2 Å multiple isomorphous replacement (MIR) map. This work indicated that the conformation of the crystallized small subunits resembles that seen within the 70S ribosomes. Subsequently, crystals of particles trapped in their functionally active state were grown.

Conclusions: Single-particle cryo-EM can contribute to the progress of crystallography of non-symmetrical, large and flexible macromolecular assemblies. Besides confirming heavy-atom sites, obtained from flat or overcrowded difference Patterson maps, the cryo-EM reconstructions assisted in elucidating packing arrangements. They also provided tools for the identification of the conformation within the crystals and for the estimation of the level of inherent non-isomorphism.

Addresses: [1]Max-Planck Research Unit for Ribosomal Structure, Notke Strasse 85, 22603 Hamburg, Germany, [2]Department of Structural Biology, Weizmann Institute, 76100 Rehovot, Israel, [3]Imperial College of Science, Technology and Medicine, Department of Biochemistry, London SW7 2AY, UK and [4]Max-Planck Institute for Molecular Genetics, Ihnestrasse 73, 14195 Berlin, Germany.

[†]Present address: Marburg University, Institute for Molecular Biology & Cancer Research, Marburg, 35037, Germany.

*Corresponding author.
E-mail: YONATH@mpgars.desy.de

[‡]These authors made a major contribution to these studies.

Key words: electron cryo-microscopy, MIR phasing, MR searches, ribosomes

Received: 14 October 1998
Revisions requested: 4 December 1998
Revisions received: 3 March 1999
Accepted: 21 April 1999

Published: 15 July 1999

Structure August 1999, 7:931–941
http://biomednet.com/elecref/0969212600700931

© Elsevier Science Ltd ISSN 0969-2126

Introduction

Ribosomes, discovered in the mid-fifties, are the universal cellular organelles on which the sequential polymerization of amino acids according to the genetic code takes place. They are giant ribonucleoprotein assemblies (called 70S in bacteria), consisting of two subunits of unequal size (called 50S and 30S in bacteria) that associate upon initiation of protein biosynthesis. Extensive efforts have been made to elucidate the three-dimensional structure of the ribosome, using a large range of techniques including X-ray crystallography and advanced cryo-electron microscopy (cryo-EM).

We have grown two types of three-dimensional crystals of ribosomal particles that diffract to around 3 Å resolution: those of the large subunits from *Haloarcula marismortui*, H50S, and those of the small subunits from *Thermus thermophilus*, T30S [1,2]. Difficulties in carrying out crystallographic analysis of them reflect their unfavorable characteristics. Not only are the ribosomes of a huge size with no internal symmetry, they also exhibit internal flexibility and have a surface that is rich in readily degradable RNA and loosely attached proteins. Moreover, most of the ribosomal crystals show extreme radiation sensitivity, poor isomorphism and non-isotropic mosaicity. They yield deformed spot shapes and suffer from an increase in the unit-cell dimensions during X-ray exposure.

Electron microscopy of ribosomal particles has undergone significant developments over the past few years. The introduction of single-particle cryo-EM, in combination with powerful computational procedures such as angular reconstitution [3–6], has yielded detailed three-dimensional

images of bacterial ribosomal particles and their functional complexes [7–13]. These three-dimensional reconstructions resemble the consensus topography observed by traditional negative-staining EM and confirm the existence of internal features, mainly associated with vacant spaces such as tunnels and hollows, detected about a decade ago in reconstructions from negatively stained crystalline arrays [14–17]. They have also been interpreted along similar lines, in conjunction with biochemical findings accumulated over three decades [18,19]. Using the reconstructions obtained from negatively stained arrays we have conducted combined EM/X-ray studies at different levels [20] that clearly pointed to the need for more detailed starting models.

With the availability of cryo-EM three-dimensional reconstructions, a fruitful interface between EM imaging and X-ray crystallography became feasible. The suitability of EM information for yielding adequate X-ray phases that lead to structure determination was first shown for the tomato bushy stunt virus, a system with a high level of noncrystallographic symmetry [21]. Similar studies were performed later on other viruses [22] and smaller macromolecules [23]. In studies of complicated structures, such as the proteosome [24] and the chaperonin GroEL [25], EM was useful in confirming their internal symmetry. The overall shape of the nucleosome [26], as observed by EM, was initially combined with the known DNA periodicity. EM of muscle fibers and high-resolution structures of the muscle proteins were exploited together for the determination of the structure of the actin–myosin complex [27]. Only a few molecular replacement (MR) studies of large assemblies with no internal symmetry, such as ribosomes, however, have been reported so far [2,19,28].

We report here three approaches to MR studies of ribosomal particles from *T. thermophilus* and of H50S, the large ribosomal subunit from *H. marismortui*. We used pure MR searches and their verification by noncrystallographic information for the 70S ribosomes from *T. thermophilus*, T70S. We then employed MR combined with experimental phasing, including the confirmation of heavy-atom sites detected independently by crystallographic methods, for the 50S subunits from *T. thermophilus*, T50S, and for H50S. For the latter, the exploitation of the MR results for the estimation of the level of non-isomorphism and the suitability of the crystallographic data for efficient phasing is suggested. We employed MR as a tool for confirming independently determined packing diagrams, for better understanding of crystal selectivity and for the design of controlled conformational rearrangements within the crystals for T30S.

Results

The whole ribosome: T70S

The T70S reconstruction, performed at 24 Å resolution as for E70S (70S from *Escherichia coli*) [7,8], revealed detail including a network of tunnels through the 50S part and a large gap between the two subunits, similar to features detected earlier in reconstructions from two-dimensional arrays of 50S and 70S from *Bacillus stearothermophilus* [15,16]. T70S crystals diffract to a comparable resolution, 20–24 Å [29–31]. A complex of T70S with two molecules of PhetRNA^{Phe}, however, yielded crystals isomorphous to those of T70S but diffracting to 12–17 Å [31]; the latter were used for the MR studies.

A unique solution, with Cf (correlation coefficient, calculated using structure factors) of 72%, Ci (correlation coefficient, calculated using intensities) of 73%, agreement factor (R) of 45% and a contrast (the ratio between the correlation coefficient of the best solution and that of the following one) of 1.5, was obtained when the EM reconstruction was expanded isotropically by 2% (see Materials and methods section) and used for MR searches at 20–40 Å (Figure 1). The same solution was obtained for a large range of resolutions and radii, but with somewhat inferior scores. The map assembled according to this solution (Figure 2) shows no collisions or short contacts, and the MR packing scheme agrees with the arrangement detected in electron micrographs of positively stained thin sections of the T70S crystals.

The large ribosomal subunits: T50S and H50S

The crystals of T50S diffract nominally to 8.7 Å [32], but yield useful data to only 10–12 Å. Rotation and translation searches were performed using the 17 Å cryo-EM reconstruction of this particle, shrunk isotropically by 4% (see Materials and methods section). These searches (Figure 3) resulted in a single unique solution (Cf = 65%, Ci = 67%,

Figure 1

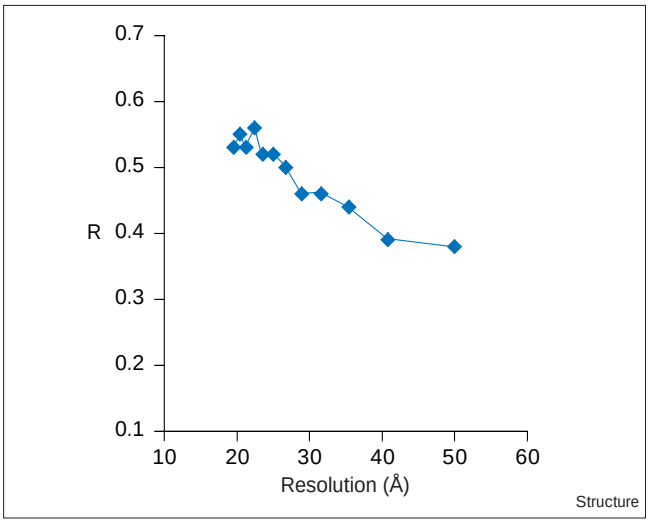

The agreement factor R(F_c/F_{obs}) of the MR result for the cryo-EM reconstruction of T70S in the crystal, as a function of resolution.

Figure 2

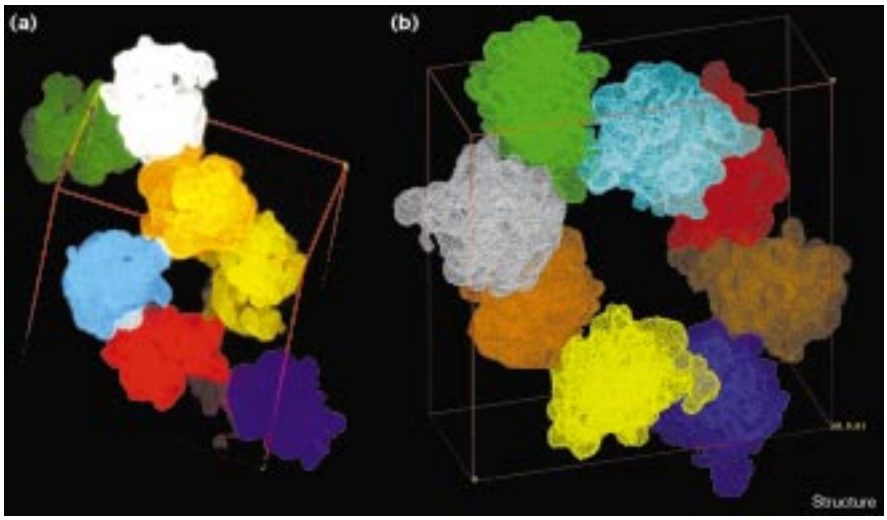

(a) The packing of the whole ribosome (T70S), assembled by positioning the 24 Å EM reconstruction in the crystallographic unit cell according to the MR search. (b) The packing of the large ribosomal subunit (T50S), assembled by positioning the 17 Å EM reconstruction in the crystallographic unit cell according to the MR results.

R = 41% and contrast(i) = 1.8) exhibiting normal interparticle contacts without overlap (Figure 2).

Crystallographic data were collected to 10 Å from native and Ta_6Br_{14}-soaked crystals of T50S. Two sites, extracted from isomorphous and anomalous difference Patterson maps, were used for initial SIRAS (single isomorphous replacement combined with anomalous diffraction). Final statistics: R_{cullis} = 0.59 (total); 0.87 (anomalous); phasing power = 1.95; figure of merit (FOM) = 0.58. These two sites were placed in the map phased according to the MR results and found to be in crystallographically sound positions [2,19]. Half a dozen sites with heights of around 4σ were detected in a difference Fourier map on the basis of the MR phases, and one corresponds to the main Ta_6Br_{14} SIRAS site. These sites might be used for extending the detail of the cryo-EM reconstruction, from its original 17 Å to the crystallographic limit of 10 Å resolution (work in progress).

Although the crystals of H50S diffract to the highest resolution obtained for ribosomal particles, 2.7 Å, they possess several undesirable properties that become less tolerable with the increase of resolution, among them a severe sensitivity to X-ray irradiation coupled with an extremely low level of isomorphism. Hence, their structure determination is performed in stages from lower to higher resolution. The shape of the particle as observed in the 12 Å MIRAS (multiple isomorphous replacement combined with anomalous diffraction) map [2], currently extended to 7.5 Å, is similar to that obtained by cryo-EM for large subunits from various bacterial sources [2,7,8,15,19,33]. It shows gross features that were identified by EM at lower resolution, such as the exit tunnel, but in more detail. It also contains elongated dense regions, interpretable as single- and double-stranded RNA chains.

The packing arrangement of these crystals is such that H50S particles form two closely packed layers, connected by a narrow contact region in the middle of the c axis (Figure 4). This contact area is surrounded by a very large continuous solvent region, reaching dimensions of more than 240 × 140 × 100 Å. The limited size of the interparticle contact region permits only a small number of interactions. This might cause the poor isomorphism, the unfavorable crystal habit (plates, made of sliding layers, reaching typically up to 0.5 mm^2 with an average thickness of a few microns in the direction of the c axis), and the variations in the c axis length (567–570 Å) as a function of irradiation [2].

The native data set used for MIRAS phasing was exploited for MR validation tests in order to minimize the probability of bias originating from the low level of isomorphism. A satisfactory packing arrangement was

Figure 3

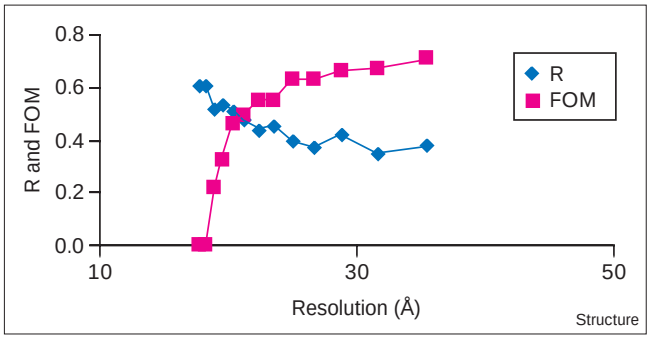

The agreement factor $R(F_c/F_{obs})$ and the figure of merit (FOM) values obtained for the MR result for the packing diagram of the crystals of T50S, as a function of resolution.

Figure 4

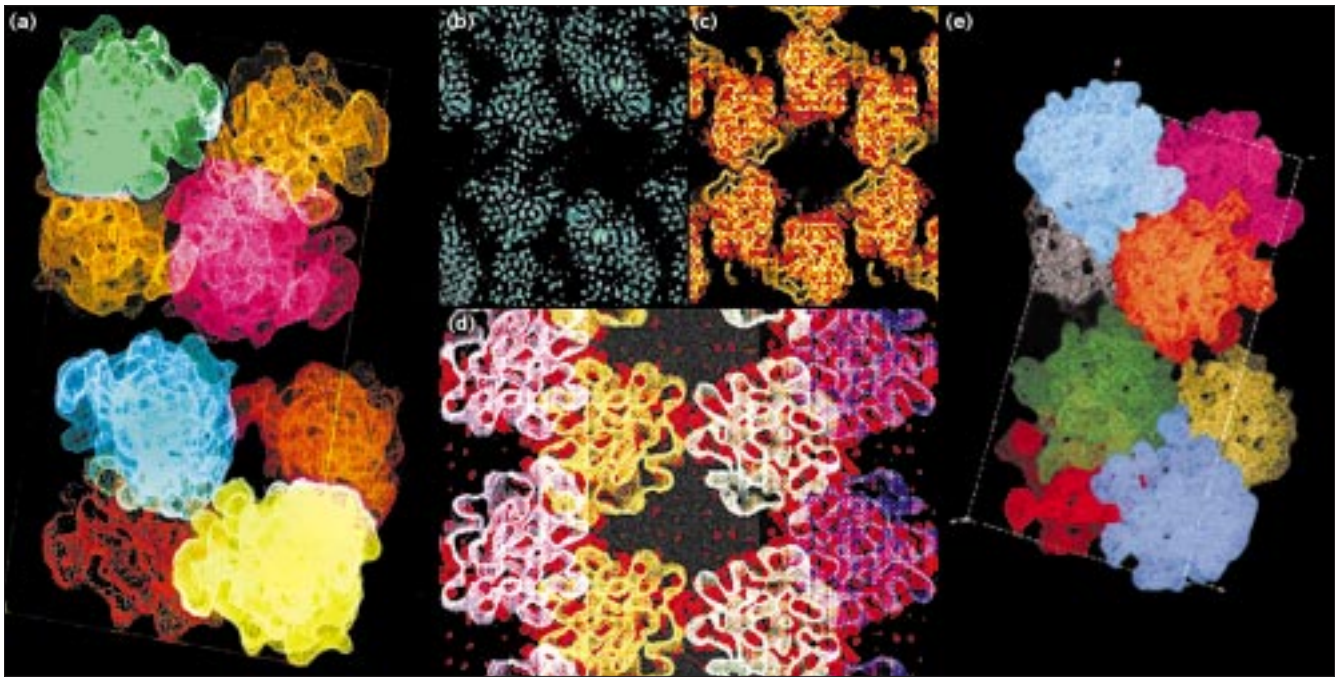

The packing arrangement of H50S crystals. **(a)** The MIRAS compatible MR packing arrangement of H50S crystals. **(b)** A slice of about 20 Å thickness of the H50S MIRAS map, showing the loose contact and the site of the main heavy atom. **(c,d)** Two slices, each of about 40 Å thickness, of the MR solution overlaid on the MIRAS map (shown in red), highlighting the main difference between the results of the two methods. **(e)** For comparison, the result of the parallel MR studies (this figure was reproduced from [28] with permission).

obtained (93% correlation, R factor 27% for 60–90 Å and 39–50% correlation with R factor 42–47% for 30–95 Å), showing the packing observed in the MIRAS map (Figure 4). For confirming the previously determined major site of Ta_6Br_{14}, the strongest H50S derivative [32], we first established that it is detectable in difference Patterson maps constructed at lower than 17 Å, the limit dictated by the cryo-EM reconstruction.

It should be mentioned that the salts required for functional activity of H50S (2.5–3 M KCl and 0.5 M NH_4Cl) hamper cryo-EM studies. The only available EM reconstruction of H50S was obtained using a solution of significantly lower salt concentration [28], close to that used at the initial step of H50S crystallization [1,34]. We used this low salt concentration to control the crystallization process because the crystallization terminated after a few hours in a shower of disordered microcrystals when the higher salt concentration necessary for activity was employed. Hence, we designed a procedure in which crystallization occurs in solutions with the minimum salt needed for the integrity of the particle (1.2–1.7 M KCl and 0.5 M NH_4Cl), at which no functional activity was detected. Once the crystals are formed they are transferred to solutions containing the salts required for functional activity [18,34], allowing X-ray measurements under these conditions.

We used the higher resolution cryo-EM reconstruction of T50S (17 Å) for MR searches of the H50S crystals because we believed that the similarity between the active conformations of 50S in the two bacteria should be a better basis for MR searches than the similarity between active and inactive conformations from the same bacterium. This assumption was confirmed in our studies as well as studies from another group using data from crystals of H50S grown under the same crystallization conditions and an EM reconstruction of the large subunit cut from that of 70S from *E. coli* [28].

Thus, it seems that the gross conformations of the large ribosomal subunits from archea and eubacteria are rather similar, and that this similarity is maintained even in slightly different environments, as long as the integrity of the particles is not harmed. The differences among the species, however, are not negligible. Indications for them were detected even at very low resolution, as seen by the decrease in the scores with progression from 60–30 Å.

Comparison of the MIRAS and the MR maps at comparable resolution (Figure 4) showed the same packing arrangements with the same positions of the centers of mass (COM) of the particles. The main differences between the MIRAS and MR maps are in the locations assigned to L1

and L7 proteins by EM. These two proteins are well resolved in the cryo-EM reconstructions, but diffuse into the solvent in the MIRAS map (Figure 4), probably because of the similarity in the electron density of the solution within the H50S crystals (3 M KCl) and that of proteins [2].

Similarities were detected between the MR packing arrangement and that revealed by neutron diffraction [35]. In addition, the MR-determined COMs of H50S as determined elsewhere at comparable resolution [28] are located at approximately the same position as in our studies, but with different orientation (Figure 4). This suggests a link between the variations in the orientations of the particles and the level of non-isomorphism. We therefore examined the MR solutions obtained for over two dozen H50S data sets of native, derivatized and chemically treated particles. We found that some of the data sets led to solutions with reasonable scores that fall into the category described above: similar COM positions, but variability in the orientations. Other data sets led to several unrelated solutions. The classification by COM provided a tool to discriminate between extreme and moderate deviations from isomorphism and assist in the selection of consistent data sets for MIR phasing. This approach might be unnecessary in standard cases, but it should be increasingly useful for studies of giant macromolecular complexes that yield overcrowded, flat and difficult to interpret difference Patterson maps.

The resolution of the crystallographic studies of H50S is currently being significantly extended, as a 5 Å anomalous data set of the Ta_6Br_{14} derivative gave difference Patterson maps that show a major site consistent with our lower resolution results [2]. Hence we have decided to delay the interpretation until a later stage.

The small ribosomal subunit: T30S

In contrast to the impressive progress in image reconstruction of 70S ribosomes and 50S subunits, until recently the small ribosomal subunit was reconstructed to only 37 Å resolution [36]. The flexibility and instability of the small subunits is easily demonstrated. Exposure of 70S ribosomes to proteolytic enzymes resulted in complete digestion of the 30S subunits and left the 50S subunits essentially intact. Furthermore, crystallization attempts with functionally active 70S ribosomes that were formed from *in vitro* associated subunits, yielded crystals of the 50S subunits and degradation of the 30S [18,37]. For our cryo-EM reconstructions, therefore, we used the preparations that yielded the best three-dimensional crystals. Nevertheless, these yielded reconstructions at only 25 Å (Figure 5), a resolution limit that is significantly poorer than that obtained for T50S, but the highest obtained from 30S to date.

The two crystal forms of T30S that we obtained are clearly non-isomorphous (R scale above 60%), even though their unit-cell parameters are virtually identical ($P4_12_12$, a = b = 405 Å, c = 176 Å). The first crystal form (called T30S-LR) was characterized about ten years ago [38], but was not extensively studied because its diffraction yielded useful data to only 12–18 Å [39]. Subtle modifications in the procedures of bacterial growth and crystal treatment recently led to a higher resolution, 3.0 Å. The current MIR 7.2 Å electron-density map of these crystals (called T30S-HR) reveals elongated dense regions similar to those detected in the nucleosome at comparable resolution levels [40] and globular or elliptic lower resolution regions, appropriate to host ribosomal proteins.

Among the main features of the 7.2 Å map are extensive pairing of the particles and an internal continuous solvent region of a fairly large size, both detected earlier by conventional negative-stain EM. The large solvent region was first observed in EM studies of positively stained thin sections of epon-embedded T30S-LR crystals (Figure 6). The pairing contacts are extremely stable and maintained even after the rest of the crystal network is destroyed. Thus, EM of dissolved T30S-HR crystals showed the majority of the particles as pairs with a typical butterfly-like shape (Figure 6), similar to the organization in the crystal (Figure 7). These two prominent features were also

Figure 5

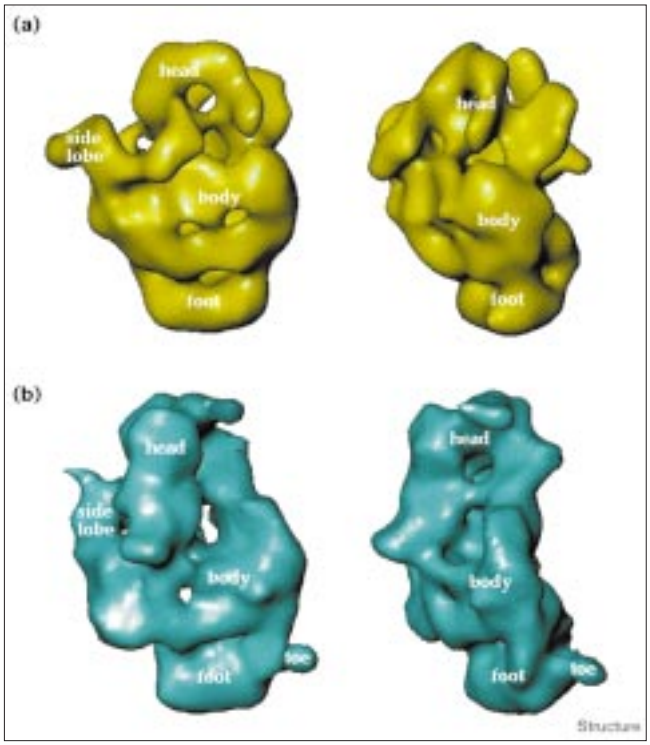

(a) Two views of the 25 Å cryo-EM reconstruction of the isolated (free) T30S. (b) The bound form of T30S (the cut model, obtained by removing the density assigned for T50S in the reconstruction of T70S), positioned in the same orientation as (a).

observed in the MR packing diagrams of T30S-LR and T30S-HR crystals, using the reconstructions of free T30S (Figure 6). Despite the difference in scores obtained from MR searches of T30S-LR (Cf = 66.0%, R = 46.4%, contrast(f) = 1.2) and of T30S-HR (Cf = 40.2%, R = 54.5%, contrast(f) = 1.1), at a first glance the two solutions show a high degree of similarity. Indeed, the COM's of the particles are almost identical but their relative orientations differ by approximately 80°. Thus, in the HR crystals the upper part of T30S (called the head, and known to be flexible) is involved in extensive contacts, whereas in the LR form it points into the solution. It is conceivable that free movement of the heads allowed by the LR packing arrangement causes the lower resolution of this crystal form. Hindrance of these movements by the crystal network might be the reason for the higher order of the T30S-HR crystals.

Attempts to fit the contour of the cryo-EM three-dimensional reconstruction of the free 30S particle onto the MIR map met with some difficulties, because the cryo-EM and the X-ray map are different in length-to-width ratio as well as in various finer details (Figure 7). Careful inspection of the MIR map indicates, however, that the crystallized particles have a conformation similar to that of the small subunit when bound to the 50S within the 70S ribosome. To further assess this point, we computed the reconstruction of a 'bound' T30S by removing the density that was originally assigned to the 50S subunit within the three-dimensional reconstruction of the T70S ribosome (Figure 5). This reconstruction, called here the 'cut' T30S, led to a reasonable agreement with the main features of the 7.2 Å MIR map (Figure 7). Indeed, using the data from the HR crystals, MR searches gave rise to a solution with reasonable scores (Cf = 52.2, R = 44.8, 40–80 Å) and an arrangement grossly fitting the MIR packing diagram. This arrangement, however, suffers from moderate interparticle collisions, presumably because the cut three-dimensional reconstruction does not provide an accurate representation of the conformation selected by the HR crystals.

The fitting experiments suggested that a part of the pairing contacts within the crystals utilize the 30S sites participating in the interactions with the 50S particle within the ribosome. Support for this presumed arrangement was provided recently, in a series of experiments in which DNA oligomers, complementary to several single-stranded segments of the 16S RNA, were diffused into T30S-HR crystals. We found that the infiltration of the oligonucleotide complementary to the 5′ end of the 16S RNA did not lead to any loss of crystal order. The oligomer that binds in solution to the decoding region [41,42], however, caused substantial disorder of the crystals in accordance with its location in the region involved in the pairing. It can also be a result of significant conformational changes caused by its binding.

The assumption that the T30S conformation selected by the HR crystals is close to that of active particles, led to the growth of both the HR and the LR crystals from particles trapped in their functionally active state (by chemical labeling and mild cross-linking during heat activation).

Figure 6

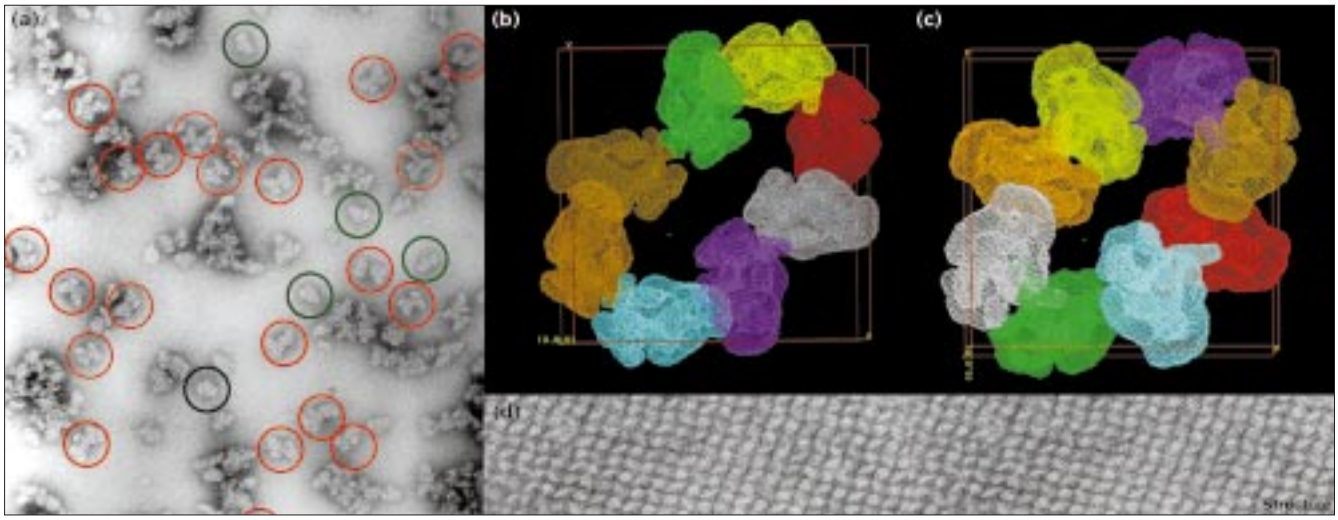

(a) A negatively stained preparation of carefully dissolved T30S-HR crystals observed by EM, showing the butterfly-like T30S pairs (in red circles) together with isolated particles (in green circles). The MR solutions, using the free T30S reconstruction with the X-ray amplitudes from (b) T30S-LR and (c) T30S-HR. (d) A negatively stained thin section of about 500 Å thickness, obtained from an epon-embedded T30S-LR crystal, in a direction approximately perpendicular to the c axis.

Figure 7

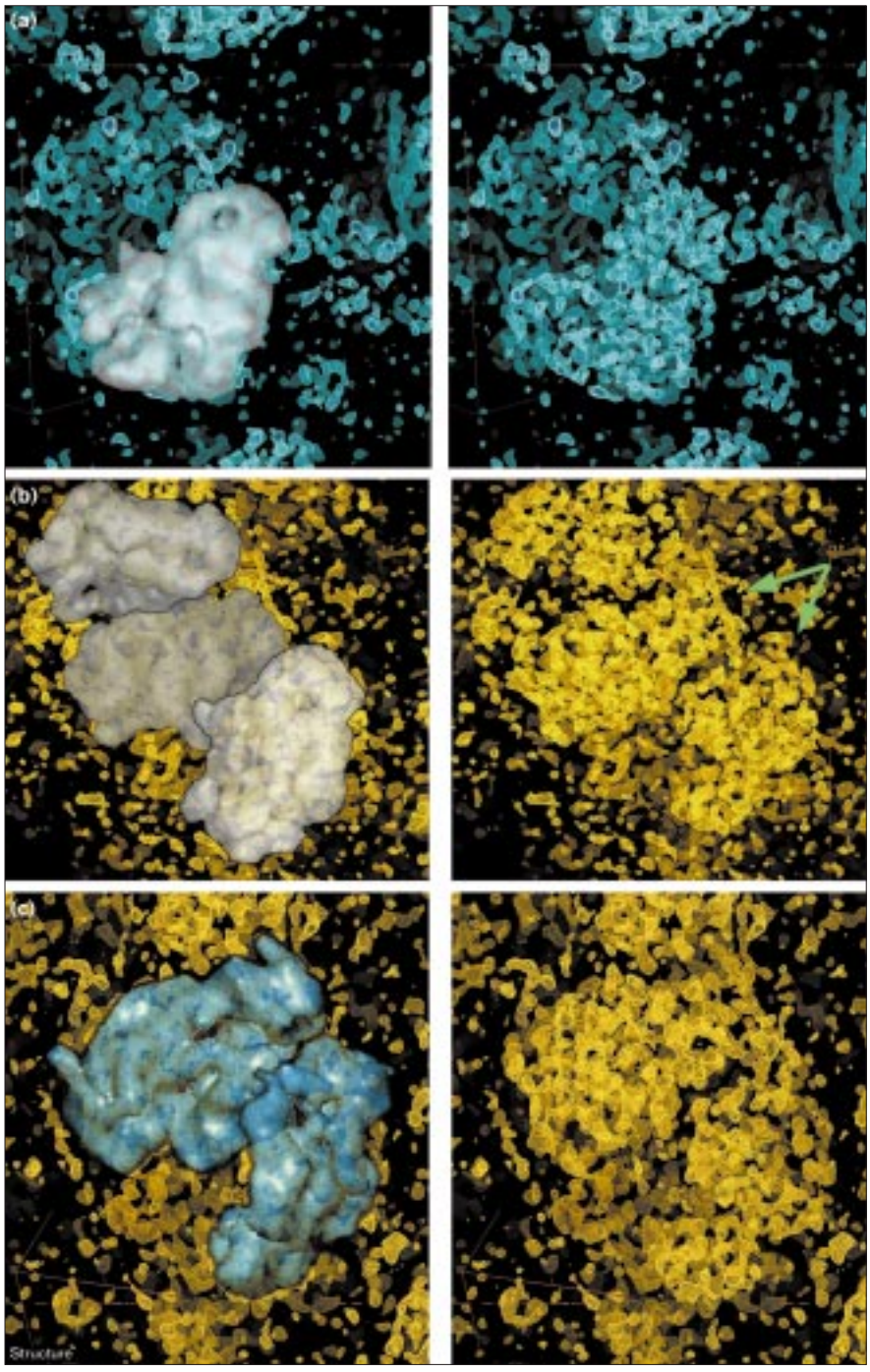

(a) The free T30S reconstruction overlaid on a part of the 7.2 Å MIR map. (b) Three reconstructions of the 'free' T30S overlaid on the 7.2 Å MIR map. The arrows point to the particles creating the extensive contact region (the crystallographic pair). The density between them belongs to a particle in a lower unit cell. (c) Two reconstructions of 'cut' T30S are overlaid on the 7.2 Å MIR map. The density between these originates partially from a particle belonging to a lower unit cell. In all, the right-hand panels show the corresponding part of the 7.2 Å map.

Interestingly, when using the LR crystallization conditions, the quality of these crystals grown from the trapped particles was much higher than that of the native ones, most probably because of their enhanced homogeneity. Furthermore, taking advantage of the sizeable internal solvent region within the crystal that would allow for significant conformational rearrangements, we heat-activated [43] the crystallized particles in order to increase the proportion of 30S particles in their active conformation. These experiments were performed on HR crystals that were found to yield moderate resolution, that is 5–6 Å instead of the expected 3–3.5 Å. Indeed, the controlled heating treatment led to a larger proportion of high quality crystals in our preparations and ensured that the main conformation studied by us is that of functionally active T30S particles.

Discussion

Several aspects of a fruitful interplay between cryo-EM three-dimensional reconstruction and X-ray crystallography are demonstrated in our studies of the *T. thermophilus* ribosome and its two subunits. The uniqueness of the MR solution for the T70S particle, along with the various verification tests, indicates that the resulting packing assembly (Figure 2) is correct. This result, by itself, does not add to the knowledge about the ribosome's structure, beyond what is already known from cryo-EM, but confirms independently the correctness of the cryo-EM three-dimensional reconstruction. Studies on the large subunits, T50S and H50S, have led to more meaningful structural results. Enhanced detail is expected for these particles given that the 17 Å EM reconstruction of T50S might be extended to higher resolution limits by incorporating phase information obtained independently by SIRAS. These studies also provide reliable tools for assessing the correlation between crystallographically determined phases and those obtained by MR, as well as for assessment of the level of the deviation from isomorphism.

Of special interest is the interplay between cryo-EM and crystallography of T30S that intersects several aspects of electron microscopy. The 7.2 Å map, in conjunction with the cryo-EM reconstructions, indicates that the conformation selected by the HR crystals is closed to that of the 30S particle within the assembled ribosome. It also shows pairing of the crystallized particles, an observation that was confirmed by negative-stain EM investigations of partially dissolved crystals. So far no functional relevance can be assigned to the crystallographic or to the previously observed induced pairing [43,44], but it is conceivable that the extensive interparticle interactions emulate some of the contacts in which the small subunit is involved at the intra-ribosomal subunit interface and/or the contacts needed for the formation of intermediates along the path of the translation cycle.

The solvent content of the ribosomal crystals falls within the range observed for other macromolecules (55–70%); the distribution of the solvent regions, however, is rather unique. Sizeable continuous solvent regions were detected in three out of the four crystal forms of the thermophilic ribosomal particles (all of space group $P4_12_12$) as well as in the form diffracting to the highest resolution, H50S, that has a different space group ($C222_1$). Interestingly, the lowest resolution crystals, those of T70S, show smaller solvent cavities, whereas an unusually large continuous solvent region, held rather loosely by one interparticle contact area, was found by MIRAS phasing in the crystals of H50S, the form diffracting to the highest resolution.

The usefulness of cryo-EM reconstructions in phasing data collected from crystals of large particles with no internal symmetry, such as the ribosomes, remains to be seen. Limiting factors stem from the weak diffraction power, the radiation sensitivity and the low level of isomorphism of the crystals, as well as from the character of the EM three-dimensional reconstruction. Thus, flexible particles are likely to yield reconstructions that represent the average of large spectrums of conformations that might differ from the conformation selected by the crystals and consequently might be of little help for MR phase determination. Complications, specific to low-resolution MR studies, arise from difficulties in the verification of the MR solutions. The powerful tool for assessing the reliability of the MR results, namely the correctness of bond lengths and bond angles, that emerges while refining high-resolution structures is missing at low resolution. Even parameters that are normally available for simpler macromolecular systems, such as their volume, bear uncertainties in the case of ribosomes. In addition, maps originating from MR phases lack information about a large fraction of the crystals, namely the non-crystalline solvent, because their structure factors are obtained by back Fourier transformation of the MR assembled map. At high resolution the solvent part of the structure factors might be negligible, but at low resolution (below 8–10 Å) the non-crystalline part might reach values similar to that of the crystalline material.

The H50S crystals pose a further problem because of the high electron density of the solvent, which reaches that of proteins [45], significantly reducing the contrast between the ribosomal proteins (which account for about 35% of the total particle mass) and the solvent. Consequently, in our 12 Å MIRAS map the RNA chains are readily detectable, whereas the outline of the surface ribosomal proteins is less well resolved [2]. Furthermore, it was found that the main differences between the MIRAS map of H50S and the MR solution are in the vicinity of the regions assigned as the locations of the external ribosomal proteins (Figure 4).

The MR searches performed for the verification of the X-ray results proved to be useful for the assessment of the level of structural heterogeneity, using their relative orientations as a guide. Although the orientation information — by itself — might be a rather poor indicator, when combined with the knowledge about the positions of the centers of mass, it was found to be quite useful. The ability (or inability) of the MR phases to reveal heavy-atom sites that were extracted independently by non-MR methods adds to the usefulness of the orientation information.

So far, only two of the large number of searches performed for H50S have yielded MR phases that confirmed heavy-atom sites at low resolutions [2,28]. As mentioned above, these are similar in position, but different in orientation. If indeed this shows two different conformers, it is conceivable that both will lead to structure determination. The

Ta_6Br_{14} site, revealed originally at approximately 10 Å by MIRAS [2], reconfirmed by MR, and shown to be stable at a relatively high resolution (i.e. about 5 Å) by anomalous crystallography, raises the expectations for further progress. The key for reliable structure analysis at high resolution, however, is increasing the level of isomorphism of the H50S crystals. We aim at reducing the conformational variability of the crystallized H50S particles by inducing controlled rearrangements within the crystals, along the lines found useful for the T30S crystals, namely by heat activation, or cross-linking prior to crystallization. The halophilic system poses a greater challenge in the design of such experiments, because of the high salt concentration in the crystallization solution.

Biological implications

Among all ribosomal particles that we examined, H50S and T30S yield the crystals diffracting to the highest resolution: 2.7 Å [1] and 3.0 Å [2], respectively. Whereas the crystals of H50S are highly non-isomorphous [2], we benefitted from the conformational variability of T30S in the growth of two crystal families (LR and HR), each exhibiting normal isomorphism. Consequently, an intermediate 7.2 Å multiple isomorphous replacement (MIR) map of T30S-HR was constructed, showing particles with elongated dense chains that were interpretable as rRNA, and regions fitting the size of average ribosomal proteins.

Cryo-EM reconstructions were found useful in assisting the X-ray crystallography of ribosomal particles and in highlighting several unusual aspects concerning their conformational variability. Thus, inspection of the T30S MIR map indicated that the conformation of the crystalline particles resembles that assigned to the small subunit within the reconstruction of T70S ribosomes. It is conceivable that part of the intensive interactions of T30S within the crystals (seen as pairs) exploits part of the high-affinity binding sites of T30S, such as those forming the interface between the small and large subunits within the assembled ribosome. Indeed, diffusion of DNA oligomers complementary to the 16S rRNA in the decoding region caused severe crystal damage. The destruction of the crystals suggests that the decoding region lies in the vicinity of the extensive interparticle contacts and can also indicate conformational changes that occur upon binding of this oligomer.

Following these observations, we were able to increase the number of crystals diffracting to around 3 Å from preparations showing somewhat lower quality (that is diffracting to 5–6 Å) by heat activation of the crystallized particles. We also obtained crystals of T30S that were chemically trapped in their activated state prior to crystallization and showed that the functionally active trapped particles are still sufficiently flexible to undergo further conformational changes within the crystal.

Finally, our studies are in agreement with the principle of ribosomal universality [13–17,19,45–47]. The MIRAS and MIR maps obtained by us for H50S and T30S show internal and external features revealed in ribosomes from other sources. Furthermore, we and others [28], have shown that the EM reconstructions of eubacterial ribosomal particles (E50S and T50S) are suitable for MR studies of ribosomes from archaea (H50S).

Materials and methods

Cryo-EM reconstruction

Ribosomes and subunits from the same preparations that gave the best three-dimensional crystals have been subjected to the cryo-EM and angular reconstruction procedures. Electron micrographs of the vitreous ice embedded specimens were taken in the liquid helium cooled microscope (SOPHIE) at a magnification of 66.000 and a defocus of about 0.9 microns. The Emil densitometer (Image Science GmbH, Berlin) was used to digitize the micrographs using a sampling step size of 14 μm. The pixel size was coarsened by a factor of 2 resulting in a sampling of 4.48 Å per pixel on the specimen scale. All image processing was performed with the IMAGIC-V software package [4]. Approximately 4000 individually boxed particles (of T30S, T50S and T70S) were aligned using an iterative multireference alignment (MRA) scheme. Upon subsequent application of multivariate statistical analysis (MSA) data compression and classification procedures, characteristic views of ribosomes could be obtained with improved signal-to-noise ratio. The Euler angles of these two-dimensional projection images were determined using the angular reconstruction approach [3].

The data set was submitted to several rounds of iterative refinement including retrojection of the three-dimensional reconstruction, MRA using reprojections as reference images, MSA/classification, Euler angle determination, and three-dimensional reconstruction as performed previously in the reconstruction of 70S from *E. coli* [7]. The resolution of the resulting three-dimensional reconstructions was determined using the Fourier Shell Correlation [48] function with a threshold value of 3σ. The differences in resolution obtained for the various samples can be explained mainly by their different degrees of conformational variability.

Crystal growth, X-ray data collection and MIR studies

The preparations of ribosomal particles, their crystallization and treatment were performed as described earlier [1,2,31,37] with minor modifications, associated mainly with mild treatment. Activation was achieved by heating [41]. For trapping the activated state, mild cross-linking was performed. Negatively stained, epon-embedded thin sections of three-dimensional crystals and negatively stained dissolved crystals were inspected using a Philips CM-100 as in [15,16]. Synchrotron radiation (SR) crystallographic data were collected at cryo-temperature and processed using the progams DENZO and SCALEPACK [49].

Data from the 70S complex crystals were collected at F1/CHESS (R_{merge} = 4.7% and completeness = 96% over the range 17–77 Å) and from T50S crystals at BW7b/EMBL/DESY. To exploit anomalous phase information, data from the Ta_6Br_{14} derivative were collected at two wavelengths: 1.2537 Å (LIII, maximum f″ peak) and 1.2547 Å (LIII near its inflection point, i.e. at maximum f′). The deviation from the Ta edge, namely 1.25530 Å, is caused by the chemical environment within the crystals and to the parameters of BW6/MPG/DESY, where these measurements were performed. Typical R_{merge} (for the three data sets) = 8.1% with completeness of 95–99%.

Data from T30S-LR crystal were collected at BW6/DESY (R_{merge} = 7.9%, completeness = 99.0% up to 12 Å), and from T30S-HR (and its derivatives) at F1/CHESS and ID2/ESRF. For the MR studies the shell up to 12 Å was used (R_{merge} = 6.2%, completeness = 99.6%).

For the construction of the 7.2 Å MIR map 20688 reflections in the range of 7.2–30 Å were included. The sites of the four derivatives were verified by difference Patterson and difference Fourier procedures (FOM = 0.671, phasing power up to 1.4, R_{cullis} = 0.8–0.91).

Data from 59 crystals of H50S, collected at several resolution ranges between 3 Å and 300 Å, were used for the MIRAS and MR studies reported here. These were collected at wavelengths 0.78–1.5 Å at the SR stations reported in the Acknowledgements section, on film, offline and online imaging-plate detectors or CCD cameras. The construction of the 12 Å MIRAS electron-density map is described in [2].

Molecular replacement

MR studies, exploiting cryo-EM three-dimensional reconstructions and SR data, rotation and translation searches, followed by rigid-body refinement, were performed using the program AMoRe [50]. The reconstructions were presented as envelopes of uniform density. Integration radii of lengths comparable to the assumed size of the ribosomal particles (i.e. 70–200 Å) were used. In order to resolve uncertainties between the X-ray and the cryo-EM data sets, the reconstructions were isotropically expanded or contracted by up to 20%, and each of the thus computed models was subjected to a full run of AMoRe. Several parameters, such as resolution shells and different integration radii, were fitted and optimized at each stage. The translation searches were performed for both enantiomorphic space groups, $P4_12_12$ and $P4_32_12$. A map of the unit-cell content was assembled by placing the optimized EM model according to the MR results followed by the application of the symmetry operations. Structure factors and phases were calculated by back transforming the MR assembled map (subroutine gendd in AmoRe). Agreement factors were computed by RSTATS and FOM by SIGMAA [51]. This test was not performed for T30S because neither of its MR results was fully satisfactory.

The searches for T70S were performed as follows. Rotations: 20–40, 20–50, 30–40, 20–34, 25–40 and 20–27 Å; integration radii 106–242 Å; translations: 20–40 and 20–60 Å; rigid-body refinement: 20–40, 20–60 and 20–80 Å; expansion/shrinkage = 0–20%. For T50S, rotation: 20–40, 17–35 and 18–67 Å; translation 20–40, 16–47 and 18–30 Å; rigid-body refinement 20–40 Å; integration radii = 113–133 Å; shrinkage 4%. For T30S, rotation: 25–40 Å; integration radii = 70–160 Å; translation and rigid-body refinement at 25–50 and 25–95 Å. For the 'free' model, optimal solution was obtained with 6% shrinkage (LR) and 0% (HR). No contraction/expansion was needed for the 'cut' T30S because it was obtained from optimized T70S and T50S. Over two dozen H50S data sets were searched, using rotation radii of 17–90 Å.

Acknowledgements

We are exceptionally grateful to the late HG Wittmann, with whom these studies were initiated. We thank M Safro for active participation in the phasing attempts, F Zemlin for the use the SOPHIE EM, W Preetz and M Pope for their generous gifts of heavy-atom compounds, W Traub for his constructive comments and A Podjarny for valuable suggestions. We also thank K Anagnostopoulos and H Avila for producing the cDNA oligomers and H Bartels, WS Bennett, H Hansen, D Janell, S Weinstein, M Peretz, M Piolleti, S Krumbholtz, T Auerbach, M Kessler, C Radzwill, R Albrecht, C Glotz, K Knaack, M Laschever, Y Halfon, S Meier, J Muessig and C Paulke for their participation in the different stages of these studies. Data were collected at EMBL and MPG beamlines at DESY; F1/CHESS, ID2,ID13,D2AM/ESRF, BL26/PF/KEK, and ID19/APS. Support was provided by the US National Institute of Health (NIH GM 34360), the German Ministry for Science and Technology (BMBF 05-641EA), the European Community (B104 CT 972188), BBSRC (28/SBD07611) and the Kimmelmann Center for Macromolecular Assembly at the Weizmann Institute. AY holds the Martin S Kimmel Professorial Chair.

References

1. von Boehlen, K., *et al.,* & Yonath, A. (1991). Characterisation and preliminary attempts for derivatisation of crystals of large ribosomal subunits from *Haloarcula marismortui*, diffracting to 3 Å resolution. *J. Mol. Biol.* 222,11-15.
2. Yonath, A., *et al.,* & Franceschi, F. (1998). The quest for the molecular structure of a large macromolecular assembly exhibiting severe non-isomorphism, extreme beam sensitivity and no internal symmetry. *Acta Crystallogr. A* 54, 945-955.
3. van Heel, M. (1987). Angular reconstitution: *a posteriori* assignment of projection directions for 3D reconstructions. *Ultramicroscopy* 21, 111-124.
4. van Heel, M., Harauz, G. & Orlova, E. (1996). A new generation of the IMAGIC image processing system (Image Science GmbH Berlin). *J. Struct. Biol.* 116, 17-24.
5. Radermacher, M., Wagenknecht, T., Verschoor, A. & Frank, J. (1987). Three-dimensional reconstruction from single-exposure, random conical tilt series applied to the 50S ribosomal subunit. *J. Microscopy* 146, 113-136.
6. Frank, J. (1996). *Three-Dimensional Electron Microscopy of Macromolecular Assemblies.* Academic Press, San Diego.
7. Stark H., *et al.,* & van Heel M. (1995). The 70S *E. coli* ribosome at 23 Å resolution: fitting the ribosomal RNA. *Structure* 3, 815-821.
8. Frank, F., *et al.,* & Agrawal, R.K. (1995). A model of protein synthesis based on cryo electron microscopy of the *E. coli* ribosome. *Nature* 376, 441-444.
9. Agrawal, K.R., Penczek, P., Grassucci, R.A., Li, Y., Leith, A.D., Nierhaus, K.H & Frank, J. (1996). Direct visualization of A-, P- and E-site tRNA in the *E. coli* ribosome. *Science* 271, 1000-1002.
10. Stark, H., *et al.,* & van Heel, M. (1997). Arrangement of the tRNAs in pre- and post translational ribosomes revealed by electron cryo-microscopy. *Cell* 88, 19-28.
11. Stark, H., Rodina, M.V., Rinke-Appel, J., Brimacombe, R., Wintermeyer, W. & van Heel, M. (1997). Visualization of elongation factor Tu in the *E. coli* ribosomes. *Nature* 389, 403-406.
12. Agrawal, K.R., Penczek, P., Grassucci, R.A. & Frank, J. (1998). Visualization of the elongation factor G on *E. coli* 70S ribosome: the mechanism of translation. *Proc. Natl Acad. Sci. USA* 95, 6134-6138.
13. Malhotra, A., *et al.*, & Frank, J. (1998). *E. coli* 70S ribosome at 15 Å resolution by cryo-electron microscopy: localization of fMet-$tRNA_f^{Met}$ and fitting of L1 protein. *J. Mol. Biol.* 280, 103-115.
14. Milligan, R. & Unwin, P.N.T. (1986). Location of the exit channel for nascent proteins in 80S ribosomes. *Nature* 319, 693-696.
15. Yonath, A., Leonard, K.R. & Wittmann H.G. (1987). A tunnel in the large ribosomal subunit revealed by three-dimensional image reconstruction. *Science* 236, 813-816.
16. Arad, T., Piefke, J., Weinstein, S., Gewitz, H.S., Yonath, A. & Wittmann, H.G. (1987). Three-dimensional image reconstruction from ordered arrays of 70S ribosomes. *Biochimie* 69, 1001-1006.
17. Yonath, A. & Berkovitch-Yellin, Z. (1993). Hollows, voids, gaps and tunnels in the ribosome. *Curr. Opin. in Struct. Biol.* 3, 175-180.
18. Berkovitch-Yellin, Z., Bennett, W.S. Yonath, A. (1992). Aspects in structural studies on ribosomes. *CRC Rev. Biochem. Mol. Biol.* 27, 403-444.
19. Yonath, A. & Franceschi, F. (1998). Functional universality and evolutionary diversity: insights from the structure of the ribosome. *Structure* 6, 678-684.
20. Berkovitch-Yellin, Z., Wittmann, H.G. & Yonath, A. (1990). Low resolution models for ribosomal particles reconstructed from electron micrographs of tilted two-dimensional sheets: tentative assignments of functional sites. *Acta Crystallogr. B* 46, 637-644.
21. Jack, A. Harrison, S.C. & Crowther, R.A. (1975). Structure of tomato bushy stunt virus: comparison of results obtained by EM and X-ray diffraction. *J. Mol. Biol.* 97, 163-172.
22. Rossmann, M.G. (1995). *Ab initio* phase determination and phase extension using non-crystallographic symmetry. *Curr. Opin. Struct. Biol.* 5, 650-655.
23. Urzhumtzev, A., Podjarny, A. (1995). On the solution of the molecular replacement problem at very low resolution: application to large complexes. *Acta Crystallogr. D* 51, 888-895.
24. Loewe, J., Stock, D., Jap, B., Zwickl, P., Baumeister, W. & Huber, R. (1995). Crystal structure of the 20S proteosome from Archeon *T. acidophilum* at 3.4 Å resolution. *Science* 268, 533-539.
25. Braig, K., Otwinowski, Z., Hedge, R., Boisvert, D.C., Joachimiak, A., Horwich, A.L. & Sigler, P.B. (1994). The crystal structure of the bacterial chaperonin at 2.8 Å. *Nature* 371, 578-582.
26. Luger, K., Maeder, A.W., Richmond R.K., Segent, D.F. & Richmond, T.J. (1997). Crystal structure of the nucleosome core particle at 2.8 Å resolution. *Nature* 389, 251-260.
27. Rayment, I., Holder, H., Whittaker, M., Yohn, C., Lorenz, M., Holmes, K. & Milligan, R. (1993). Structure of the actin-myosin complex and its implications for muscle contraction. *Science* 261, 58-65.

28. Ban, N., *et al.*, & Steitz, T. (1998). The 9 Å resolution X-ray crystallography map of the large ribosomal subunits. *Cell* **93**, 1105-1115.
29. Trakhanov, S.D., *et al.*, & Moras, D. (1989). Preliminary X-ray investigation on 70S ribosome crystals. *J. Mol. Biol.* **209**, 327-334.
30. Berkovitch-Yellin Z., *et al.*, & Wittmann H.G. (1991). Crystals of 70S ribosomes from thermophilic bacteria are suitable for X-ray analysis at low resolution. *J. Crystal Growth* **110**, 208-213.
31. Hansen, H.A.S., *et al.*, & Yonath, A. (1990). Crystals of complexes mimicking protein biosynthesis are suitable for crystallographic studies. *Biochem. Biophs. Acta* **1050**, 1-5.
32. Volkmann, N., *et al.*, & Wittmann, H.G. (1990). Characterization and preliminary crystallographic studies on large ribosomal subunits from *Thermus thermophilus*. *J. Mol. Biol.* **216**, 239-243.
33. Dude, P., *et al.*, & van Heel, M. (1998). The 80S rat liver ribosome at 25 Å resolution by electron microscopy and angular reconstruction. *Structure* **6**, 398-399.
34. Franceschi, F. *et al.*, & Yonath, A. (1994). Crystallography, biochemical and genetics studies on halophilic ribosomes. *Syst. Apl. Microbiol.* **16**, 197-205.
35. Roth, M., *et al.*, & Yonath, A. (1996). On low resolution phasing of neutron diffraction data collected from ribosomal crystals. In *Biological Structure and Dynamics.* Proceedings of the 9th Conversation (R.H. Sarma and M.H. Sarma eds.), pp. 15-24, Adenine Press, NY.
36. Lata A.R, Agrawal, R.K., Penczek, P., Grassucci, R., Zhu, J. & Frank, J. (1996). Three-dimensional reconstruction of the *E. coli* 30S ribosomal in ice. *J. Mol. Biol.* **262**, 43-52.
37. Franceschi, F., *et al.*, & Yonath, A. (1993). Towards atomic resolution of prokaryotic ribosomes: crystallographic, genetic and biochemical studies. In *The Translational Apparatus* (K. Nierhaus ed.), pp. 397-410, Plenum Press, NY.
38. Yonath, A. Glotz, C. Gewitz, H.S. Bartels, K. von Boehlen, K. Makowski, I. & Wittmann, H.G. (1988). Characterization of crystals of small ribosomal subunits. *J. Mol. Biol.* **203**, 831-833.
39. Schluenzen F., *et al.*, & Yonath A. (1995). A milestone in ribosomal crystallography: the construction of preliminary electron density maps at intermediate resolution. *J. Biochem. Cell Biol.* **73**, 739-749.
40. Richmond, T.J., Finch, J.T., Rushton, B., Rhodes, D., & Klug, A. (1984). Structure of the nucleosome core particle at 7 Å resolution. *Nature* **311**, 532-537.
41. Weller, J.W., & Hill, W.E. (1992). Probing dynamic changes in rRNA conformation in the 30S subunit of the *E. coli* ribosome. *Biochemistry* **31**, 2748-2757.
42. Oakes, M.I., Clark, M.W., Henderson, E. & Lake, J.A., (1986). DNA hybridization electron microscopy: ribosomal RNA nucleotides 1392-1407 are exposed in the cleft of the small subunit. *Proc. Natl Acad. Sci. USA* **83**, 275-279.
43. Zamir A., Miskin, R. & Elson, D.(1971). Inactivation and reactivation of ribosomal subunits: amino acyl-transfer RNA binding activity of the 30S subunits of *E. coli*. *J. Mol. Biol.* **60**, 347-364.
44. Guerin M.F. & Hayes, D.H. (1987). Comparison of active and inactive forms of the *E. coli* 30S ribosomal subunits. *Biochemie* **69**, 965-974.
45. Anderson, K.M. & Hovmoeller, S. (1988). The average atomic volume and density of protein. *Z. Kristallogr.* **213**, 369-373.
46. Verschoor A., Warner JR. Srivastava S. Grassucci RA. Frank J. (1998). Three dimensional structure of the yeast ribosome. *Nuc Acids Res.* **26**, 655-661.
47. Verschoor, A. Srivastava, S., Grassucci, R. & Frank (1996). Native 3D structure of eukaryotic 80S ribosome: morphological homology with the *E. coli* 70S ribosome. *J. Cell. Biol.* **133**, 495-505.
48. Harauz, G. & van Heel, M. (1986). Exact filters for general geometry three-dimensional reconstruction. *Optik* **73**, 146-156.
49. Otwinowski, Z. (1993). Data collection and processing. In *Proceedings of CCP4 Study Weekend*. p.p. 56-62.
50. Navaza J. (1994). AMoRe: an automated package for molecular replacement. *Acta Crystallogr. A* **50**, 57-163.
51. Collaborative Computational Project, No. 4 (1994). The CCP4 suite: programs for protein crystallography. *Acta Crystallogr. D* **50**, 760-763.

Because *Structure with Folding & Design* operates a 'Continuous Publication System' for Research Papers, this paper has been published on the internet before being printed (accessed from http://biomednet.com/cbiology/str). For further information, see the explanation on the contents page.

Ich erkläre, daß ich die vorliegende Arbeit selbständig und nur unter Verwendung der angegebenen Hilfsmittel und Literatur angefertigt habe.

Berlin, 01. 04. 2001. Ante Tocilj

Ante Tocilj

ante@dewar.desy.de

Curriculum Vitae

General

Date of birth	04.12.1971
Place of birth	Split, Croatia
Nationality	Croatian
Languages	Croatian, English

Education

1998-2001 **PhD.** Biochemistry	**Max Planck Institute** Germany	Structure of the small ribosomal subunit from *T. Thermophilus*
1997-1998 Research assistant	**Queen's University** Ontario, Canada	Structure of antifreeze proteins
1995-1997 **MSc** Chemistry	**Feinberg Graduate School** Weizmann Institute of Science Israel	Structural studies of ribosomal particles
1990-1995, **BSc** Molecular Biology	**Faculty of Natural Sciences and Mathematics,** University of Zagreb Croatia	Crystal structure of nifedipine hemisolvates with dioxane and morpholine

Bibliography

Schluenzen, F., Zarivach, R., Harms, J., **Tocilj, A.**,Bashan, A., Yonath, A. & Franceschi, F., 2001. Structural implications of antibiotic action on big ribosomal subunit. ***Nature***, (*in press*).

Tocilj, A., Schlunzen, F., Janell, D., Gluhmann, M., Hansen, H. A., Harms, J., Bashan, A., Bartels, H., Agmon, I., Franceschi, F., & Yonath, A. 1999. The small ribosomal subunit from Thermus thermophilus at 4.5 A resolution: pattern fittings and the identification of a functional site. ***Proc Natl Acad Sci U S A***, 96(25): 14252-14257.

Schluenzen, F., **Tocilj, A.**, Zarivach, R., Harms, J., Gluehmann, M., Janell, D., Bashan, A., Bartels, H., Agmon, I., Franceschi, F., & Yonath, A. 2000. Structure of functionally activated small ribosomal subunit at 3.3 angstroms resolution. ***Cell***, 102(5): 615-623.

Liou, Y. C., **Tocilj, A.**, Davies, P. L., & Jia, Z. 2000. Mimicry of ice structure by surface hydroxyls and water of a beta-helix antifreeze protein. ***Nature***, 406(6793): 322-324.

Harms, J., **Tocilj, A**., Levin, I., Agmon, I., Stark, H., Kolln, I., van Heel, M., Cuff, M., Schlunzen, F., Bashan, A., Franceschi, F., & Yonath, A. 1999. Elucidating the medium-resolution structure of ribosomal particles: an interplay between electron cryo-microscopy and X-ray crystallograhy. **Structure Fold Des**, 7(8): 931-941.

Medalia, O., Koster, A. J., **Tocilj, A.**, Angenitzki, M., Sperling, J., Berkovitch-Yellin, Z., & Sperling, R. 1997. Automated electron tomography of large nuclear RNP (InRNP) particles-- the naturally assembled complexes of precursor messenger RNA and splicing factors**. J Struct Biol**, 120(3): 228-236.